



## DISSERTATION

---

# Omnidirectional Interferometric Strain Sensors for Lamb Wave Detection

ausgeführt zum Zwecke der Erlangung des akademischen Grades  
eines Doktors der technischen Wissenschaften unter der Leitung von

*Ao. Univ. Prof. Dipl. Ing Dr. Franz Keplinger*  
Institut für Sensor- und Aktuatorssysteme

eingereicht an der Technischen Universität Wien  
Fakultät für Elektrotechnik und Informationstechnik

von

Just K. Agbodjan Prince

Hadikgasse 38, 1140 Wien

Matr.-Nr. 0025814

Wien, im Dezember 2016

---

The research presented in this thesis was carried out at the Institute of Sensor and Actuator Systems, Vienna University of Technology and the Center for Integrated Sensor Systems, Danube University Krems, Wiener Neustadt.

This work was supported by the project Nr. FFG 814579 and partially co-funded by the European Commission under the European Regional Development Fund according to article 4 ERDF, and the province of Lower Austria.

Supervisor: *Ao. Univ.-Prof. Dipl.-Ing. Dr. Franz Keplinger*  
Co-supervisor: *Dipl.-Ing. Dr. Franz Kohl*

Referee I: *Ao. Univ. Prof. Dipl.-Ing. Dr. Franz Keplinger*  
Institute of Sensor and Actuator Systems  
Vienna University of Technology, Austria

Referee II: *Ao. Univ. Prof. Dipl.-Ing. Dr. Roland Grössinger*  
Institute of Solid State Physics  
Vienna University of Technology, Austria

Albert Einstein (1879-1955): “If we knew what it was we were doing, it would not be called research, would it?”

# Summary

This thesis deals with a highly responsive method for detecting guided elastic waves, which is a promising means of non-destructive monitoring of large, preferably plate-like composite structures. Aiming at operation in environments of high electromagnetic activity, a double Michelson interferometer composed of fiber-optic components forms the core of the wave strain transduction system. The investigated interferometer employs a  $3 \times 3$  fiber-optic directional coupler for splitting and recombining optical waves. A segment of optical fiber that is preferably attached to the surface of the monitoring body carrying the elastic wave forms the measurement arm of the interferometer while a separate segment serves as reference. The directional characteristic of the strain transduction varies between pronounced directional or omnidirectional depending on the straight or circular shape of the attached fiber segment, respectively. Multi-turn spiral coiled fiber segments enable extraordinary high strain resolution. The double interferometer technique offers pseudo-quadrature interferometer signals that enable rather uniform resolution over a wide range of fiber elongation.

This research work examines the function, technical properties, and application related aspects of interferometric transducers using finite element analysis and analytical modeling. Basic system characteristics are confirmed by experiments.

Fundamental questions related to the selected detection technique that will be answered by this thesis include achievable sensitivity and resolution, perturbations of the elastic waves introduced by the attached fiber segment and the distortions of the fiber-optic strain conversion by the finite length of interaction between fiber and structure. Among other results, a leading-edge strain resolution of  $8 \cdot 10^{-9}$  was achieved with a single-turn fiber-optic strain transducer without any optimization of the detection system. Finite element (FE) simulations proved that attached fiber coils induce very moderate reflection and mode conversion so that a 10-turn fiber coil exhibits twice the elongation of a 5-turn coil. The transducer output signal becomes temporarily deformed compared to the wave strain if the wavelength of the surface strain approximates a fraction of the coil dimension.

The FE simulation of the complete conversion chain, comprising piezoelectric actuation, elastic wave propagation and fiber-optic strain conversion was successfully accomplished. The simulation results agree well with the performed measurements. By deploying a fully-fledged FE model of the mechanical behavior of layered composite material, it was shown that the commonly applied quasi-equivalent orthotropic material model delivers rather poor accuracy.

As optical fibers are mechanically vulnerable and interferometric transduction suffers from interference by non-uniform temperature variations, a robust construction of the wave strain transducer has been devised. The core of this novel approach is a sandwich construction comprising two thin protective sheets carrying the measurement segment of the fiber interferometer and the reference fiber segment respectively. A compliant intermediate layer made of soft elastomer serves for mechanical decoupling of the reference arm of the interferometer from the measurement arm and its carrier that is attached to the deforming

plate sample. Its thermal conductivity enables a uniform temperature throughout the interferometer arms. The implementation of the novel robust transducer was confronted of the restriction availability of construction material. Nevertheless, the measured sensitivity of the order of  $10^{-8}$  is very encouraging in spite of the comparable rigid steel protective carriers used for the first implementation.

This thesis is structured into seven chapters. Chapter 1 describes the state-of-art of structural health monitoring, which is the target application for the research done in this thesis.

In Chapter 2, an overview of the fundamental theory of elastic wave propagation in solids is given. Guided waves, especially the Lamb waves, are presented and their ability of damage detection is illustrated. Different methods of Lamb wave production are discussed along with the mechanisms behind them, especially wave generation with piezoelectric actuators.

Chapter 3 presents the state-of-art of the diversity of fiber-optic strain transducers and detection methods. After a brief discussion of the advantages of fiber-optic transduction, a classification of fiber-optic transducers and a description of the interferometric fiber-optic transducer setup applied in this thesis is provided. The fiber-optic double Michelson interferometer function is investigated. Fiber-optic path length changes due to applied strains is modeled for multi-turn fiber coils and its relation to measured fiber length changes is demonstrated. The novel, robust and reusable fiber-optic transducer is explained.

Chapter 4 describes different model implementations using the finite element methods. First, a finite element model enabling quantitative comparison between simulation and interferometric strain measurements is presented, that exploits a specific configuration for wave excitation, propagation and detection. Having confirmed the basic function of the fiber-optic transducer, further models are devised to study secondary effects such as the loading of the plate by the fiber-optic transducer or the signal distortions introduced by the finite extent of the sensing fiber segment. Afterwards, FE models that tackle the most complex and computational costly case of wave excitation and propagation in stratified media like CFRP are presented. Two different studies are conducted: a rough approach approximates the CFRP by an equivalent orthotropic material and a refined model treating the CFRP as layered composite material. Different fiber-optic coil turn number have been designed and the responses of the system for different excitation pulses are taken into account to evaluate for elastic wave propagation in the plate. Finally, the robust transducer is modeled.

Chapter 5 presents experimental investigations of wave strain transduction using specific types of fiber-optic transducers. The prototype models in the previous chapter are implemented using a pair of piezoelectric ceramic actuators to discuss the corresponding models. The processing of interferometer output signals delivering the sought wave strain is discussed. The received signal of finite-size transducers is interpreted using a convolution approach. This chapter is concluded with design, experimental setup and measurement of Lamb wave on a composite material using the robust and reusable transducer.

Chapter 6 contains in depth discussion of the relation between simulated and experimental results of both the reference and the robust models.

Finally, in the chapter 7 the research specifics from this work are summarized and possible directions for future research on fiber-optic SHM are presented.

# Kurzfassung

Diese Arbeit beschäftigt sich mit einem reaktionsschnellen Verfahren zur Erfassung von geführten elastischen Wellen, welches ein vielversprechendes Mittel zur zerstörungsfreien Überwachung von großflächigen und vorzugsweise Kompositstrukturen ist. Das für die Wellendehnung verwendete Messverfahren beruht auf einem doppeltes Michelson-Interferometer mit faseroptischen Komponenten, welches den störungsarmen Betrieb in Umgebungen mit hoher elektromagnetischer Aktivität garantiert. Das untersuchte Interferometer verwendet einen  $3 \times 3$  faseroptischen Richtkoppler zur Aufspaltung und Rekombination von optischen Wellen. Ein Segment der optischen Faser, die fest mit der Oberfläche der Körpers angebracht wird, welcher die elastische Welle führt, bildet den Meßarm des Interferometers, während ein separates, von Umwelteinflüssen geschütztes Segment als Referenzarm dient. In Abhängigkeit von der geraden oder runden Form des befestigten Fasersegments, variiert die Richtcharakteristik des Wandlers von cosinus-förmig bezüglich der Faserrichtung bis zu omnidirektional. Fasersegmente in Form einer flachen Spirale ermöglichen beispielsweise eine außergewöhnlich hohe, omnidirektionale Belastungsauflösung. Die verwendete Interferometerkonfiguration liefert zwei Pseudo-Quadratur Signale, die eine durchgehend hohe Auflösung über einen weiten Bereich von Faserdehnung ermöglichen.

Diese Forschungsarbeit untersucht die Funktion, die technischen Eigenschaften und anwendungsbezogene Aspekte von interferometrischen Transducern unter Verwendung der finiten Elementenanalyse und der analytischen Modellierung. Grundlegende Systemcharakteristiken werden durch Experimente bestätigt.

Grundlegende Fragen betreffend die ausgewählte Wellen-Erkennungstechnik, welche in dieser Arbeit beantwortet werden, beinhalten die erreichbare Empfindlichkeit und die Auflösung, die Störungen der elastischen Wellen, welche durch das beigefügte Fasersegment eingeführt werden und Verzerrungen der faseroptischen Dehnungsumwandlung für speziell geformte Fasersegmente. Im Experiment wurde eine Dehnungsauflösung von  $8 \cdot 10^{-9}$  mit einer ringförmigen Glasfaser mit 25 mm Durchmesser erreicht. Mit Finite-Elemente-Simulationen wurde bewiesen, dass typische Faserspulen sehr moderate Reflexion und Modenumwandlung induzieren, sodass eine 10-Windungs-Faserspule zweimal die Dehnung eines 5-Windungs Systems aufweist. Das Transducer Ausgangssignal wird verzerrt wenn der Spulendurchmesser in die Größenordnung der halben Wellenlänge der geführten elastischen Welle kommt.

FE-Simulationen, welche die gesamte Umwandlungskette, bestehend aus piezoelektrischen Aktuatoren, elastischer Wellenausbreitung und faseroptischer Dehnungsumwandlung umfassten, wurden erfolgreich durchgeführt. Die Simulationsergebnisse für praktische Implementierungen stimmen sehr gut mit den durchgeführten Messungen überein. Durch den Einsatz eines kompletten FE-Modells des mechanischen Verhaltens von Schichtverbundmaterial, wurde gezeigt, dass das üblicherweise angewendete quasi-äquivalente orthotrophe Materialmodell nur ungenaue Ergebnisse liefert.

Da optische Fasern mechanisch fragil sind und die interferometrische Transduktion unter Temperaturschwankungen leidet, wurde eine robuste Konstruktion des Wellen-Dehnungsaufnehmers

erdacht. Der Kern dieses neuen Ansatzes ist eine Sandwichkonstruktion aus zwei dünnen Schutzblechen, welche das Messsegment des Faser-Interferometers bzw. des Referenzfasersegments tragen. Eine nachgiebige Zwischenschicht aus weichem Elastomer dient zur mechanischen Entkopplung des Referenzarms des Interferometers vom Meßarm, dessen Trägerarm mechanischen Wellenleiter fest angebracht ist. Die Wärmeleitfähigkeit der beiden Träger sorgt für eine gleichmäßige Temperatur der Interferometerarme und damit für gute Langzeitstabilität. Die gemessene Empfindlichkeit in der Größenordnung von  $10^{-8}$  ist sehr vielversprechend zumal relativ starres Edelstahlblech als Trägermaterial für die Faserspulen benutzt wurde.

Diese Arbeit ist in sieben Kapitel gegliedert. Kapitel 1 beschreibt den state-of-the-art des Structural Health Monitoring (SHM), der kontinuierlichen Überwachung von kritischen Strukturelementen, welche die Zielanwendung der Forschungstätigkeit in dieser Arbeit ist.

In Kapitel 2 wird ein Überblick über die fundamentale Theorie der elastischen Wellenausbreitung in Festkörpern gegeben. Geführte Wellen, vor allem die Lamb-Welle, werden präsentiert und ihre Fähigkeiten für die Schadenserkennung werden dargestellt. Verschiedene Methoden der Produktion von Lamb-Wellen und die dahinterstehenden Mechanismen werden diskutiert, vor allem die Generierung von diesem Wellen mit piezoelektrischen-Aktuatoren.

Kapitel 3 präsentiert den state-of-the-art der Vielfalt der faseroptischen Dehnungstransducer und Nachweismethoden. Nach einer kurzen Diskussion der Vorteile der Glasfaserübertragung, wird eine Klassifizierung von faseroptischen Sensoren und eine Beschreibung des interferometrischen faseroptischen Transduceraufbaus, welcher in dieser Arbeit verwendet wird, zur Verfügung gestellt. Die Funktion des faseroptischen Doppelmichelson-Interferometer-Funktion wird beschrieben. Faseroptische Pfadlängenänderungen aufgrund von angelegten Dehnungen werden für verschiedene Faserkonfigurationen und Wellentypen modelliert und ihre Beziehung zu den gemessenen Faserlängenänderungen werden aufgezeigt. Der neue, robuste und wiederverwendbare faseroptische Transducer wird erläutert.

Kapitel 4 beschreibt verschiedene Modellimplementierungen mit den zugehörigen finite-Elemente-Methoden. Zunächst wird ein finites-Elemente-Modell, welches einen quantitativen Vergleich zwischen Simulation und interferometrischen Dehnungsmessungen ermöglicht, präsentiert, welches eine spezifische Konfiguration für die Wellenanregung, die Ausbreitung und die Detektion nutzt. Nachdem die Grundfunktion des faseroptischen Transducers bestätigt wurde, werden weitere Ausführungen erdacht, um die Sekundäreffekte wie beispielsweise die Belastung der Platte durch den faseroptischen Transducer oder die Signalverzerrungen, die durch die endliche Ausdehnung der Sensorfasersegmente eingeführt wurden, zu studieren. Danach werden FE-Modelle, die den komplexesten Fall der Wellenanregung und Übertragung in geschichteten anisotropen Medien, wie z.B. Kohlefaserverstärkte Lamine vorgestellt. Zwei verschiedene Studien werden durchgeführt: eingrober Ansatz, der sich dem CFRP durch ein äquivalentes orthotropes Material annähert und ein verfeinertes Modell, das das CFRP als Schichtverbundmaterial behandelt. Zudem werden die Antworten des Systems für verschiedene Anregungsimpulse berücksichtigt, um die elastische Wellenausbreitung in der Platte zu bewerten. Letztendlich wird der robuste Transducer modelliert.

In Kapitel 5 werden experimentielle Untersuchungen der Wellendehnungsübertragung unter Verwendung von spezifischen Typen von Glasfaser-Transducern präsentiert. Ein zu den Modellen des Vorigen Abschnitts korrespondierender Prototyp wurde mittels eines Paares von piezoelektrischen Keramikaktuatoren implementiert, um die Simulationsmodelle zu verifizieren. Die Verarbeitung von Interferometer-Ausgangssignalen, welche die gesuchte Wellendehnung liefern, wird diskutiert. Dieses Kapitel wird mit Design, experimentiellem Aufbau und Messung an einem Verbundwerkstoff unter Verwendung des robusten und wieder ver-

wendbaren Transducers abgeschlossen.

Kapitel 6 enthält eine eingehende Diskussion über die Beziehung zwischen simulierten und experimentiellen Ergebnissen sowohl des Referenz- als auch des robusten Modells.

Schließlich werden im Kapitel 7 die Forschungs-Besonderheiten dieser Arbeit zusammengefasst und mögliche Richtungen für zukünftige Forschung über Glasfaser SHM vorgestellt.

# Résumé

Le travail présenté dans cette thèse a consisté à développer une méthode très sensible de détection des ondes élastiques guidées. Il se trouve que cette méthode s'avère un moyen très prometteur de contrôle non-destructif de larges structures, particulièrement dans le cas des structures composites. Conçu pour des environnements d'activité électromagnétique élevée, le double interféromètre de Michelson composé de fibre optique est le noyau du système de capteur. Ledit système emploie un coupleur directionnel  $3 \times 3$  de fibre optique permettant de diviser et de recombinaer des ondes optiques. Un tronçon de fibre optique, branche mesurante de l'interféromètre, est fixé à la surface de l'objet à contrôler qui est lui-même traversé par l'onde élastique alors qu'une deuxième tronçon distinct sert de référence. La caractéristique directionnelle du capteur de tension ou de traction varie entre la position dans une seule direction ou dans tous les sens en fonction de la forme droite ou circulaire du segment de fibre optique mesurant. Ainsi, plusieurs tours de segments de fibre enroulés en spirale permettent une résolution extraordinaire de détection de tension. La technique du double interféromètre offre des signaux qui permettent une résolution assez uniforme sur une large gamme d'allongement de la fibre.

Ce travail de recherche examine les fonctions, les propriétés techniques, et l'application interférométrique du capteur, en utilisant le logiciel commercial COMSOL d'analyse par éléments finis accompagné de la modélisation analytique. Les caractéristiques du système de base sont confirmées par la partie expérimentale.

Cette thèse répondra à des questions fondamentales liées à la technique de détection sélectionnée : sensibilité et résolution du capteur, éventuelles perturbations des ondes élastiques introduites par le segment de fibre pausé à la surface de l'objet à contrôler et par les distorsions de la fibre optique sous tension qui se traduit par l'interaction entre la fibre et la structure. Il faut noter que parmi les résultats obtenus on relève une tension de  $8.10^{-9}$  mesurée par une fibre optique souche d'un tour, sans aucune optimisation du système de détection. Des simulations d'éléments finis ont prouvé que des rouleaux de fibres attachés induisent une réflexion d'onde et des conversions de mode très modérés. Ainsi, le capteur de fibre à 10 rouleaux présente un allongement de fibre deux fois plus long que celui de 5 rouleaux. Le signal du capteur devient temporairement étiré proportionnellement aux ondes de déformation si la longueur d'onde à la surface de la structure se rapproche d'une fraction du diamètre du rouleau.

Une chaîne complète de simulation de la transformation, comprenant le déclenchement des ondes élastiques par un actionneur piézoélectrique, la propagation des ondes, et la conversion de tension par l'allongement de la fibre optique a été réalisée avec succès. Les résultats des modèles simulés correspondent très bien à ceux des expériences réalisées. En déployant un modèle d'éléments finis entièrement détaillé du comportement mécanique du matériel composite en couches, il a été démontré que le modèle communément appliqué comme matériel orthotrope est quasi équivalent, cependant avec moins de précision.

Etant donné la vulnérabilité mécanique des fibres optiques, le capteur interférométrique

souffre d'interférences dues à des variations de température non uniforme, une construction robuste du capteur a donc été mise au point. Le principe de cette nouvelle approche est une construction sandwich comprenant deux feuilles minces de protection, portant respectivement le segment de mesure et de référence. Une couche intermédiaire souple en élastomère sert au découplage mécanique du bras de mesure et du bras de référence qui sont attachés respectivement à leurs supports. La conductivité thermique du nouveau système permet de maintenir une température uniforme à travers les bras de l'interféromètre. La mise en œuvre du capteur robuste a souffert de l'indisponibilité de certains matériaux. Néanmoins, la sensibilité mesurée de l'ordre de  $10^{-8}$  est très encourageante en utilisant des supports de protection en acier rigide.

Cette thèse est structurée en sept chapitres. Le premier chapitre donne un panorama sur les systèmes de surveillance de l'intégrité des structures (Structural Health Monitoring - SHM), qui sera l'application ciblée pour la recherche effectuée.

Dans le chapitre 2, un aperçu de la théorie fondamentale de la propagation des ondes élastiques dans les solides est donné. Les ondes guidées, en particulier les ondes de Lamb sont présentées et la capacité de détection des dommages est illustrée. Différentes méthodes de production des ondes de Lamb sont discutées ainsi que les mécanismes sous-jacents, en particulier la génération des ondes par des actionneurs piézoélectriques.

Le chapitre 3 présente le point de la diversité des extensomètres à base de fibres optiques et des procédés de détection. Après un bref aperçu sur les avantages des capteurs à base de fibre optique, une classification de ces capteurs et une description générale des caractéristiques d'interféromètre à fibre optique appliquée dans cette thèse est décrite. Le principe de fonctionnement du double interféromètre de Michelson est présenté. Les variations de trajectoire des ondes dues aux déformations ont été modélisées pour les tours multiples de fibre. Le lien est établi avec les changements de longueur des fibres mesurés. Le nouveau capteur à fibre optique, robuste et réutilisable, est largement décrit.

Au chapitre 4 on décrit les différentes implémentations de modèles en utilisant la méthode des éléments finis. Dans un premier temps, un modèle d'éléments finis permettant la comparaison quantitative entre la simulation et la modélisation du capteur interférométrique de tension est présente, celui-ci exploite une configuration spécifique pour l'excitation d'onde, leur propagation et leur détection. Après avoir confirmé la fonction de base du capteur à fibre optique, d'autres modèles sont conçus pour étudier les effets secondaires, tels que le poids du capteur optique sur la plaque à contrôler ou les distorsions des signaux introduits par l'étendue finie du segment de fibre mesurant. Enfin, les modèles des éléments finis qui abordent le cas épineux et plus complexe du calcul pour l'excitation et la propagation d'ondes dans les milieux stratifiés comme le polymère à renfort fibre de carbone (PRFC) sont présentés. Deux études différentes sont menées : une approche grossière se rapproche de la PRFC par un matériel orthotrope équivalente et un modèle affiné traitant le PRFC comme un matériel composite en couches. Différents nombres de tours de fibre optique ont été envisagés et les réponses du système pour différentes impulsions d'excitation sont prises en compte pour évaluer la propagation des ondes élastiques dans la plaque. Enfin, le capteur robuste est modélisé.

Le chapitre 5 présente les tests expérimentaux d'investigation des ondes de déformation utilisant des types spécifiques de capteur à fibre optique. Les modèles prototype du chapitre précédent sont mis en œuvre en utilisant une paire d'actionneurs céramiques piézoélectriques correspondants aux modèles. Le traitement des signaux de sortie de l'interféromètre délivrant la souche d'onde de déformation est discuté. Le signal reçu des capteurs est interprété en utilisant une approche de convolution. Ce chapitre se termine par la conception, l'installation

expérimentale et la mesure de l'onde de Lamb dans un matériel composite en utilisant le capteur robuste réutilisable.

Le chapitre 6 propose une discussion approfondie de la relation entre les résultats expérimentaux et simulés à la fois du modèle de référence et du modèle robuste.

Enfin, dans le chapitre 7, les objectifs de la recherche sont résumés et des orientations possibles pour de futures études sur la fibre optique dans le domaine SHM sont présentées.

# Contents

<b>Summary</b>	<b>iii</b>
<b>Zusammenfassung</b>	<b>v</b>
<b>Résumé</b>	<b>viii</b>
<b>Contents</b>	<b>xi</b>
<b>1 Introduction</b>	<b>1</b>
1.1 Motivation . . . . .	1
1.2 Overview of related work: Lamb wave detection in aerospace material . . .	2
1.2.1 Excitation of structures . . . . .	2
1.2.2 Sensing methods for elastic waves . . . . .	4
1.3 Challenges . . . . .	5
1.4 Objective, contribution and outline of the thesis . . . . .	6
<b>2 Elastic waves</b>	<b>9</b>
2.1 Fundamentals of elastic waves . . . . .	10
2.2 Guided elastic waves . . . . .	15
2.2.1 Lamb waves fundamentals . . . . .	15
2.3 Generation of Lamb waves with piezoelectric actuators . . . . .	21
2.4 Composite materials . . . . .	24
2.4.1 Technical aspects . . . . .	24
2.4.2 Simplified models of anisotropic reinforced materials . . . . .	25
2.4.3 CFRP Laminates . . . . .	26
2.4.4 Lamb waves propagation in composite material . . . . .	27
2.5 Summary and conclusion . . . . .	27
<b>3 Fiber-Optic waveguides for sensing</b>	<b>29</b>
3.1 Light source and detectors . . . . .	29
3.2 Fiber-optic sensing . . . . .	31
3.3 Fiber-optic characteristics . . . . .	31
3.3.1 Fiber-optic varieties . . . . .	31
3.4 Classification of fiber-optic transducers . . . . .	32
3.4.1 Fiber Bragg Grating . . . . .	34
3.5 Intrinsic mechanical and mechano-optical characteristics of optical waveguides	36
3.6 Interferometric fiber sensors . . . . .	38
3.6.1 Waveguide based interferometer types . . . . .	40
3.6.2 The employed double Michelson interferometer . . . . .	42

3.7	Transduction of plane waves by a circular fiber segment . . . . .	45
3.8	Robust fiber-optic transducer system . . . . .	46
3.9	Summary . . . . .	48
<b>4</b>	<b>Modeling</b>	<b>49</b>
4.1	A benchmark setup for Lamb wave excitation and detection . . . . .	49
4.1.1	Concept . . . . .	50
4.1.2	Implementation . . . . .	53
4.1.3	FEM results . . . . .	54
4.1.4	Exploration model for spurious effects of fiber-optic transducers . . .	59
4.1.5	FEM analysis of stratified CFRP plates . . . . .	69
4.2	Robust strain transducer . . . . .	74
4.2.1	Model of the robust transducer . . . . .	76
4.2.2	Simulation results for robust transducer . . . . .	77
4.3	Summary . . . . .	79
<b>5</b>	<b>Experimental investigations</b>	<b>84</b>
5.1	General instrumentation . . . . .	84
5.2	Reference model implementation . . . . .	86
5.2.1	Data processing . . . . .	87
5.2.2	Measurement results . . . . .	89
5.3	Novel robust optic fiber transducer . . . . .	92
5.3.1	Design of the robust fiber-optic strain transducer . . . . .	92
5.3.2	Testing concept of the robust transducer . . . . .	93
5.3.3	Sensitivity tests . . . . .	94
5.4	Summary . . . . .	95
<b>6</b>	<b>Discussion of results</b>	<b>97</b>
6.1	Reference model . . . . .	97
6.2	Results for the robust transducer . . . . .	102
<b>7</b>	<b>Conclusion and Outlook</b>	<b>105</b>
7.1	Scope of the work . . . . .	105
7.2	Conclusions . . . . .	106
7.3	Outlook . . . . .	107
	<b>Bibliography</b>	<b>109</b>

# Chapter 1

## Introduction

### 1.1 Motivation

Today's aviation has no excuse for desultory safety. Instead, safety ought to be total, according state-of-the art. Based on this principle, human safety issues belong to the essential driving forces behind technical research and development in recent years, especially in the sensitive aerospace. The safety of aircrafts can only be guaranteed when appropriate damage assessment is available alongside a strict maintenance system.

Aerospace structures are a compromise between optimum weight, maintenance costs, and high safety. To achieve this, modern fiber-reinforced composite material are increasingly replacing the traditional ones [1]. Boeing has increased its use of composite material from 9% in the model 777 to 50% in the model 787. For Airbus, this figure has gone from 23% to 53% between A380 and A350XWB (20% of mass reduction). Composite materials, such as carbon fiber reinforced polymers (CFRPs), are increasingly used in aerospace applications due to their high strength to weight ratio. This trend shows the importance in the characterization of all mechanical properties of these composites and specific needs of monitoring the health during their life time [2]. The novel increasingly deployed structures are, on the other hand, exposed to damages that are unusual for homogeneous isotropic materials. Composites have very different failure types and modes than traditional metal materials.

During the assembling of the aircraft, flight operations or apparatus ageing, an airplane's structure is exposed to many different events, which can produce visible and invisible damages. This creates the necessity to monitor the structure to detect potentially critical damages timely. The development of a detection method for critical damages as well as monitoring systems for structural integrity are crucial for the preventive maintenance program.

Non-Destruction Testing (NDT) recommends scattered waves analysis for in-situ material property change inspections [3, 4, 5]. Damage or change detection through wave analysis, localization, and characterization in aerospace, civil and mechanical engineering infrastructure is a type of Structural Health Monitoring (SHM). SHM technology promises a means to significantly enhance the maintenance-free cycle of aerospace, civil and mechanical engineering infrastructure by eliminating unnecessary inspections by humans [6].

When a composite structure is subjected to heavy loading, microcracks, delaminations, fiber fractures, disbonds between fiber and matrix can occur within the piece. Delaminations and disbonds are most frequent failures that affect the structure performance of composite laminate materials [7, 8, 9]. Such changes, create or modify elastic waves that eventually propagate in the structure. These changes can be detected and analyzed using specific

sensors.

The delamination detection poses challenges which draw the attention of many research groups [10]. Several solutions were proposed and among many others a system using Lamb waves. Lamb waves, first described in theory by Horace Lamb in 1917 [11], are a form of elastic perturbation which can propagate in a solid plate with free boundaries. These guided elastic waves offer long range propagation with moderate attenuation. Their sensitivity to structural discontinuities provides a potentially very attractive means of inspecting large structures. When Lamb waves pass through delamination zones, their amplitude and phase changes and eventually a different wave mode emerges from this site. These phenomena could be well analyzed using finite element models of simplified model geometries as well in labor experiments. From changes in the amplitude ratio, the phase and the time of arrival the new mode, it was found that at least in principle, this system could evaluate the delamination length quantitatively [12, 13, 14]. However, the analysis of Lamb wave propagation becomes rather complex if multiple modes are involved in combination with layered composite materials.

This work deals with the scientific aspects of omnidirectional fiber-optic sensing methods for Lamb waves in homogeneous and composite structures. The focus is put on analytical and numerical modeling investigations of the fiber-optic transduction. Wherever feasible, modeling results are compared to experiments. The designed and developed novel transducer offers high sensitivity, omnidirectional characteristic and allows the construction of low-cost robust setups.

## 1.2 Overview of related work: Lamb wave detection in aerospace material

Various methodologies and systems have been developed for ultrasound wave production, response acquisition, and sophisticated data analysis to characterize or detect changes (e.g., damages) in different materials [15, 16, 17, 18, 19, 20]. Current damage detection and related excitation methods are either visual or localized experimental methods such as vibration-based methods, acoustic or ultrasonic methods, magnetic field methods, radiography, eddy-current methods and thermal field methods [21]. The early approaches are based on correlating numerical models with measured modal properties from undamaged and damaged components using Micro-Electro Mechanical Systems (MEMS), piezoelectric and FBG (Fiber Bragg Grating) sensors. Today's candidate list of ultrasonic transducer technologies is long: several optical fiber interferometric sensors, piezoelectric sensor, MEMS sensor, etc. Among the most promising sensor principles are piezoelectric transducers, FBG, Fabry Perot interferometers, or Brillouin optical time domain reflectometry sensors [22].

### 1.2.1 Excitation of structures

Numerous excitation methods have been developed with potential for rapid or large area inspection capabilities. However, at present, most of them have limitations that prevent them for being used extensively. Laser ultrasound generation is one of these newer methods, but the costs are currently prohibitive and a number of special precautions need to be taken into account. Certainly, the laser systems have the advantage of wide area scanning capacity and are good actuation methods but the setup systems are not easy to move.

Vibration based method is a successful approach used for damage detection in mechanical homogeneous materials [23]. In [3, 24, 25] Cawley and Adams proposed the use of a vibration technique to locate defects in structures made from advanced composite materials. Using this, damage can be detected, located and roughly quantified by measuring changes in natural frequencies of the structure. It is claimed that the severity of the damage can be assessed by additional analysis. This technique is potentially very attractive because properties can be measured at a single point on a structure, hence, access to the total structure is not required. Actual test time can be very short, particularly if the resonant frequencies are excited by an impulse. Also, in the same way, Schultz and Warwick [26] measured the forced vibration response of glass-fiber-reinforced epoxy beams at various intervals during fatigue loading. They found changes in the resonant frequencies to be relatively insensitive to damage. However, they realized that the damping ratio and response magnitude were very sensitive to damage. Cawley [3] reviews several other techniques for detection of simple disbond to more complex delamination in composites using vibration based methods. A comprehensive summary of the vibration-based damage detection methods in isotropic homogeneous material, their applications and their limitations was reported by Doebling et al. [22]. Merely, the question remains whether or not this technique is applicable in this concept to composite structures for example delamination detection.

Acoustic emission (low frequency) and ultrasonic waves (high frequency) are also often used for structure monitoring. Acoustic emission refers to the generation of transient elastic waves produced through an object or plate for material change detection. These guided waves can be also defined as stress waves with a multi-path and multi-modes propagation by the material and boundaries of the structure. The scattered or reflected waves from any interface which separates regions of differing elastic properties are recovered. The detection of most other defects at the same time is possible. Some authors maintain that the most commonly used non-destructive test for composite structures is ultrasonic inspection [27, 28, 29]. The reasons for favoring ultrasonic waves are numerous. Except for the potential for rapid or large-area inspection capabilities, the inspection is very sensitive to the defect types commonly found in composites. It is also one of the few methods available for detecting delamination and it can detect most of the other defects at the same time. Many research groups are currently working on this method for monitoring aluminum and composite materials [4, 27, 28, 29].

Basically, the methods of structure excitation for change detection can be split in two groups: contacting and non-contacting to the sample structure. The first group, involves the connection of an exciter of some form which remains attached to the structure throughout the test. It can be surface-bonded or embedded. In the this case, one is confronted with additional mass. This effect can be reduced by using very lightweight devices. Hence, the excitation type is continuous (sinusoidal, random, etc.) or transient (pulse, chirp, etc). The second type includes devices which are either out of contact throughout the vibration (such as provided by a non-contacting electromagnet, the sound energy transfer is usually promoted by a coupling liquid) or which are only in contact for a short period, while the excitation is being applied.

The piezoelectric is the most widely used method to actuate a guided elastic wave (Lamb wave) signal that propagates into the structure to be monitored and applies small size, light weight and long life time actuators. This elastic perturbation can propagate for long distance in structure with moderate amplitude decrease. It is, then, be recorded either by the same transducer (pulse-echo: radar or sonar systems ) or a different sensor (pitch-catch, transmitter-receiver systems). Several other advantages of the Lamb wave and its generation

are more detailed in chapter 2.

### 1.2.2 Sensing methods for elastic waves

The most widely used techniques for ultrasound diagnostics in solids are based on piezoelectric and fiber-optic transducers [30]. Strain gauges and Microelectromechanical systems (MEMS) devices can be also applied for small area monitoring. However, the electromagnetic interference of the piezoelectric transducer sometimes limits its effectiveness in practical applications [31]. The use of fiber-optic based methods like the fiber Bragg grating (FBG) sensors, diverse fiber based interferometers, or Brillouin optical time domain reflectometry transducers rapidly extends because of their flexibility, high strength, heat resistance, immunity to electromagnetic interference, durability and corrosive resistance of the fiber.

Currently on in-service vehicles used, the strain gauge method for damage monitoring in composite materials applies a voltage across a foil gauge, which is capable to measuring strain by the change in resistance due to deformation. Relatively small, light, and inexpensive, the strain gauge can be easily implemented, and their results are simple to be interpreted. They monitor local strain to detect time-history overloads and deformations. A disadvantage of this technique above mentioned is that the results from a single gauge can only cover a small area of the surface accurately. So, a large quantity of them would be necessary to monitor for example an entire vehicle, yielding a complex system with many wires or a wireless system with many remote power supplies. Therefore, the gauges can only be placed in few predictable problem areas [32].

MEMS are miniature of interns systems that can be easily bonded or embedded the structure. MEMS technology enables the integration of transducers, actuators and signal processing on a single chip. MEMS can also be incorporated into a wireless network with efficient communication systems. Structure monitoring MEMS sensors are commercially available, however, mainly in the low frequency range (up to 10 kHz). MEMS sensors operating at higher frequency are feasible and have been demonstrated [33]. However, they have to be specially made, which requires access to the appropriate MEMS design and fabrication facilities making them also rather expensive at this stage. MEMS transducers can operate on several principles, the most common being capacitive, thermal, magnetic and piezoelectric. A variety of MEMS strain transducers were bonded-to or embedded-in composite plates and tested by Hautamaki et al. [34]. They have demonstrated that such devices can successfully function in both uniaxial and bending loading conditions. Varadan and Varadan [35] further discussed MEMS-based in structure monitoring. In particular, the authors discuss in situ aircraft structure monitoring and found that the biggest single obstacle in implementing such a system is the sensor wiring. Greve et al. [36] used MEMS transducers directly coupled to solids for monitoring. They have also demonstrated phased-array detection of the location and angular position of a source, and also the detection of flaws in a test specimen. Jones et al. [29] overview the use silicon-based MEMS technology for damage detection in CFRP composites. The authors claim that silicon-based microsensors can be used for the detection of impacts as well as the presence of damage. The authors list some serious drawbacks of MEMS and surface acoustic wave (SAW) devices, including the cost and complexities involved with signal conditioning.

In recent researches, piezoelectric transducer for damage detection is the most investigated method in structure monitoring systems [32, 37, 38, 39]. Piezoelectric sensor system uses small size, light weight, and long life time piezoelectric elements that can act as both actuators and sensors for detecting impact damage. Piezoelectric sensors can be used in various

configurations to convert pressure, acceleration, strain, and force into an electrical charge separation. The piezoelectric ultrasound actuator works in the reverse direction where it transmits waves of known properties. Simultaneously, it may receive part of the transmitted waves through reflections. With appropriate electronics, a comparison of transmitted signals with scattered and received wave induced signals (pulse-echo) is feasible. A complex gating procedure is required to suppress extremely high initial actuation potentials at the receiver input where weak signals have to be measured. Piezoelectric sensors are used by Valdes et al. in [40] for investigation of three different laminates in the presence of various damages such as delamination or crack. Tan and Tong [41] involved piezoelectric sensor/actuators, surface mounted as well as embedded within composite structures for delamination detection. Yeum et al. [42] used a considerable number of piezoelectric transducers (9 pieces) for relative small composite plate (1512 mm×762 mm×5 mm) monitoring but achieved real size damage detection.

The fiber-optic methods which are more elaborated on chapter 3, are considered ideal for the composite structure monitoring applications. They possess adequate sensitivity, dynamic range, and bandwidth. The sensing principle involves optical waves guided by fibers that are attached to the structure of interest. This approach promises low weight, very sensitive, capacity of large scanning area, and immunity against electromagnetic disturbances caused, e.g., by piezoelectric actuation. Fiber-optic transducers are capable of absolute measurement of strain, pressure, temperature, acoustic, vibration etc. , mostly non-perturbative to the structure, able to multiplex, and match the lifetime of the structure. They are popular for NDT of composite materials and less common for traditional materials, e.g., aluminum alloys. Fiber-optic sensors may be adapted to monitor strain resulting from either mechanical loads, pressure, temperature, acoustic or ultrasonic excitation, vibrations, or others.

Various types of fiber-optic transducers are used for composite structure monitoring; the most common being the fiber Bragg grating (FBG) device [43, 44]. FBG's modulate their spectral characteristics of transmission and reflection according to the applied strain or temperature variation [45]. Next to the mostly proposed FBG, there are several other transducers based on fiber-optic which are classified and discussed in chapter 3. Several varieties of interferometer setups are used for strain detection in composite material. Elvin and Leung [46] demonstrated the feasibility of fiber based Mach-Zehnder interferometer for delamination detection. They detected the presence of a delamination but could not identify its size and location. Moreover, Fabry-Perot interferometer sensors have been proposed for real-time monitoring of edge-induced and internal delamination in composites [47], but again the delamination size and location could not be determined experimentally.

While MEMS and piezoelectric devices are preferably applied to metals, the FBG techniques are especially popular with composite materials. They could be very sensitive to static and dynamic strain in the grating region that can be made up to a few centimeters long. However, this high sensitivity is pronounced unidirectional for strains oriented parallel to the fiber axis. Hence, more than a single FBG is needed to acquire arbitrary oriented compressive strain. A straightforward monitoring of large areas of aerospace composite material asks for fiber-optic sensors that offer omnidirectional sensitivity characteristic.

### 1.3 Challenges

The inspection of a large composite material area with minimum number of sensors is the goal for today SHM. Such SHM systems ought to perform in-situ on structures with minimum manual intervention. Kessler et al in [9], stated that damage diagnostics in composites is even

more difficult than in metallic structures. The anisotropy of this material, the conductivity of the fibers, the insulating properties of the matrix and the fact that much of the damage often occurs beneath the surface of the laminate complicate all known examination methods.

It appears that ultrasonic testing is the most used technique in industrial applications [8, 12, 19, 28, 48, 49], for large area, sheet-like objects. This method offers transmission, refraction and reflection of ultrasonic Lamb waves (discussed in detail in section 2 of the second chapter) for evaluation. High frequencies give rise detailed to non-destructive analysis of solid material plates. Typically, Lamb waves appear in various modes and it is not practical to produce a single pure mode. It is always recommended to select a low frequency times thickness product of plate ( $f \cdot d \ll 10^3$  m/s) to avoid severe complications introduced by numerous excited Lamb modes. On the other hand, the need of short wavelengths is mandatory for detection of small damages such as delamination. A further complication results from the significant dispersion of Lamb wave modes for  $f \cdot d \gg 100$  m/s.

Beside the effects of environment, the presence of multiple reflections at boundaries together with the various dispersions of individual modes and mode conversion at discontinuities leads to complex features of Lamb waves responses produced by the structure to be monitored. Moreover, in anisotropic and heterogeneous materials such as carbon fiber composite, the analysis of propagating Lamb waves is a complex task. Many details of the actual arrangement influence the obtained signals. Among them are the thickness of the plate in conjunction with the used frequencies and material proprieties, the geometry of the transducers and the boundary conditions.

In this work the physics of guided wave propagation in composite environment is examined and discussed briefly. The foundation of Lamb wave detection using a specific omnidirectional fiber-optic strain transducer will be described and modeled for synthetically excited Lamb wave modes as well as for guided waves produced by piezoelectric actuators. The fiber preferred optic strain transducer comprises a circular or spiral wound section of the optical waveguide that is attached to the surface of the investigated plate. This transducer shape combines enhanced sensitivity with an omnidirectional characteristic. The permissible bending radius of the optical fiber determines the minimum diameter of the transducer which comes well within the range of applicable wavelengths. The expectable strain conversion is modeled analytically for a specific type of interferometer. A detailed mechanical analysis of the optical fiber transducer subjected to concentrated static loads and axial compressive loads is presented. An extension of omnidirectional fiber transducer to a robust and reusable fiber-optic transducer is proposed, modeled and tested. All relevant detection characteristics were studied with the help of finite element analysis covering the complete physical chain from piezoelectric wave excitation up to electronic output of the interferometer. Numerical simulations are performed in order to study the detection of the piezoelectrically actuated Lamb wave in structure. FEM simulations use the Comsol 4.2a Multiphysics suite. Among these results are the loading effect of the fiber-optic transducer, the convolution due to the finite extension of the transducer coil, as well as the interferometric transduction a propagating elastic wave in the plate by the guided light wave in the fiber. A very good agreement between simulated and measured signals was achieved for appropriate experimental arrangements.

## 1.4 Objective, contribution and outline of the thesis

This thesis explores the properties of a specific type of fiber-optic transducer as a means to detect guided elastic waves. Numerical modeling supported by analytical considerations

are used to predict the effectiveness of various implementations, and to help in design of appropriate testing procedures. Subsequently, related experiments were performed.

After a short explanation of the reasons for choosing Lamb wave excitation combined with fiber-optic strain transduction, the work briefly describes the generation of the probing signal, especially by using piezoelectric actuators. The main objectives of the thesis are detailed exploration of the transduction chain for Lamb waves passing through a custom configured optical fiber used as strain converter. A recently proposed fiber interferometric arrangement [50] is investigated in depth, taking into account side effects of the strain transducer as structure loading, mode conversion, and reflection of Lamb waves in different materials. The studies are based on a hybrid setup comprising a piezoelectric actuator or alternatively synthetic Lamb mode excitation and a coiled fiber-optic transducer. The thesis first proceeds to the study of elastic wave detection by numerical modeling from finite element method (Comsol 4.2a), followed by experimental works. Due to the occurrence of multiple Lamb wave modes, their different propagation speed and velocity dispersion and eventual propagation in anisotropic heterogeneous media, the interpretation of strain transducer signals is a rather complex task. Complexity increases generally with structural complexity (e.g. stiffeners, thickness variations, transmission and reflection between layers etc. ). As these complications are so complex and diverse that practical systems are exclusively based on the detection of deviations from reference measurements on the very same structure.

In this chapter the motivation, state-of-art of actuation are presented and the sensing methods are listed. The focus is put on the damage detection process by composite materials. The challenge to be faced and the word structure are presented. The further chapters are structured in the following manner:

In Chapter 2, an overview of the fundamental theory of elastic wave propagation in solids is given. Guided wave, especially the Lamb wave is presented and its ability of damage detection is illustrated. Detailed modeling of Lamb wave modes are presented. Different methods of Lamb waves production are discussed along with the mechanism behind them, especially waves generation with piezoelectric actuators. Lamb wave propagation in fiber reinforced carbon composite and the stiffness tensor of composite materials is determined and an quasi equivalent orthotropic model is developed to concludes this chapter.

Chapter 3 presents the state-of-art of the diversity of fiber-optic strain transducers and detection methods. After a brief discussion of the advantages of fiber-optic transduction, a classification of fiber-optic transducers and a description of the interferometric fiber-optic transducer setup applied in this thesis is presented. The fiber-optic double Michelson interferometer function is investigated. Fiber-optic path length changes due to applied strains is modeled for multi-turn fiber coils and its relation to measured fiber length changes is demonstrated. The novel, robust and reusable fiber-optic transducer is described and presented.

The chapter 4 describes different model implementations using the finite element methods (Comsol 4.2a). First, a finite element model enabling quantitative comparison between simulation and interferometric strain measurements is presented, that exploits a specific configuration for wave excitation, propagation, and detection. Having confirmed the basic function of the fiber-optic transducer, further models are devised to study secondary effects such as the loading of the plate by the fiber-optic transducer or the signal distortions introduced by the finite extent of the sensing fiber segment. Finally, FE models that tackle the most complex and computational costly case of wave excitation and propagation in stratified media like CFRP are presented. Two different studies are conducted: a rough approach approximates the CFRP by an equivalent orthotropic material and a refined model treating the CFRP as layered composite material. Different fiber-optic coil turn number have been

designed and the responses of the system for different excitation pulses are taken into account to evaluate for elastic wave propagation in the plate. Finally, the robust transducer is modeled.

Chapter 5 presents experimental investigations of wave strain transduction using specific types of fiber-optic transducers. The prototype models in the previous chapter are implemented using a pair of piezoelectric ceramic actuators enabling discussions in view of the corresponding models. The processing of interferometer output signals delivering the sought wave strain is discussed. Signal processing knowledge for interpretation of signals received by the fiber-optic strain transducer in comparison with piezoelectrically excited signals is discussed. The received signal of finite-size transducers is interpreted using a convolution approach. This chapter is concluded with design, experimental setup and measurement on a composite material of the robust and reusable transducer.

Chapter 6 contains an in depth discussion of the relation between simulated and experimental results of both the reference and the robust models.

Finally, chapter 7 concludes and offers an outlook to the future work. The research specifics from this work are summarized and possible directions for future research on fiber-optic SHM are presented.

# Chapter 2

## Elastic waves

Guided ultrasonic elastic waves have emerged as one of the most promising tools for structure health monitoring (SHM) due to their well established theory, their ability to detect small damages within relatively large inspection areas, and the capacity to monitor large areas of material from a single location; even in material with a moderate attenuation such as carbon fiber reinforced polymers (CFRP). Advancements in piezoelectric transducer technologies used for guided wave excitation and also for sensing, reinforce the use of Lamb waves in non-destructive monitoring. In recent years, a large number of papers and books have been published, which stress the benefits of guided waves over other technologies [30, 51, 52]. Variable mode structures and distributions, propagation over long distances, capability to follow curvature and reach hidden or buried parts, and sensitivity to different type of flaws are some reasons of using Lamb waves. The drawback is that they require complex detection analysis. Type of ultrasonic waves, Lamb waves are guided between two parallel free surfaces of a plate. In 1917, Lamb described guided waves in flat plates for the first time [11]. Lamb

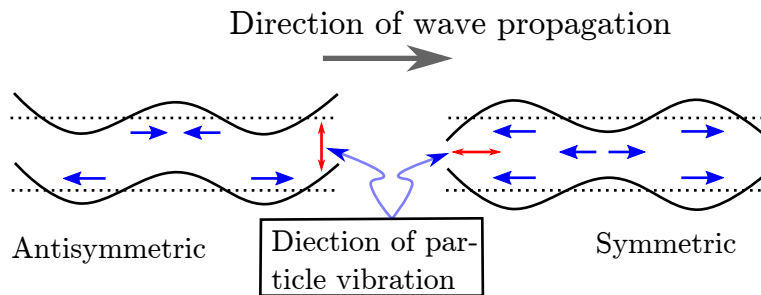


Figure 2.1: Illustration of Lamb wave: symmetric compressional and antisymmetric flexural modes.

waves are of two basic varieties: symmetric guided modes compressional and antisymmetric flexural modes. Symmetric and antisymmetric Lamb waves exhibit different dependencies of phase and group velocities on the exciting frequency. Furthermore, their distributions of particle displacements and stress through the plate thickness are different.

To exploit Lamb waves diagnostics, a thorough understanding of the theoretical fundamentals is indispensable. In the order to provide fundamental characteristics such as phase and group velocities. Solving wave equations is required to answer questions like: What types of ultrasonic waves can exist? The effective stiffness tensor of materials is needed to compute the dispersion curves of Lamb waves which predict their propagation inside the material, all this taking into account the various degrees anisotropy.

## 2.1 Fundamentals of elastic waves

An elastic solid body is said to be strained when the relative distances between particles points in the body are changed under stress [53]. Elastic waves occur as a result of the restoring forces between the particles of material. Excited in a medium, elastic waves transmit changes in stress and particles velocity inside the material. Periodic change in stress and velocity influence the quantitative wave characteristics. These are the frequency, phase, wave speed, and amplitude of particle displacement. Let's assume harmonic guided plane wave propagation along the plate  $x$ -axis in a Cartesian coordinate system of a solid body in which a wave propagates without any (or negligible) damping/attenuation. The wave propagating in the plate is consider as a scalar field. Under the action of excitation, the body's particle elements interact. It denotes internal forces as body force and external forces as contact forces<sup>1</sup>. However, the elasticity is the property of mechanical materials that connects stress and strain which in turn is related to the relative displacement of infinite volume elements. The equation of motion expresses well these relations, where two fundamentals principles of physics are taken into account, which are the conservation of momentum and the conservation of angular momentum. Newton's law states that by applying a force  $\mathbf{f}$  per unit volume on a solid at the center of mass of a small volume  $dV$

$$\mathbf{f} = \rho \mathbf{a} = \rho \frac{\partial^2 \mathbf{u}}{\partial t^2}, \quad (2.1)$$

where  $\rho$  is the mass density,  $\mathbf{a}$  is the acceleration vector and  $\mathbf{u}$  the displacement vector of the respective point  $P(x_1, x_2, x_3)$  center of gravity of the solid, which coordinates  $x_k$  vary with time. Consider at time  $t$  the small volume  $dV$  of the medium, bounded by the surface  $S$  with  $\mathbf{s}$  a surface traction defining a force per unit area of the linear momentum principle result (see Fig. 2.2); the instantaneous rate of change of the linear momentum of a small body is equal to the resultant external forces acting on the body at any particular instant of time. Considering that the elastic solid body is in dynamic equilibrium, the conservation

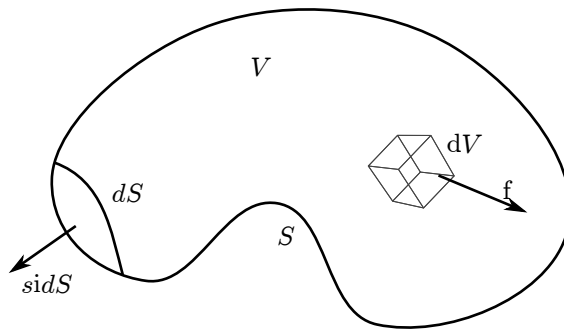


Figure 2.2: Momentum principles.

of linear momentum implies that the external forces acting on this region are balanced by inertial forces and thus the resultant force must vanish [54],

$$\oint_S \mathbf{s} dS + \int_V \mathbf{f} dV = \frac{d}{dt} \int_V \rho \frac{\partial \mathbf{u}}{\partial t} dV. \quad (2.2)$$

<sup>1</sup>The strain is fully depending of forces orientation. The constitutive law relating the applied force to the resulting deformation is called Hooke's Law. It defines the relationship between stress and strain.

$\rho$  denotes the mass density of the solid in equilibrium state. It is assumed that by small deflections, linear theory can be applied. Based on linear theory and applying the divergence theorem (also called Gauß integral theorem) to the surface integral allows the conversion to a volume integral, and by substituting the Cauchy stress formula ( $\mathbf{s} = \underline{\underline{\sigma}}\mathbf{n}$ ) in Eq. 2.2, where  $\underline{\underline{\sigma}}$  is the stress tensor and  $\mathbf{n}$  is unit-length direction vector. This relation can then be expressed as

$$\oint\!\!\!\oint_s \underline{\underline{\sigma}}\mathbf{n}dS + \int_V \mathbf{f}dV = \frac{d}{dt} \int_V \rho \frac{\partial \mathbf{u}}{\partial t} dV \iff \int_V (\nabla \cdot \underline{\underline{\sigma}} + \mathbf{f} - \rho \frac{\partial^2 \mathbf{u}}{\partial t^2}) dV = 0, \quad (2.3)$$

where  $\nabla$  is the del operator, and  $\nabla \cdot \underline{\underline{\sigma}} = \sum_j \frac{\partial \sigma_{ij}}{\partial x_j}$ . Since the Eq. 2.3 applies for arbitrary volumes, the integrand must vanish, i.e. the momentum conservation gives

$$\nabla \cdot \underline{\underline{\sigma}} + \mathbf{f} = \rho \frac{\partial^2 \mathbf{u}}{\partial t^2}. \quad (2.4)$$

Equation 2.4 states that the elastic forces applied to the volume element are in balance with the inertial force acting on this volume, the elasticity law can be applied. In the case of absence of external forces ( $\mathbf{f} = 0$ ), Eq. 2.4 reduces to the fundamental wave equation, governing elastic solids [55], which are not subjected to external body forces follows

$$\rho \left( \frac{\partial^2 \mathbf{u}}{\partial t^2} \right) = \nabla \cdot \underline{\underline{\sigma}}. \quad (2.5)$$

For very small deflections, Hooke's law states that the strain is linearly proportional to the stress. The stress components  $\sigma_{ij}$  have the dimension of a force over a unit area ( $i$ -plane) in a direction ( $j$ -direction), Hooke's law states

$$\sigma_{ij} = \sum_k \sum_l c_{ijkl} \varepsilon_{kl}, \quad i, j = 1, 2, 3. \quad (2.6)$$

Here  $\varepsilon_{kl}$  denotes the strain tensor components

$$\varepsilon_{kl} = \frac{1}{2} \left( \frac{\partial u_k}{\partial x_l} + \frac{\partial u_l}{\partial x_k} \right) \text{ or } \underline{\underline{\varepsilon}} = \frac{1}{2} \left( [\nabla \mathbf{u}]^T + \nabla \mathbf{u} \right), \quad (2.7)$$

where T is the transpose operator. Equation 2.5 establishes a connection between the dynamic restoring forces and the material displacement gradient. The constitutive relations form of Hooke's law, which show the interdependence of strain  $\varepsilon_{kl}$  and stress  $\sigma_{ij}$  are given either in terms of the stiffnesses tensor  $\underline{\underline{\underline{C}}}$  (rank four,  $3^4 = 81$  components) or the strain tensor  $\underline{\underline{\varepsilon}}$ , in the expression 2.6. Due to the second conservation law of momentum (the conservation of angular momentum), the stress tensor is symmetric, i.e.  $\sigma_{ij} = \sigma_{ji}$ . The strain tensor is symmetric  $\varepsilon_{kl} = \varepsilon_{lk}$  [56]. The symmetry condition on both tensors implies that only six of the nine tensor components are needed to fully describe the stress and strain relation of the body. Thus, the stiffness tensor  $\underline{\underline{\underline{C}}}$  must have a corresponding degree of symmetry (minor and major symmetries) which leads to the simplifications [53]

$$c_{ijkl} = c_{jikl} = c_{ijlk} = c_{jilk}, \quad (2.8)$$

$$c_{ijkl} = c_{klij}. \quad (2.9)$$

In terms of displacements, taking in account the strain tensor in 2.7, Hooke's law 2.6 becomes,

$$\sigma_{ij} = \frac{1}{2} \sum_{k=1}^3 \sum_{l=1}^3 \left[ c_{ijkl} \frac{\partial u_k}{\partial x_l} + c_{ijlk} \frac{\partial u_l}{\partial x_k} \right]. \quad (2.10)$$

With the symmetries constraints on the stiffness tensors, the four subscripts may be reduced to two and an equivalent  $6 \times 6$  matrix by using abbreviated subscript notation:

1  $\longleftrightarrow$  11, 2  $\longleftrightarrow$  22, 3  $\longleftrightarrow$  33, 4  $\longleftrightarrow$  23 or 32, 5  $\longleftrightarrow$  31 or 13 and 6  $\longleftrightarrow$  12 or 21.

For example, the relation  $\sigma_{12} = c_{1122}\varepsilon_{22}$  is replaced in abbreviated subscript notation by  $\sigma_1 = c_{12}\varepsilon_2$ . The stiffness tensor can be written in matrix notation as

$$\mathbf{C} = \begin{bmatrix} c_{11} & c_{12} & c_{13} & c_{14} & c_{15} & c_{16} \\ c_{21} & c_{22} & c_{23} & c_{24} & c_{25} & c_{26} \\ c_{31} & c_{32} & c_{33} & c_{34} & c_{35} & c_{36} \\ c_{41} & c_{42} & c_{43} & c_{44} & c_{45} & c_{46} \\ c_{51} & c_{52} & c_{53} & c_{54} & c_{55} & c_{56} \\ c_{61} & c_{62} & c_{63} & c_{64} & c_{65} & c_{66} \end{bmatrix}. \quad (2.11)$$

The stress-strain relation can be than expressed by

$$\begin{bmatrix} \sigma_{11} \\ \sigma_{22} \\ \sigma_{33} \\ \sigma_{23} \\ \sigma_{31} \\ \sigma_{12} \end{bmatrix} = \mathbf{C} \cdot \begin{bmatrix} \varepsilon_{11} \\ \varepsilon_{22} \\ \varepsilon_{33} \\ 2\varepsilon_{23} \\ 2\varepsilon_{31} \\ 2\varepsilon_{12} \end{bmatrix}.$$

Owing to the major symmetries  $c_{ijkl} = c_{ijlk}$  the independent elastic constants are further reduced to 21. This is the maximum number of independent constants for any medium [53]. Usually the number of independent constants is much less than this, because of additional restrictions imposed by symmetries of the microscopic nature of the medium. In case of anisotropic environment, all three tensors ( $\underline{\underline{\sigma}}$ ,  $\underline{\underline{\varepsilon}}$ , and  $\underline{\underline{C}}$ ) may vary from point to point inside the medium, and may vary with time as well.

Due to the before mentioned symmetries, the tensors can be represented by matrices, which is advantageous for the practical calculation or evaluation. The motion equation and elasticity law can be rewritten as

$$\rho \left( \frac{\partial^2 \mathbf{u}}{\partial t^2} \right) = \nabla \cdot \underline{\underline{C}} := \left( [\nabla \mathbf{u}]^T + \nabla \mathbf{u} \right),$$

$$\underline{\underline{\sigma}} = \underline{\underline{C}} := \underline{\underline{\varepsilon}} \quad \text{or} \quad \underline{\underline{\varepsilon}} = \underline{\underline{S}} := \underline{\underline{\sigma}}, \quad (2.12)$$

where  $\underline{\underline{C}}$  and  $\underline{\underline{S}}$  are the stiffness and compliance tensors, respectively. This reduced matrix-based approach is called Voigt notation.

To understand guided waves propagation in a complex composite structure, it is useful to briefly consider a simple configuration, i.e., an isotropic homogeneous plate in advance. Isotropic materials exhibit the same elastic properties in any direction and the stiffness tensor is invariant to any change of the axis orientation. Consequently, each component  $c_{ijkl}$  of the isotropic medium can be expressed as [54]

$$c_{ijkl} = \lambda \delta_{ij} \delta_{kl} + \mu (\delta_{ik} \delta_{jl} + \delta_{il} \delta_{jk}), \quad (2.13)$$

where  $\delta_{ij}$  means the Kronecker symbol, and  $\mu$  and  $\lambda$  are called Lamé's coefficients. Hooke's law then reduces to the well-known form

$$\sigma_{ij} = \lambda \delta_{ij} \sum_{k=1}^3 \varepsilon_{kk} + 2\mu \varepsilon_{ij}, \quad (2.14)$$

where  $\sum_{k=1}^3 \varepsilon_{kk} = \varepsilon_{11} + \varepsilon_{22} + \varepsilon_{33}$  is called trace( $\underline{\underline{\varepsilon}}$ ) and the number of independent elastic constants of the material is reduced to two [53]. From 2.11 the identities

$$\begin{aligned} c_{12} &= c_{21} = c_{13} = c_{31} = c_{23} = c_{32} = \lambda, \\ c_{11} &= c_{22} = c_{33} = \lambda + 2\mu, \quad \text{and} \\ c_{44} &= c_{55} = c_{66} = \frac{1}{2}(c_{11} - c_{12}) = \mu \end{aligned} \quad (2.15)$$

follow for the  $c_{ij}$  matrix representation of  $c_{ijkl}$ .

The other 24 of the moduli  $c_{ijkl}$  are zero since they have an odd number of distinct indices. Expressing all the components in terms of  $c_{11}$  and  $c_{12}$ , the representation of isotropic media by the reduced matrix  $\mathbf{C}$  takes the following form

$$\mathbf{C} = \begin{bmatrix} c_{11} & c_{12} & c_{12} & 0 & 0 & 0 \\ c_{12} & c_{11} & c_{12} & 0 & 0 & 0 \\ c_{12} & c_{12} & c_{11} & 0 & 0 & 0 \\ 0 & 0 & 0 & c_{44} & 0 & 0 \\ 0 & 0 & 0 & 0 & c_{44} & 0 \\ 0 & 0 & 0 & 0 & 0 & c_{44} \end{bmatrix} \quad (2.16)$$

with  $c_{44} = \frac{1}{2}(c_{11} - c_{12})$ . Lamé's coefficients completely define the elastic behavior of the isotropic material. In engineering applications, Lamé's constants are usually replaced by related elastic constants, e.g. by Young's modulus or modulus of elasticity  $E$ , and Poisson's ratio  $\nu$

$$\lambda = \frac{\nu E}{(1 + \nu)(1 - 2\nu)}, \quad (2.17)$$

$$\mu = G = \frac{E}{2(1 + \nu)}. \quad (2.18)$$

Furthermore, the parameter  $G = \mu$  is called shear modulus [57].

In isotropic case Hooke's law is much simplified, the normal and the shear stresses are summarized

$$\sigma_{ij} = \lambda \delta_{ij} \sum_{k=1}^3 \varepsilon_{kk} + 2\mu \varepsilon_{ij} = \frac{\nu E}{(1 + \nu)(1 - 2\nu)} \delta_{ij} \sum_{k=1}^3 \varepsilon_{kk} + 2\varepsilon_{ij} \frac{E}{2(1 + \nu)}. \quad (2.19)$$

The fundamental elastic wave equation, also known as Navier's equation, can be now obtained, from equations 2.5 and 2.6, taking in consideration that the stress are same in all direction, to

$$\rho \frac{\partial^2 \mathbf{u}}{\partial t^2} = (\lambda + \mu) \nabla(\nabla \cdot \mathbf{u}) + \mu \nabla^2 \mathbf{u}. \quad (2.20)$$

The most general method for solving isotropic waveguide problems makes use of the representation of the displacement velocity field by a scalar and a vector potential [57]. This approach is called Helmholtz decomposition. As a measurement of the material deformation, the displacement gradient matrix is deficient. Using Helmholtz decomposition, the displacement vector  $\mathbf{u}$  can be composed of the gradient of a scalar potential  $\Phi$  and the curl of a vector potential  $\mathbf{H}$ , of which the divergence vanishes according to the following equations:

$$\mathbf{u} = (\nabla\Phi + \nabla \times \mathbf{H}) \quad \text{and} \quad \nabla \cdot \mathbf{H} = 0. \quad (2.21)$$

In electromagnetism, the postulation  $\nabla \cdot \mathbf{H} = 0$  is known as Coulomb gauge. The Navier's equations of motion 2.20 of the isotropic medium may be rewritten as

$$\rho(\nabla \frac{\partial^2 \Phi}{\partial t^2} + \nabla \times \frac{\partial^2 \mathbf{H}}{\partial t^2}) = (\lambda + \mu)\nabla [\nabla \cdot (\nabla\Phi + \nabla \times \mathbf{H})] + \mu\nabla^2(\nabla\Phi + \nabla \times \mathbf{H}) \quad (2.22)$$

and further

$$\nabla \rho \frac{\partial^2 \Phi}{\partial t^2} + \nabla \times \rho \frac{\partial^2 \mathbf{H}}{\partial t^2} = (\lambda + \mu)\nabla \left[ \nabla \cdot \nabla\Phi + \underbrace{\nabla \cdot (\nabla \times \mathbf{H})}_0 \right] + \mu\nabla^2\nabla\Phi + \mu\nabla^2\nabla \times \mathbf{H}.$$

Applying the identities  $\nabla(\nabla \cdot (\nabla\Phi)) = \nabla(\nabla^2\Phi)$ ,  $\nabla^2\nabla = \nabla\nabla^2$  and  $\nabla(\nabla \cdot (\nabla \times \mathbf{H})) = \nabla \times (\nabla^2\mathbf{H})$ , Eq. 2.22 can be regrouped as

$$\nabla \left[ (\lambda + 2\mu)\nabla^2\Phi - \rho \frac{\partial^2 \Phi}{\partial t^2} \right] + \nabla \times \left[ \mu\nabla^2\mathbf{H} - \rho \frac{\partial^2 \mathbf{H}}{\partial t^2} \right] = 0. \quad (2.23)$$

As the first and second term of this equation describes pure gradient and vortex fields, respectively, which are linearly independent, both terms must vanish separately. This gives the classical wave equations

$$\nabla^2\Phi = \frac{1}{v_L^2} \frac{\partial^2 \Phi}{\partial t^2} \quad \text{and} \quad \nabla^2\mathbf{H} = \frac{1}{v_T^2} \frac{\partial^2 \mathbf{H}}{\partial t^2}, \quad (2.24)$$

where  $v_L^2 = \lambda + 2\mu/\rho$  and  $v_T^2 = \mu/\rho$  in case of elastic wave propagation in isotropic medium. Volume or dilatational disturbances, will propagate at the  $v_L$ , the longitudinal waves phase velocity, while shear distortions propagate with  $v_T$ . Alternative expressions in terms of Young's modulus  $E$  and Poisson's ratio  $\nu$  of the longitudinal waves phase velocity is [54]

$$v_L = \sqrt{\frac{E(1-\nu)}{\rho(1+\nu)(1-2\nu)}}. \quad (2.25)$$

The transversal or shear waves propagation velocity  $v_T$  can be also expressed in terms of  $E$  and  $\nu$ , or with the shear modulus

$$v_T = \sqrt{\frac{E}{2\rho(1+\nu)}} = \sqrt{\frac{G}{\rho}}. \quad (2.26)$$

The equations 2.24 show that the two potentials propagate independently of each other, such that waves may propagate in the interior of an elastic solid at two different speed  $v_L$  for compressional modes and  $v_T$  for shear modes. In plate medium, transversal and longitudinal waves are generated.

Contrary to the simple isotropic material, where the three different constants of the stiffness matrix rely on two independent parameters, orthorhombic or orthotropic materials require 9 independent elements. The elastic material properties are characterized by having three orthogonal axes, of direct or inverse symmetry, which are taken as the coordinate axes, in this case the stiffness tensor is given by

$$\mathbf{C} = \begin{bmatrix} c_{11} & c_{12} & c_{13} & 0 & 0 & 0 \\ c_{12} & c_{22} & c_{23} & 0 & 0 & 0 \\ c_{13} & c_{23} & c_{33} & 0 & 0 & 0 \\ 0 & 0 & 0 & c_{44} & 0 & 0 \\ 0 & 0 & 0 & 0 & c_{55} & 0 \\ 0 & 0 & 0 & 0 & 0 & c_{66} \end{bmatrix}. \quad (2.27)$$

The solution of motion Eq. 2.5 with nine independent constants is more complex. The wave velocities  $v_L$  and  $v_T$  vary with the direction.

## 2.2 Guided elastic waves

This thesis paid attention to the propagation of elastic waves in plates which are shortly called guided waves (GW) or rather Lamb waves. Defined as elastic wave propagating in bounded solids, guided waves study relies on the solution of equation of motion with boundary conditions. The term GW comprises several species of propagating elastic deformations. Associated Rayleigh wave is a wave that propagates on the traction-free surface of a semi-infinite solid [58]. Love waves exist in a half-space covered by a layer of material with different elastic properties [56]. Stoneley waves are free waves that occur at an interface between two media [59]. Lamb waves are the waves that propagate in plates with traction-free surfaces [11]. Because thin-walled structures are very commonly used, Lamb waves are of particular interest in structural health monitoring and thus, they are considered below in detail.

Guided waves (including Lamb waves) may propagate along or inside the wave guide over long distances. Derivation of the Rayleigh-Lamb equation and analysis of the Lamb wave behaviors can be found in many text books and publications [16, 53, 54, 55, 60], and will be summarized in concisely below.

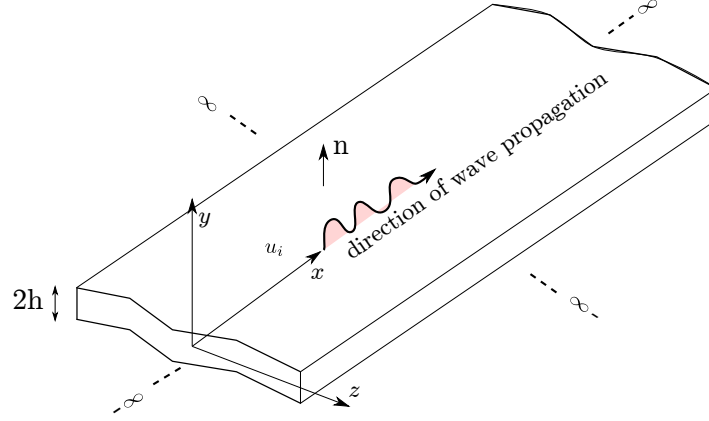
### 2.2.1 Lamb waves fundamentals

In the following discussion, a free plate with thickness  $2h$ , extending to infinity in  $x$ - and  $z$ -directions is considered [30]. The  $x$ -direction is assumed herein as the direction of propagation of a plane wave and the  $y$ -direction is the normal to the plate surface (see Fig. 2.3). Thus, we are considering primarily  $z$ -invariant solutions of the equations of motion, i.e.,  $\frac{\partial}{\partial z} = 0$  and  $\sigma_{zz} = 0$  within the plate. The free boundary condition at  $y = \pm h$  requires  $\sigma_{xy} |_{y=\pm h} = \sigma_{yy} |_{y=\pm h} = \sigma_{yz} |_{y=\pm h} = 0$ . The motion Eq. 2.5, reduces to

$$\frac{\partial \sigma_{xx}}{\partial x} + \frac{\partial \sigma_{xy}}{\partial y} = \rho \frac{\partial^2 u_x}{\partial t^2}, \quad (2.28)$$

$$\frac{\partial \sigma_{xy}}{\partial x} + \frac{\partial \sigma_{yy}}{\partial y} = \rho \frac{\partial^2 u_y}{\partial t^2}, \quad (2.29)$$

$$\frac{\partial \sigma_{xz}}{\partial x} + \frac{\partial \sigma_{yz}}{\partial y} = \rho \frac{\partial^2 u_z}{\partial t^2}. \quad (2.30)$$

Figure 2.3: Guided waves in a free boundaries plate of thickness  $2h$ .

In case of  $u_x = u_y = 0$ , Eq. 2.30 represents the equation of motion for plane shear waves, while Eqs. 2.28 and 2.29 in conjunction with  $u_z = 0$  are the equations of motion for straight Lamb waves.

Recalling the general strain-displacement relation

$$\varepsilon_{ij} = \frac{1}{2} \left( \frac{\partial u_i}{\partial x_j} + \frac{\partial u_j}{\partial x_i} \right),$$

the plate strain can be summarized as

$$\varepsilon_{xx} = \frac{\partial u_x}{\partial x}, \quad \varepsilon_{xy} = \frac{1}{2} \left( \frac{\partial u_x}{\partial y} + \frac{\partial u_y}{\partial x} \right), \quad (2.31)$$

$$\varepsilon_{yy} = \frac{\partial u_y}{\partial y}, \quad \varepsilon_{yz} = \frac{1}{2} \left( \frac{\partial u_y}{\partial z} + \frac{\partial u_z}{\partial y} \right), \quad (2.32)$$

$$\varepsilon_{zz} = 0, \quad \varepsilon_{xz} = \frac{1}{2} \left( \frac{\partial u_x}{\partial z} + \frac{\partial u_z}{\partial x} \right). \quad (2.33)$$

In case of  $u_x = u_y = 0$ , the strain of plane shear waves results while the conditions  $u_z = 0$  and  $\frac{\partial}{\partial z} = 0$  concern the strain of plane Lamb waves which is of interest here.

The most elementary definition of strain is a deformation of a solid due to stress where the stress is force per area [61]. This definition recalls the previous linearized relationship between stress and strain, where strain component is proportional to the corresponding stress component. Using Eq. 2.14, the stresses for the case of plane Lamb waves propagating in minus  $x$ -direction are expressed as

$$\sigma_{xx} = \lambda \varepsilon_{xx} + 2\mu \varepsilon_{xy} = \lambda \frac{\partial u_x}{\partial x} + \mu \left( \frac{\partial u_x}{\partial y} + \frac{\partial u_y}{\partial x} \right), \quad (2.34)$$

$$\sigma_{yy} = \lambda \varepsilon_{yy} + 2\mu \varepsilon_{xy} = \lambda \frac{\partial u_y}{\partial y} + \mu \left( \frac{\partial u_x}{\partial y} + \frac{\partial u_y}{\partial x} \right), \quad (2.35)$$

$$\sigma_{xy} = \sigma_{yx} = 2\mu \varepsilon_{xy} = \mu \left( \frac{\partial u_x}{\partial y} + \frac{\partial u_y}{\partial x} \right), \quad (2.36)$$

$$\text{and } \sigma_{zz} = \sigma_{xz} = \sigma_{yz} = 0. \quad (2.37)$$

Recalling the definition of Helmholtz decomposition with potentials  $\Phi$  and  $\mathbf{H}$  in the Eq. 2.21

$$\mathbf{u} = (\nabla\Phi + \nabla \times \mathbf{H}) \quad \text{and} \quad \nabla \cdot \mathbf{H} = 0,$$

and that plane waves that are guided in  $x$ -direction with  $z$ -invariance leads to

$$\begin{aligned} u_x &= \frac{\partial\Phi}{\partial x} + \frac{\partial H}{\partial y}, \\ u_y &= \frac{\partial\Phi}{\partial y} - \frac{\partial H}{\partial x}, \\ u_z &= \frac{\partial H}{\partial x} - \frac{\partial H}{\partial y}, \end{aligned} \quad (2.38)$$

where the last equation concerns in-plane shear waves that are not in the focus of this work.

The wave equations of the Helmholtz potentials as defined in the Eq. 2.24 are reduced for guided plane waves with  $\frac{\partial}{\partial z} = 0$  to

$$\frac{\partial^2\Phi}{\partial x^2} + \frac{\partial^2\Phi}{\partial y^2} = \frac{1}{v_L^2} \frac{\partial^2\Phi}{\partial t^2} \quad \text{and} \quad \frac{\partial^2\mathbf{H}}{\partial x^2} + \frac{\partial^2\mathbf{H}}{\partial y^2} = \frac{1}{v_T^2} \frac{\partial^2\mathbf{H}}{\partial t^2}. \quad (2.39)$$

Solutions to Eqs. 2.39 can be found by means of separation of variables the approach which take the form of harmonic waves propagating in minus  $x$ -direction

$$\Phi = \phi(y) \exp[i(kx - \omega t)] \quad \text{and} \quad \mathbf{H} = H(y) \exp[i(kx - \omega t)], \quad (2.40)$$

where  $\omega$  is the angular frequency of the local motion and  $k$  is the angular wave number.

Substitution of these solutions into Eqs. 2.39 yields equations governing the unknown functions  $\phi(y)$  and  $H(y)$

$$\frac{\partial^2\phi}{\partial y^2} + p^2\phi = 0 \quad \text{and} \quad \frac{\partial^2 H}{\partial y^2} + q^2 H = 0, \quad (2.41)$$

with

$$p^2 = \frac{\omega^2}{v_L^2} - k^2 \quad \text{and} \quad q^2 = \frac{\omega^2}{v_T^2} - k^2. \quad (2.42)$$

These equations may be rewritten as  $p^2 + k^2 = k_L^2$  and  $q^2 + k^2 = k_T^2$  where  $k_L$ ,  $k_T$  are the propagation constants of the longitudinal and transversal elastic waves in the bulk. Hence,  $p$  and  $q$  may be considered as the  $y$ -component and  $k$  as the  $x$ -component of the wave vector of the elastic waves.

The general solutions of Eqs. 2.41 are

$$\phi(y) = A_1 \sin(py) + A_2 \cos(py) \quad \text{and} \quad H(y) = B_1 \sin(qy) + B_2 \cos(qy),$$

where  $A_1$ ,  $A_2$ ,  $B_1$  and  $B_2$  are arbitrary constants which can be found from the boundary conditions, i.e., free surfaces at  $y = \pm h$ . According to Eqs. 2.38 and 2.40, the displacement components become

$$u_x = ik[A_1 \sin(py) + A_2 \cos(py)] + q[B_1 \cos(qy) - B_2 \sin(qy)], \quad (2.43)$$

$$u_y = p[A_1 \cos(py) - A_2 \sin(py)] - ik[B_1 \sin(qy) + B_2 \cos(qy)]. \quad (2.44)$$

Substituting these displacement components into the strain-displacement Eqs. 2.35 and 2.36 one gets

$$\begin{aligned} \sigma_{xy} = & \mu[-A_2 2ikp \sin py + B_1(k^2 - q^2) \sin qy \\ & + A_1 2ikp \cos py + B_2(k^2 - q^2) \cos(qy)], \end{aligned} \quad (2.45)$$

$$\begin{aligned} \sigma_{yy} = & \mu[-A_2(k^2 - q^2) \cos py - B_1 2ikq \cos(qy) \\ & + A_1(k^2 - q^2) \sin py + B_2 2ikq \sin qy]. \end{aligned} \quad (2.46)$$

A mirror-symmetric solution requires

$$\begin{aligned} u_x(x, -h) &= u_x(x, h), & \sigma_{yx}(x, -h) &= -\sigma_{yx}(x, h), \\ u_y(x, -h) &= -u_y(x, h), & \sigma_{yy}(x, -h) &= \sigma_{yy}(x, h). \end{aligned}$$

Similar, for the antisymmetric solution of the plane wave equations

$$\begin{aligned} u_x(x, -h) &= -u_x(x, h), & \sigma_{yx}(x, -h) &= \sigma_{yx}(x, h), \\ u_y(x, -h) &= u_y(x, h), & \sigma_{yy}(x, -h) &= -\sigma_{yy}(x, h). \end{aligned}$$

Recalling that the top and bottom surfaces of the plate are free surfaces, the boundary conditions at the free surfaces of the plate are  $\sigma_{xy}|_{y=\pm h} = \sigma_{yz}|_{y=\pm h} = \sigma_{yy}|_{y=\pm h} = 0$ . In combination with Eq. 2.46 these boundary conditions lead to the Rayleigh–Lamb frequency equations as they can be found in [30]

$$\frac{\tan(ph)}{\tan(qh)} = - \left[ \frac{4k^2 pq}{(k^2 - q^2)^2} \right]^{\pm 1}, \quad (2.47)$$

where +1 applies for symmetric modes, and -1 applies for anti-symmetric modes. The terms symmetric and antisymmetric are used with respect to the direction of propagation, in this case the  $x$ -direction, and describe the amplitude distribution over the plate thickness. The thickness of the waveguide accounts for  $2h$  and the left hand side of Eqs. 2.47 varies according to the product  $\omega \cdot h$  as can be seen from Eqs. 2.42.

Solutions for the Rayleigh–Lamb equations can be found, e.g., for a given  $\omega$  only numerically where, with the exception of low frequency-thickness products, multiple solutions exist for each Eq. 2.47. The transcendent Eqs. 2.47 implies also that the phase velocity  $v_\varphi = \omega/k$ , is a distinct nonlinear function of  $\omega$  for each mode. Hence, Lamb waves are dispersive, which means that their phase and group velocities vary with frequency as can be seen from Fig. 2.4.

Considering the wave equations 2.40, the elastic perturbation propagates along  $x$ -axis, i.e.,  $u_j = U_j \exp i(kx - \omega t)$ , where  $U_j$  represents the complex particle displacement amplitudes in  $x$ ,  $y$  directions. The phase  $\varphi$  of a wavefront is defined by

$$\varphi = kx - \omega t = \text{const.} \quad (2.48)$$

With no loss of generality, one may choose  $\varphi = 0$  which leads immediately to the propagation velocity of a point of constant phase  $\varphi$

$$v_\varphi = \frac{\omega}{k}, \quad (2.49)$$

where  $v_\varphi$  is called the phase velocity.  $|k| = \omega/|v_\varphi| = 2\pi/\lambda$  is the angular wave number measured along the wavefront normal. The term  $k \cdot x$  measures, at a given time, the phase difference of the disturbance at point  $x$ , relative to the origin  $x = 0$ .

**Group velocity** The group velocity is associated with the propagation velocity of a group of waves of similar frequencies (wave strain). Practically, the propagation velocity of the carrier is the phase velocity  $v_\varphi$  while the propagation velocity of the modulation envelope is the group velocity  $v_g$  defined as

$$v_g \equiv \frac{\partial \omega}{\partial k}. \quad (2.50)$$

$v_g$  may be obtained from

$$\frac{\partial v_\varphi}{\partial k} = \frac{\partial}{\partial k} \left( \omega \cdot \frac{1}{k} \right) = \frac{1}{k} \frac{\partial \omega}{\partial k} - \frac{\omega}{k^2},$$

which transforms into

$$\frac{\partial \omega}{\partial k} = v_g = v_\varphi + k \frac{\partial v_\varphi}{\partial k} = v_\varphi + k \frac{\partial v_\varphi}{\partial \omega} \frac{\partial \omega}{\partial k}$$

and with rearrangement of terms

$$v_g = \frac{\partial \omega}{\partial k} = v_\varphi \left( 1 - k \frac{\partial v_\varphi}{\partial \omega} \right)^{-1} = v_\varphi \left( 1 - \frac{\omega}{v_\varphi} \frac{\partial v_\varphi}{\partial \omega} \right)^{-1} \equiv v_\varphi \left( 1 - \frac{f \cdot h}{v_\varphi} \frac{\partial v_\varphi}{\partial (f \cdot h)} \right)^{-1}.$$

The group velocity is equal to phase velocity only if the the derivative of  $v_\varphi$  with respect to  $\omega$  becomes zero and  $v_g \geq v_\varphi$  for  $\partial v_\varphi / \partial \omega \geq 0$ . Phase velocity and group velocity dispersion curves can be drawn as functions of the  $f \cdot h$  product in Fig. 2.4.

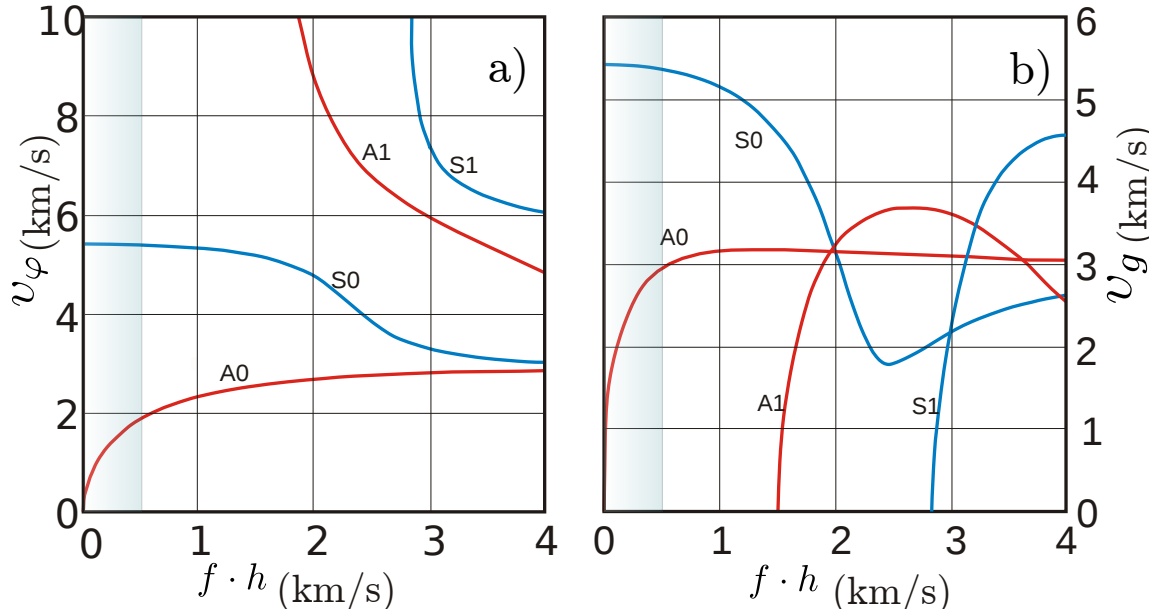


Figure 2.4: Dispersion curves for a traction free aluminum plate: a) phase velocity dispersion curves; b) group velocity dispersion curves.

**Damping and Attenuation** In general, attenuation decreases as the medium becomes more ordered as the representation of atomic interaction by uniform mechanic parameters becomes nonlinear [57]. The two major sources of GW attenuation are absorption due to

matrix loss and ultrasound path scattering from material inhomogeneities. Matrix loss can be taken into account introducing a loss term into Hooke's law

$$\sigma_{ij} = \sum_{k=1}^3 \sum_{l=1}^3 (c_{ijkl} \varepsilon_{kl} + \eta_{ijkl} \frac{\partial \varepsilon_{kl}}{\partial t}) \quad (2.51)$$

where  $\eta_{ijkl}$  is called viscosity tensor. The symmetry of  $\sigma_{ij}, \varepsilon_{ij}$  limits the number of independent components of  $\eta_{ijkl}$  applying the same restrictions as for the elastic constants  $c_{ijkl}$ . Considering Hooke's law Eq. 2.51, the motion wave equation becomes

$$\rho \frac{\partial^2 \mathbf{u}}{\partial t^2} = \sum_{i=1}^3 \sum_{j=1}^3 \sum_{k=1}^3 \sum_{l=1}^3 \left[ c_{ijkl} \frac{\partial^2 \mathbf{u}}{\partial x_j \partial x_k} + \eta_{ijkl} \frac{\partial^3 \mathbf{u}}{\partial x_i \partial x_k \partial t} \right]. \quad (2.52)$$

Moreover, the scattering of waves causes a decrease in amplitude with increasing travel distance, where the characteristic frequency is determined by a characteristic spatial scale, such as the correlation length of random media or the crack length. Perturbation of the different elastic parameters produce characteristic radiation patterns. The scattering attenuation depends not only on wave frequency but also on scatterer size and position.

**Reflection and refraction** Reflection and refraction at boundaries and interfaces profoundly affect or enable Lamb waves excitation. Wave reflection and refraction considerations are fundamental to the study of stress wave propagation in layered solids. Considering an incident harmonic plane wave traveling in an minus  $x$ -direction, propagating in adjoining half space; an interface between two media in Fig. 2.5, the wave equation can be expressed for either longitudinal or shear waves

$$\frac{\partial \mathbf{u}^I}{\partial x^2} = \frac{1}{v_L^2} \frac{\partial \mathbf{u}^I}{\partial t^2} \quad \text{or} \quad \frac{\partial \mathbf{u}^{II}}{\partial x^2} = \frac{1}{v_T^2} \frac{\partial \mathbf{u}^{II}}{\partial t^2}, \quad (2.53)$$

where  $\mathbf{u}^I$  and  $\mathbf{u}^{II}$  are displacement vectors along the  $x$ -axis, in media I and II respectively. For an incident longitudinal wave  $u_1^I = I e^{i(k_1 x - \omega t)}$  with  $k_1 = \omega/v_L^{(1)}$ , the reflected and transmitted displacement amplitude can be written respectively as

$$u_1^{(R)} = A_R e^{-i(k_1 x + \omega t)} \quad \text{and} \quad u_1^{(T)} = A_T e^{i(k_1 x + \omega t)}, \quad (2.54)$$

here,  $A_R$  and  $A_T$  are can be deduced from the boundary condition at the interface.

When plane elastic waves obliquely impinge on a plane interface between two media as shown in Fig. 2.5, secondary waves (refracted and transmitted portions) are excited to meet the boundary conditions there. The transmitted wave has a different angle from the incident one which is called wave refraction. The detailed circumstances depend on the incident angle of the wave as well as the material properties of the two media. Reflection and refraction are basically caused by different stiffness tensors of the media. For known isotropic materials, the refraction angle can be calculated from the equivalent of Snell's law that relies on equal propagation along the interface of elastic perturbations at both sides of the plane interface. For complex cases, like the interface between differently oriented anisotropic materials, the boundary condition of continuous variation of displacement and stress components determines the relations. Matching such boundary conditions requires a superposition of multiple modes of elastic waves. If some of these extra modes are not evanescent, mode conversion, that is the emergence of a different type of wave occurs. For example, a longitudinal wave

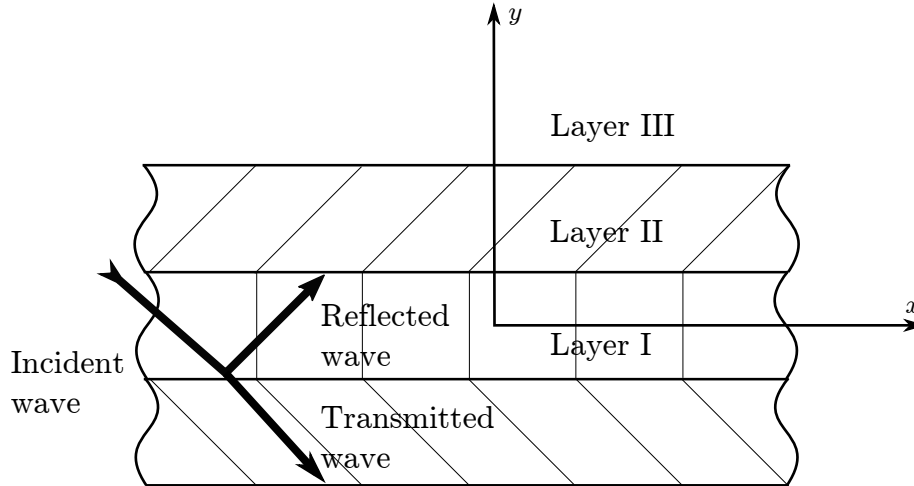


Figure 2.5: Elastic wave propagating in layered structure.

incident on an interface between two different solids is transmitted partially as a refracted longitudinal wave and partially as a mode converted shear wave in the solid. It should be noted that any type of wave can be converted to another type, e.g. from a shear wave to a longitudinal wave, and vice versa. The angles of reflection and refraction even in case of mode conversion can be calculated from adapted Snell's laws.

## 2.3 Generation of Lamb waves with piezoelectric actuators

There are several ways to excite Lamb waves in a material [30, 62, 63, 64, 65]. One of the most crucial problems, when generating Lamb waves using actuators, is the control of the actually excited modes. In order to have a clear view of generating modes, simple mechanical excitations have been found. Some of these devices are ultrasonic probes, lasers, and piezoelectric elements. A partial solution to this complexity is the use of transducers that excite only a single mode or a minimum number of modes. Various strategies have been employed to this end:

- Guo and Cawley proposed in [13] the ultrasonic wedge method which has the advantage to excite a single mode Lamb wave but is also single directional.
- Air-coupled transducers are mainly limited by the poor coupling of energy from the transducer to the sample due to the large air/solid impedance mismatch [49].
- Electromagnetic acoustic transducers (EMATs) have restrictions on the applicable frequency range and they require electrical conductivity of the plate [54].
- Contactless Lamb wave generation by lasers can target a dominant mode [63]. The optical method is based on a thermal excitation of acoustic vibrations by heating with a powerful laser where its intensity is modulated at the desired frequency  $f$ . A drawback of optical excitation is that the efficiency of Lamb wave generation decreases quickly with frequency. In addition, the optic infrastructure is expensive.

- Affixed piezoelectric transducers are versatile devices for Lamb wave generation. High force output and broadband transfer characteristics are the benefits of piezoelectric actuators. However, they produce small static displacement which can be considered as serious drawback [30].

**Piezoelectric actuator** Certain materials become electrically polarized when they are strained. A prerequisite for this piezoelectric effect is the existence of ionic bonds in the unit cell of a crystal lacking an inversion symmetry. The piezoelectric transduction is reversible as electrically induced polarization causes deformation of the material. This is called the inverse piezoelectric effect. A piezoelectric material has the property of undergoing mechanical displacement when an electric field is applied.

Modeling of piezoelectric actuators is based on the governing equations of the electro-elastic behavior of piezoelectric continua. The constitutive piezoelectric equations couple mechanical stress  $\sigma_{ij}$ , mechanical strain  $\varepsilon_{ij}$ , dielectric displacement  $D_i$ , and the electric field  $E_j$ . Noted in the stress-charge form they are given by [66]

$$\varepsilon_{ij} = \sum_k \sum_l s_{ijkl} \sigma_{kl} - d_{kij} E_k, \quad (2.55)$$

$$D_i = \sum_j \sum_k d_{ijk} \sigma_{jk} + \sum_k \epsilon_{ik} E_k, \quad (2.56)$$

where  $\underline{\underline{S}} = (\underline{\underline{C}})^{-1}$ , with the tensor components  $s_{ijkl}$ ,  $d_{ijk}$ ,  $d_{kij} = (d_{ijk})^T$  and  $\epsilon_{ik}$  are the elastic compliance tensor, the direct and converse piezoelectric strain tensors, and the permittivity tensor, respectively. Equations 2.55 and 2.56 may be written in reduced matrix form, the Voigt notation, where  $1 \longleftrightarrow 11$ ,  $2 \longleftrightarrow 22$ ,  $3 \longleftrightarrow 33$ ,  $4 \longleftrightarrow 23$  or  $32$ ,  $5 \longleftrightarrow 31$  or  $13$  and  $6 \longleftrightarrow 12$  or  $21$  is set. For a piezoelectric ceramic such as PZT (Lead zirconate titanate)<sup>2</sup> with poling direction parallel to the 3 coordinate. The equations read in matrix form

$$\begin{bmatrix} \varepsilon_1 \\ \varepsilon_2 \\ \varepsilon_3 \\ \varepsilon_4 \\ \varepsilon_5 \\ \varepsilon_6 \end{bmatrix} = \begin{bmatrix} s_{11}^E & s_{12}^E & s_{13}^E & 0 & 0 & 0 \\ s_{12}^E & s_{22}^E & s_{13}^E & 0 & 0 & 0 \\ s_{13}^E & s_{13}^E & s_{33}^E & 0 & 0 & 0 \\ 0 & 0 & 0 & s_{44}^E & 0 & 0 \\ 0 & 0 & 0 & 0 & s_{55}^E & 0 \\ 0 & 0 & 0 & 0 & 0 & s_{66}^E \end{bmatrix} \begin{bmatrix} \sigma_1 \\ \sigma_2 \\ \sigma_3 \\ \sigma_4 \\ \sigma_5 \\ \sigma_6 \end{bmatrix} + \begin{bmatrix} 0 & 0 & d_{31} \\ 0 & 0 & d_{31} \\ 0 & 0 & d_{33} \\ 0 & d_{15} & 0 \\ d_{15} & 0 & 0 \\ 0 & 0 & 0 \end{bmatrix} \begin{bmatrix} E_1 \\ E_2 \\ E_3 \end{bmatrix}$$

$$\begin{bmatrix} D_1 \\ D_2 \\ D_3 \end{bmatrix} = \begin{bmatrix} 0 & 0 & 0 & 0 & d_{15} & 0 \\ 0 & 0 & 0 & d_{15} & 0 & 0 \\ d_{31} & d_{31} & d_{33} & 0 & 0 & 0 \end{bmatrix} \begin{bmatrix} \sigma_1 \\ \sigma_2 \\ \sigma_3 \\ \sigma_4 \\ \sigma_5 \\ \sigma_6 \end{bmatrix} + \begin{bmatrix} \epsilon_{11} & 0 & 0 \\ 0 & \epsilon_{11} & 0 \\ 0 & 0 & \epsilon_{33} \end{bmatrix} \begin{bmatrix} E_1 \\ E_2 \\ E_3 \end{bmatrix},$$

where  $s_{66}^E = 2(s_{11}^E - s_{12}^E)$  and the superscript  $E$  indicates that the coefficient applies for constant electric field strength.

It turns out that the actuated strains are directly proportional the mechanical/electrical coupling coefficient  $d_{ij}$  and an applied time-varying electrical field  $E(t)$  over a broad frequency range. The generation of Lamb waves by lightweight piezoelectric transducers permanently glued to the structure is very frequently used [67]. Technically applied sheets of

<sup>2</sup>The chemical formula of PZT is  $\text{Pb}[\text{Zr}_x\text{Ti}_{1-x}]\text{O}_3$  with  $(0 \leq x \leq 1)$ .

material allow a good integration or attachment of the small and lightweight piezoelectric elements. The ability to efficiently generate Lamb waves and the possibility to control the preferably excited modes by suited excitation frequencies have been demonstrated in [30].

Today, many companies offer a broad range of actuators based on piezoelectric ceramics for applications such as monitoring of structure by Lamb wave detection. The most of these actuators are based on the previous described principles.

By applying a homogeneous electrical field along the polarization axis of a piezoelectric material Fig. 2.6, polarization charges are generated at the respective surfaces on the one hand and mechanical strain on the other hand.

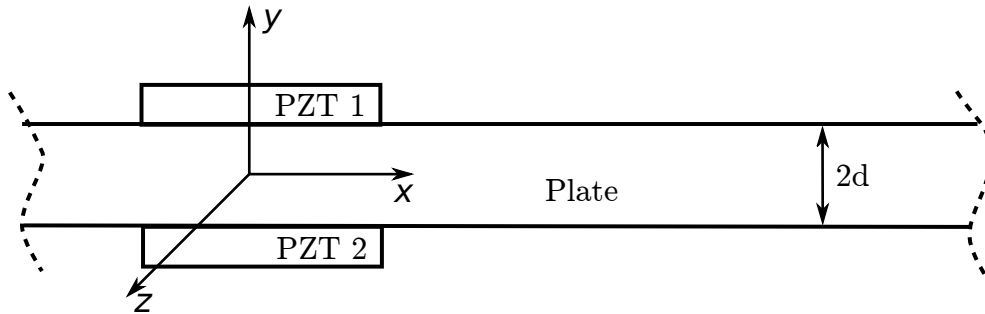


Figure 2.6: Circular piezoelectric actuator on the plate structure.

It results that the electric field inside the piezoelectric material is homogeneous and equal to the time-varying potential difference  $V(t)$  applied to the plate divided by the thickness of the plate  $d$

$$E_3(t) = \frac{V(t)}{d}.$$

Under the influences of the applied electrical field parallel to the direction of polarization, the piezoelectric materials expand and contract in the radial and polarization directions as shown in Fig. 2.7 or vice versa depending on the sign of  $V(t)$ . Assuming the strain distribution through the piezoelectric actuator and a linear strain distribution through the plate material, this induces a strain or displacement in the direction of polarization and the perpendicular direction. The piezoelectric slab deforms due to the  $d_{33}$  coefficient along the polarization direction as well as perpendicular to this direction due to the  $d_{31}$  coefficient. If the slab is

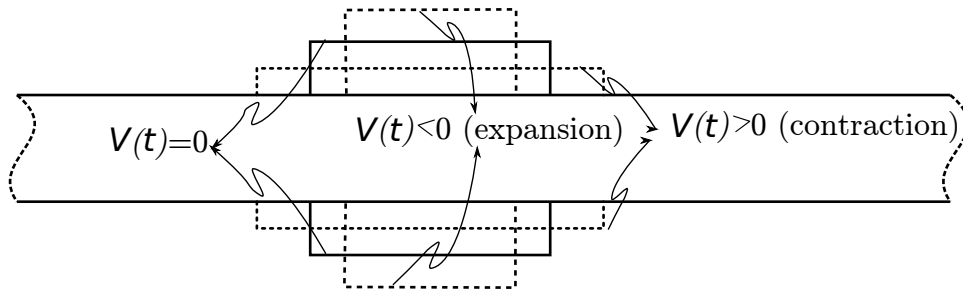


Figure 2.7: Piezoelectric actuator deformations under the influence of an electrical signal  $V(t)$ .

mounted on a surface perpendicular to the  $z$ -direction, the transversal deformation exerts

reaction forces on the host plate through the bonding layer. Appropriate signals  $V(t)$  may excite circular crested elastic waves in the host plate.

## 2.4 Composite materials

A composite material is a combination of several materials, whose combined properties are typically superior to those of the separated constituents. Technical constitution of the composite material are commonly classified in the following the main components: a type of matrix or filling material (polymer, ceramic, metal) and a reinforcement (fiber, whiskers, particulate, flake). The geometries and orientation or the nature and arrangement of the constituent phases help also by classification of composite materials. Distinction can be made between thermoset (polyester, phenolformaldehyde, epoxy, polyimide, etc); thermoplastic (thermosoftening polymers)<sup>3</sup>, carbon and metal composite.

Considering a fiber reinforced composite, the subclassification of composite is performed with fiber forms (unidirectional, cloth, randomly with continuous or chopped fibers, etc.). The matrix has to merge with the chosen reinforcing to provide the integrity of the composite material. The matrix must possess sufficient stiffness to provide uniform loading of all the fibers. The role of the matrix resin is to hold the fibers in their position, protect the fibers from abrasion and corrosion, and to transfer load between fibers. The primary role of the fibers is to provide strength and high stiffness to the composite. Typical reinforcing fiber materials are glass, carbon and aramid, with fiber diameters in the range of 6 – 14  $\mu\text{m}$ . As multiphase materials, fiber reinforced composites exhibit distinct anisotropic properties. Their material capabilities, largely related to manufacturing processes, are diverse. Furthermore, the mechanisms of flaw initiation, spreading over the composite volume, and the ultimate failure are very complicated.

Composite materials are nowadays widely used in laminated sheet form in the aerospace industry. In this work, unidirectional carbon fiber reinforced polymers composites (CFRP) are highlighted. CFRP satisfy the tree following properties, the light weight and high stiffness and strength. Delamination failure, one of the limits of these materials, can be detected with guided elastic waves. Due to the inherent anisotropic characteristics of stacked CFRP layers, the modeling of related elastic waves is complicated.

### 2.4.1 Technical aspects

CFRP made of a stack of unidirectional fiber-reinforced composite ply, shown in Fig. 2.9 is used for the simulation part of this work. CFRP is a composite material consisting of carbon fiber and polymer matrix. The coordinate system used to describe the single ply is labeled as 1-2-3 axes. In this case, the 1-axis is defined to be parallel to the fibers ( $0^\circ$ ), the 2-axis is defined to lie within the plane of the plate and is perpendicular to the fibers ( $90^\circ$ ), and the 3-axis is defined to be normal to the plane of the plate. If the ply is loaded parallel to the fibers, the modulus of elasticity  $E_{11}$  approaches that of the fibers corrected with the filling factor. If the plate is loaded perpendicular to the fibers in the two- or 90-degree direction, the modulus  $E_{22}$  is much lower, approaching that of the relatively compliant matrix. Since  $E_{11} \gg E_{22}$  and the material strength varies, depending of the loading direction within the material, CFRP with different unidirectional fiber direction ply, is strongly anisotropic. Typically several

---

<sup>3</sup>Thermoset are fabricated from resin, a curing agent lowering the viscosity and improving impregnation of reinforcement. It becomes cross linked during fabrication and do not soften upon reheating. The thermoplastics soften upon heating and can be reshaped with heat and pressure.

layers of procured unidirectional CFRP are stacked with changing fiber orientation prior to the final curing which bonds these layers together. This procedure assures that there are no preferred directions of weak mechanical performance. The adhesion or bonding between matrix and fiber serve to transfer of load and its is necessary for achieving high levels of mechanical properties of the composite.

Loading in unidirectional CFRP influences the fiber as well as in the thickness direction, hence, a ply of unidirectional fiber CFRP has orthotropic material properties. Unidirectional fiber composites are a special class of orthotropic materials in which the fiber reinforcements are orientated in a single direction. Orthotropic materials have three mutually perpendicular axes of symmetry, and a load applied parallel to these axes produces only normal strains. Such orthotropic materials require 9 independent elastic moduli in their constitutive matrices, i.e., the CFRP can be characterized by 9 constants namely,  $E_{11}$ ,  $E_{22}$ ,  $E_{33}$ ,  $G_{12}$ ,  $G_{13}$ ,  $G_{23}$ ,  $\nu_{12}$ ,  $\nu_{13}$ , and  $\nu_{23}$ . Since the fiber orientation is 1-2 plane, some simplification are possible:  $E_{22} = E_{33}$ ,  $G_{12} = G_{13}$  and  $\nu_{12} = \nu_{13}$ .

## 2.4.2 Simplified models of anisotropic reinforced materials

The simplest method of estimating the stiffness of a single ply with unidirectional fiber reinforcing is to assume that the structure is simply composed of two components which are perfectly bonded together so that they deform together. Assuming the fibers are uniformly distributed in the matrix and are perfectly aligned. There is perfect bonding between fibers and matrix. The elastic Young moduli of the matrix and reinforcement are  $E_m$  and  $E_f$ , respectively. When this composite is loaded in a direction parallel to its fiber ( $x$ -axis) for example (see Fig. 2.8), the longitudinal modulus  $E_{11}$  and the transversal modulus  $E_{22}$  can

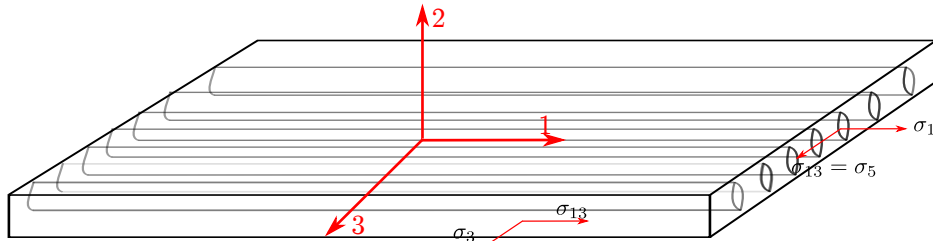


Figure 2.8: Unidirectional continuous fiber composite.

be estimated from its constituent properties by using what is known as the rule of mixtures

$$E_{11} = E_f V_f + E_m V_m, \quad (2.57)$$

$$\frac{1}{E_{22}} = \frac{1}{E_f} + \frac{1}{E_m}, \quad (2.58)$$

where  $V_f$  is the fiber volume percentage and  $V_m$  is the matrix volume percentage. The elastic modulus of the composite is determined by assuming that the applied transverse stress is equal in both the fiber and the matrix. The precedent estimation is more complex in case of discontinuity or multi-directional fiber contents. The Poisson ratio  $\nu$  of a fiber reinforced material is defined as the (negative) ratio of the lateral strain  $\varepsilon_2$  when a stress is applied in the longitudinal direction, divided by the longitudinal strain  $\varepsilon_1$ , i.e.,  $\nu_{12} = -\varepsilon_2/\varepsilon_1$ . By means of arguments similar to those above for the determination of  $E_{11}$ , it can be shown that for a stress applied in the  $y$ -direction only, the major Poisson ratio  $\nu_{12}$  is given by

$$\nu_{12} = \nu_f V_f + \nu_m V_m,$$

with  $\nu_f$  and  $\nu_m$  are Poisson ratio of of the fiber and of the matrix, respectively. The fiber and matrix assumed to be isotropic materials. Furthermore, the minor Poisson ratio must be related to  $\nu_{12}$  by the equation

$$\nu_{21}/E_{22} = \nu_{12}/E_{11}.$$

An other rule of mixture expressions for lamina properties include those for the shear modulus  $G_{12}$

$$\frac{1}{G_{12}} = \frac{1}{G_f} + \frac{1}{G_m}.$$

The composite stiffness can be characterized with mechanical (tangent to initial stress-strain slope) and ultrasonic (speed of wave through the medium) methods.

### 2.4.3 CFRP Laminates

The investigated CFRP samples are laminates that consist of multiple layers of the described unidirectional reinforced material. Typically, the direction of fibers is altered from layer to layer to avoid preferential directions of failure and to reduce the mechanical anisotropy of the full layered stack. The corresponding geometric equations for transformation of strains in the reference coordination system of each ply into the 1,2,3 coordinations take the ply's number and angle position into account. Using a sufficient number of layers, the complete laminate approximates the behavior of an orthotropic material. It is sometimes useful to approximate the mechanical properties of such laminates of unidirectional layers with a substitute material featuring nearly equivalent mechanical properties but orthotropic symmetry.

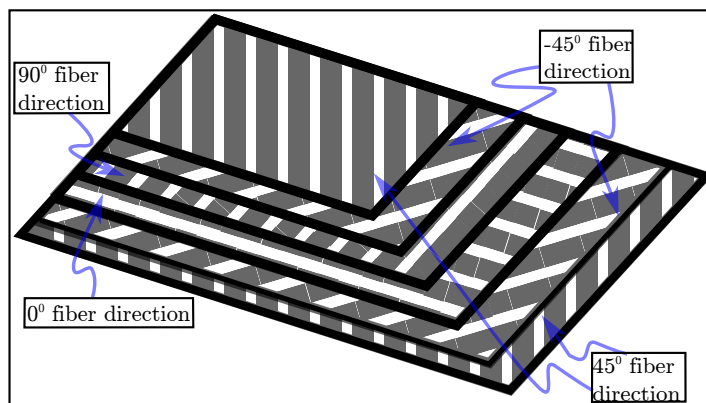


Figure 2.9: Six layered [-45/45/0/90/45/-45] CFRP.

The Austrian company FACC's product "Lower skin standard layup" (product's number 7110006) of 6 layers with layup sequence -45/45/0/90/45/-45 is simulated. The parameter details of this material are summarized in Tab. 2.1.

Material: 977-2 HTS		Reference: AS CM 3213-2003		
Data	Mean value	B-Value <sup>4</sup> 70°C	B-Value -55°C	Remark
$E_{11}$ [GPa]	135	111	111	Modulus of elasticity
$E_{22}$ [GPa]	8.55	6	6	Modulus of elasticity $\perp$
$\nu_{12}$	0.35	0.35	0.35	Poisson's ratio
$G_{12}$ [GPa]	4.2	2.5	2.5	Shear modulus
$G_{23}$ [GPa]	3.5	2.9	2.9	Shear modulus
$G_{13}$ [GPa]	5	3.3	3.3	Shear modulus
$\sigma_{11T}$ [GPa]		1.67	1.67	Tension strength
$\sigma_{11C}$ [GPa]		8.85	1.08	Compression strength
$\sigma_{22T}$ [GPa]		0.25	0.55	Tension strength $\perp$
$\sigma_{22C}$ [GPa]		1.3	1.7	Compression strength $\perp$
$\sigma_{12}$ [GPa]		0.6	0.7	Shear strength
$\sigma_{13}, \sigma_{23}$ [GPa]		0.5	0.55	Shear strength
$\varepsilon_{11T}, \varepsilon_{22T}$		0.45%	0.45%	Ultimate tensile strain
$\varepsilon_{11C}, \varepsilon_{22C}$		0.40%	0.40%	Ultimate compressive strain
$\alpha_{11}$	0.09			Thermal expansion coef.
$\alpha_{22}, \alpha_{33}$	33.5			Thermal expansion coef. $\perp$
$\rho$ [Kg/m <sup>3</sup> ]	1600	1600	1600	Density
Thickness	0.125 mm			for $V_f=60\%$

Table 2.1: Parameters of 6 layers lower skin layup of Austrian Company FACC.

### 2.4.4 Lamb waves propagation in composite material

In materials comprising multiple layer structure, the mode characteristics of propagating elastic perturbations are much more complex to analyze. Especially in fiber reinforced stratified materials, any elastic perturbation is subjected at the internal discontinuity interfaces. Furthermore, the amplitude may decrease during propagation because the interactions between the atoms or molecules are not purely elastic. Typically, such losses increase rapidly with frequency. The Lamb wave dispersion equations given above are specific to the case of a flat isotropic plate in vacuum. The transmission of the wave between different media necessitates certain elementary boundary conditions at the interfaces. Several approaches to model wave propagation in general layered media systems are possible. These analysis have been done by numerous researchers [16, 27, 53, 56]. A detailed description of the global matrix method may be found in [53].

The main advantages of composite materials are their high strength and stiffness, combined with low density, when compared with bulk materials, allowing for a weight reduction in the finished part. Composites exhibit high heat absorption capacity, resistance to thermal shock and high resistance to damage. Beside flaw detection, the high cost, the inability of the composite materials to be reused are the associated disadvantages.

## 2.5 Summary and conclusion

The chapter started with fundamentals of elastic waves and their propagation between free surfaces as guided Lamb waves. Group velocity, damping, attenuation, refraction and reflection at structure are used for Lamb waves analysis. Deformations in isotropic solids are

characterized by only two constants: Young's modulus, and Poisson's ratio (ratio of lateral to axial strain).

Lamb wave generation from a pair of piezoelectric actuators has been selected as the best choice from the long list of ways to launch these waves in a material. Due to their high-frequency response behavior and essentially infinite resolution, piezoelectric actuator materials have mechanical simplicity, small volume, light weight, large useful bandwidth, efficient conversion between electrical energy and mechanical energy, and can be easily mounted surface structures for Lamb wave production. Being bonded to the structure, the actuator produce bending strains which is communicated to the structure.

The last part of the chapter gives a sneak look at composite material, especially to CFRP laminates, using as orthotropic material. Lamb waves propagation in the layered material is analyzed.

# Chapter 3

## Fiber-Optic waveguides for sensing

Fiber-optic transduction system comprises a source of light, a fiber section of interaction and transmission, a photodetector, and analog or digital signal processing means. The excellent immunity to various electromagnetic interferences enable applications in places of high electromagnetic distortions. The sensitivity of the guided light propagation constants to, e.g., strain and temperature make of the fiber based transduction candidate for sensing. The detection of changes of optical properties like polarization, intensity, or relative phase enables conclusions about measurands interacting with the optical transducer elements. The fiber strain dependence may be used to sense mechanical deformations, which makes fiber-optic transduction interesting for SHM. The variation of the propagation speed of light waves due to stretching of a given fiber section is an intrinsic effect of the guidance of optical waves by dielectric fibers that delivers an integral mean value with respect to the total propagation time. Moreover, modified portions of a fiber acting, by FBG e.g., as distributed reflector may be used for quasi local sensing. Due to the high frequencies of usual used source (infrared or visible light) the extremely low response time of fiber optical sensors is limited either by the dynamics of optoelectronic detectors or the ratio of length of the interaction to the guided light velocity.

In this chapter a brief review of the performance, classification and the possible applications of some of the most popular or promising fiber-optic sensor technologies will be given and a description of the sensing characteristics of related fiber configurations for Lamb waves detection. The interaction of circular bent fiber and incident plane Lamb waves is analyzed. The applied waves can be characterized by straight or circular fronts, depending on localized or distributed actuation as well as on the distance between actuator and transducer. Moreover, the types of light source and photodetectors most suitable for use in fiber-optic transduction of elastic waves are identified.

### 3.1 Light source and detectors

Although there is a multitude of ways to generate light, in almost all fiber-optic systems, an optoelectronic semiconductor device is used for this purpose. The advantages of semiconductor based light sources are: compact size, high efficiency, good reliability, suitable wavelength range, emission area compatible with small monomode fiber core dimensions, and, if desired, possibility of direct modulation at relatively high frequencies. Compared with the semiconductor laser, the light-emitting diode (LED) has typically a lower output power and greater spectral width. Light is guided along the core of fiber. If it enters at one

of the end faces within an angular cone defined by the acceptance angle<sup>1</sup>  $\theta_A$ , determined only by the index of refraction

$$NA = n \sin \theta_A = \sqrt{n_f^2 - n_c^2},$$

where  $n$  is the refractive index of the medium the light is traveling before entering the fiber;  $n_f$  is the refractive index of the fiber core and  $n_c$  is the refractive index of the cladding.

Depending on the semiconductor type, superluminescent LEDs can provide appreciable light output in various spectral regions from UV to near infrared, as the 850 nm, 1300 nm and the 1550 nm windows that are popular for optical waveguides. Superluminescent LEDs feature a coherence length of the order of 10  $\mu\text{m}$  which is sufficient for many interferometric transduction schemes [68].

In basic terms, the light transmitted down the fiber can be consider as being repeatedly reflected at the core/cladding interface. According to Snell's law ( $\sin \theta_1 / \sin \theta_2 = v_1 / v_2 = n_2 / n_1$ ), this reflection is dependent on the angle  $\theta$  measured from the normal to the interface. When the critical angle is not exceeded, the light will experience total reflexion at the fiber core-to-cladding interface and remains confined inside the core of the fiber-optic. For more inclined incidence, a part of the light wave will be transmitted to the cladding and gets lost. Sufficiently coherent light source (i.e. LED, laser) can be successfully used to perform interferometric strain measurements. A drawback of the basic interferometer is emission instability evoked by waves back reflected into the source. To reduce this, effect low coherence superluminescent LED is used in this work together with an optical isolator.

The end of the fiber-optic sensor system, photodetectors (PD), convert optical power incident upon its receiver surface into current/voltage that is measured electronically. It should have high sensitivity, fast response, low noise, low cost, easy adaptation to fiber ends, and high reliability. The ideal photodetector would be sufficiently small, highly efficient, add no noise to the signal, respond uniformly to all desired wavelengths, would not limit the signal speed, and would be perfectly intensity-linear. From the range of available photodetectors, including photoconductors, phototransistors, vacuum photoemissive devices, and pyroelectric devices, only the semiconductor photodiode meets the set of properties sufficiently to be considered for use in combination with monomode fiber-optic [69, 70] and are fast converging intensities.

Equipped with fiber coupled connector and possessed high response within 1.1 - 1.6  $\mu\text{m}$  wavelength, the used InGaAs PIN Photodiode (see Fig. 3.1) (PD-1375s-ip from Roithner LaserTechnik GmbH) in this work have a large photo-sensitive diameter of 120  $\mu\text{m}$ .



Figure 3.1: Photodiode InGaAs PD-1375s-ip from Roithner LaserTechnik GmbH.

<sup>1</sup>The Numerical Aperture  $NA$  is related to the acceptance angle  $\theta_A$ , which indicates the size of a cone of light that can be accepted by the fiber.

The fundamental mechanism behind photodiode detection are such processes of optical absorption where, e.g., free movable charge carriers were produced in pairs. Generated carriers are separated by built-in or externally applied electric fields according to their type. This results in a photocurrent ( $I_p$ ) that is mostly proportional to the incident optical power  $P_R$  or intensity. The proportionality constant  $R = I_p/P_R$  is the responsivity  $R$  of the photodetector. This is plausible as the production of each free carrier requires a specific amount of energy and the density of carriers is mostly proportional to the carrier generation rate. Since the number of photons per second incident on the detector is power divided by the photon energy, and the number of electrons per second flowing in the external circuit is the photocurrent divided by the charge of the electron, it follows that the quantum efficiency  $\eta$ =electrons/incident photons is related to the responsivity by

$$\eta = R \cdot hc/q\lambda. \quad (3.1)$$

$\eta = 1$  means that a single free carrier or an electron-hole pair is generated each time a photon hits the semiconductor.

## 3.2 Fiber-optic sensing

Low cost, small cross section, large bandwidth, and low attenuation make optical waveguide fibers to ideal signal transmitters over long distances. Due to high immunity to electromagnetic induction effects, the optical waveguide become quickly exploited for challenging sensing applications [71], such as harsh environment with high voltage for example.

The optical fiber reacts to a variation of the quantity to be measured by modifying the guidance of the light wave propagating inside. This can result in a change of the intensity, the phase, the polarization state or the wavelength characteristics of the light. In this case, one refers to an intrinsic fiber-optic transduction which can be best used for structure integral measurements. In contrast, the optical fiber may be used to carry the information, acquired by an extrinsic transducer, which is usually installed at one end of the fiber, to the remote reading unit. The transducer can, for instance, alter the reflection of incoming light, modulate the light intensity coupled into the waveguide, or produce a radiation responding to the variations of the external quantity to be measured. In these cases, the extrinsic transduction happens only at the end of the fiber position of the external transducer and is often suited for local or point measurements [72].

## 3.3 Fiber-optic characteristics

Known as optical fibers, these guided wave dielectric feature a variation of the refractive index in the radial direction, exhibiting preferably cylindrical symmetry with respect to the fiber axis. The bulk of the optical fiber is most often fabricated from very pure silica ( $\text{SiO}_2$ ), which includes a core of doped silica featuring an enhanced refractive index. In this subsection the optical, mechanical, and coupled characteristics of such fibers are discussed.

### 3.3.1 Fiber-optic varieties

Fibers are usually classified as monomode and multimode types (see Tab.3.1). Multimode fibers which can be grading or step index, have larger cores (commonly around  $50 \mu\text{m}$  in diameter) and can transmit multiple transversal modes which have, in general, different

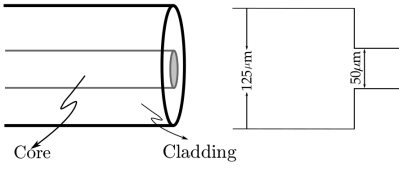
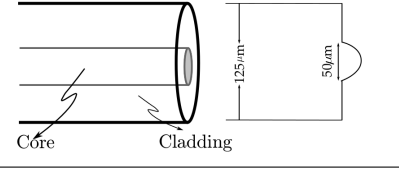
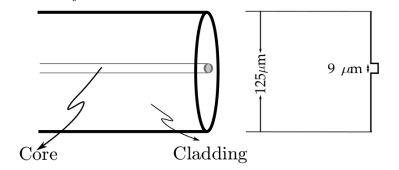
Type	Multimode step index
Multimode step index	<p>The refractive index of the core is constant</p> 
Multimode graded Index	<p>The refractive index of the core is changing</p> 
Monomode step index	<p>The refractive index of the core is constant and very small</p> 

Table 3.1: Types of optical fibers.

propagation speeds. This kind of fiber is best suited for broadband data transmission, but the modal dispersion makes these types of fibers unsuited for interferometric applications. In contrast, the monomode fiber has an index profile that allows only the fundamental transversal mode to propagate, while all higher-order modes are evanescent. Typical core sizes are between  $3\ \mu\text{m}$  and  $9\ \mu\text{m}$  [71]. Modal dispersion is a phenomenon not affecting monomode fibers and therefore these fibers allow interferometric measurements. Monomode fiber are affected by chromatic dispersion what is the result of a wavelength dependent index of refraction and is a material characteristic, also by waveguide dispersion and polarization mode dispersion. For typical silica fibers, the chromatic dispersion value is about zero at  $\lambda = 1300\ \text{nm}$  and around  $20\ \text{ps}/(\text{km} \cdot \text{nm})$  at  $\lambda = 1550\ \text{nm}$  [73]. So called dispersion fibers show a dispersion minimum at a wavelength  $\lambda\ 1300\ \text{nm}$ . Furthermore, the light in monomode fibers is transmitted as a  $\text{TEM}^2$  wave. In this work, interferometric transduction is studied and hence, monomode fibers of  $9/125/250\ \mu\text{m}$  core, cladding and mantling diameter are used for the experimental work.

The composition of the fiber consists of the silica glass ( $\text{SiO}_2$ ) and cross sectional regions of silica doped with small amounts of either  $\text{GeO}_2$  or  $\text{P}_2\text{O}_5$  for increasing the refractive index, or  $\text{B}_2\text{O}_3$  for reducing the index. Pure silica exhibits a refractive index  $n$  of 1.458.

### 3.4 Classification of fiber-optic transducers

In a Fuhr review article [73], around 60 different parameters which can be measured using fiber-optic are listed. Since light waves are characterized by amplitude (intensity), phase, frequency and polarization, any one or more of these parameters may undergo a change when the environment induces a change. External perturbation such as strain, pressure or

<sup>2</sup>TEM (Transversal ElectroMagnetic)

temperature variations that induce changes in the propagation velocity, the transmitted light wave intensity, the spectrum, or the polarization of the propagating light may be detected.

In general fiber-optic sensors can be categorized as:

- external or extrinsic: the fiber is only used to transfer the measurand information from a sensing region or the acquisition unit, as for example, a laser Doppler velocimetry or others generally expensive sensors,
- intrinsic: the measurand (strain, pressure, temperature, etc.) affects some optical property of the fiber resulting in modulation (intensity, phase, frequency or polarization) of the guided light wave.
- hybrid transducers, whereby light is transferred over the fiber to be converted to electricity to power a distant conventional sensor head.

Fiber-optic sensors can be also categorized by sensing location, the operating principle, and the sensing object (see Tab. 3.2). For extrinsic fiber-optic sensors, the fiber serves exclusively

Categories	Sensors	Examples of sensor	Application example
Mechanism location	Extrinsic	Chemical, Fabry–Perot	Pressure, Temperature, Liquid level
	intrinsic	FBG, Michelson, Sagnac	Rotation, Strain, Acceleration, Pressure
Operation principle (modulation and demodulation)	Intensity	Vibration, Micro- or Macro-bend	Amplitude
	phase	Sagnac, Michelson , Vibrometry	Strain, Pressure
	Frequencies	frequency-shifted interferometry	Dispersion, Fiber length, strain, refractive index
	Polarization	Force	Strain, Temperature
Sensing object	physical sensors	Piezoelectric, Photoelectric	Humidity, Temperature,
	chemical sensors	Viscosity	Chloride penetration, pH, Gas
	bio-medical sensors	Spectroscopy	Blood CO <sub>2</sub> and O <sub>2</sub> , pH

Table 3.2: Classification of fiber-optic sensor.

to carry light to and from an external device where the transduction of the environment variable into a light parameter takes place. In case of intrinsic transducers, the external perturbation directly modifies the properties of an optical fiber and modulates the light signal in the fiber accordingly. Since the intrinsic method enables distributed sensing it is preferably used for SHM [74, 75]. Elvin and Leung [46] demonstrated the feasibility of using an embedded intrinsic Mach–Zehnder interferometer sensor for delamination detection. Moreover, Fabry-Perot interferometer sensors have been proposed for monitoring of edge-induced and delamination in composites [47].

According to the operating principle (modulation and demodulation process), fiber-optic transducers can be also classified as intensity, phase, frequency (or wavelength), or polarization encoding device. Since detection of phase employs interferometric techniques, the related devices are also termed as interferometric transducers. Another categorisation of sensor is based on the sensing object or the sensed perturbation:

- PHYSICAL SENSORS to measure physical parameters like temperature, stress, etc.
- CHEMICAL SENSORS for pH measurement, gas analysis, spectroscopic studies, etc.
- BIO-MEDICAL SENSORS for bio-medical applications like measurement of blood flow, blood-glucose content etc.

A variety of commercial transducers based on different aforementioned light characteristics have been developed; from Fabry-Perot cavities to fiber Bragg gratings (FBGs). In addition, distributed sensors based on Raman and Brillouin scattering methods, are readily available along with pertinent interrogation instruments.

The typical fiber-optic transducer used for guided elastic wave detection are either interferometric sensors or fiber Bragg grating devices which will be discussed below. Regardless of their working principle and purposes, all above listed fiber-optic transducer have a common set of components being: light source, photodetector and the optical fiber to guide the light in between.

In this work, particular attention will be paid to interferometric fiber-optic transducers as well as the fiber Bragg grating which is more popular for SHM.

### 3.4.1 Fiber Bragg Grating

Fiber Bragg Gratings (FBGs) are the main workhorse within the family of fiber-optic transducers. For many specific transduction tasks, their performance may be considered as benchmark. Thus, their basic principle and application areas will be discussed first.

FBG-based transducers became more than any other particular sensor type a focus of contemporary research in structure monitoring [31, 76, 77, 78, 79] because of FBGs' high sensitivity to strain or temperature.

FBGs are of widespread use either in telecommunications, in instrumentation and for sensors of strain, temperature and pressure as well as many other measurands via appropriate transducing mechanisms. Due to the benefits of fiber optical transmission, FBGs have advantages over classical electrical strain gauges in many applications [76]. Although FBG principle is based on optical interference but the expression "interferometric transducer" is usually reserved for systems comprising multi-path interferometers.

The quasi intrinsic devices, FBGs are formed by spatially periodic changes in the effective refraction index of the core of a single mode fiber. Transmitting light, the reflected as well as the transmitted light portion exhibit grating induced spectral features around a wavelength determined by the Bragg grating periodicity as a consequence of phase matching between scattered partial waves. FBGs are short segments of modified single mode optical waveguides featuring, e.g., a periodic modulation of the core refractive index which can be considered as a one-dimensional grating. Light guided along the core of a fiber will be partially reflected by each grating plane. For certain wavelengths, constructive interference of these partial reflections occur and the fiber segment acts as a wavelength dependent dielectric mirror. Refraction index variations of the fiber core are formed e.g. by exposure of the doped fiber core to an intense optical interference pattern of light. An FBG acts as a filter because of

the existence of a stop band in the fiber transmission where most of the incident light in defined wavelength is reflected back. Because of the phase matching condition, the return signal intensity peaks where the optical propagation constant fits to the grating period. The sensing function of a FBG derives from the sensitivity of both the effective refractive index and the grating period to strain or thermal variation perturbations. The strain field, for example, affects the transmitting light of an FBG directly, through the expansion and compression of grating pitch size and through the strain-optic effect which can be defined as the strain-induced modification of the refractive index<sup>3</sup>. Particular wavelength of light that shifts in response to variations of strain and/or temperature. The reflections from each segment of alternating refractive index interfere at grating period  $\Lambda$  by a specific wavelength of light, called the Bragg wavelength, described as

$$\lambda_B = 2n_{\text{eff}}\Lambda, \quad (3.2)$$

where  $n_{\text{eff}}$  is the average mode index and  $\lambda_B$  is Bragg-wavelength, as shown in Fig. 3.2.

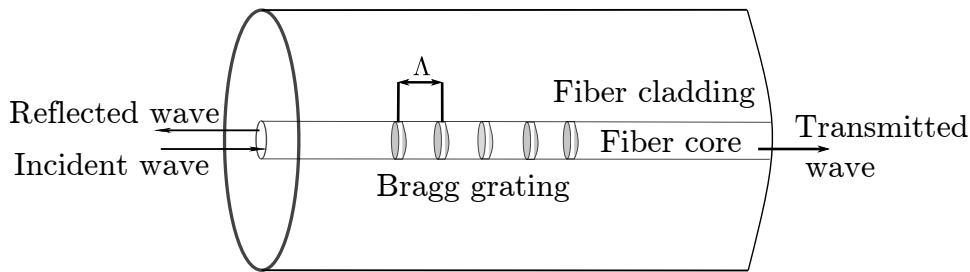


Figure 3.2: Fiber Bragg Grating structure.

It should be mentioned that an FBG sensing system based on interferometric detection has been developed for detection of a focused ultrasound field [78]. More recently, Lamb wave measurement for damage detection in composite materials using fiber Bragg grating transducer has been described by Tsudu [31] and Takeda [77].

FBGs can be used to sense elongations of the fiber axis where a strain resolution of  $2 \cdot 10^{-8}$  m/ $\mu\epsilon$  has been specified by the manufacturer “Technobis tft-fos” [80, 81], for example. Temperature effects also provoke immediate responses in the FBG characteristics due to thermal expansion. Another advantage, an optical waveguides can be equipped with multiple FBGs enabling distributed sensing. As the period  $\Lambda$  can be varied within a single fiber, the responses to environmental parameters at different locations of FBGs can be encoded to different spectral regions. Thus spatial multiplexing is converted into wavelength-multiplexing by such FBG multiples within a single sensing fiber. Although fiber Bragg grating sensors can be multiplexed in most physical architectures, the high sensitivity of FBGs is achieved only along the axis of the fiber, what can be a disadvantage, e.g., if the strain direction varies arbitrarily.

Regarding sensitive axial strain sensing applications, FBGs based sensors became more than any other particular sensor type a research topic of contemporary research [82]. Key feature of the FBG is the high feasible sensitivity in conjunction with a pronounced unidirectional characteristic.

Distributed sensing possibility and uniform integration of the measurand along the whole length of a long fiber segment is, however, often sought for applications like large structure

<sup>3</sup>Strain-optic effect or photoelastic effect will be detailed following subsection

monitoring. These goals can be met by intrinsic fiber-optic transducers only that enable new transducer features as well. Bending a segment in circular form, for example, enables a perfect omnidirectional transduction characteristic which is out of reach for FBGs.

### 3.5 Intrinsic mechanical and mechano-optical characteristics of optical waveguides

Composed essentially of silica, main physical fiber characteristics are determined by the properties of this vitreous material. Silica exhibits a mass density  $\rho$  of 2650 kg/m<sup>3</sup>, a Young's modulus of 73.1 GPa, Poisson Ratio of 0.17 and can withstand elongations up to 2 - 8% [71]. Monomode fibers have generally a diameter of 125  $\mu\text{m}$  with a core between 3 - 9  $\mu\text{m}$ , and a spring constant of 884 kN/m. Silica material as intrinsic object has an usually very low thermal expansion coefficient ( $0.55 \times 10^{-6}/^\circ\text{C}$  at 300 K) that helps to reduce the sensitivity to temperature variations in many applications.

Generally, structure monitoring is often associated with measurement of strain and displacement. The local deformations (expansion or compression) underneath an affixed fiber, generated by guided elastic waves in a plate, for example, lead to corresponding deformations of the optical fiber. While the fiber bending remains negligible, a significant variation of the fiber length, diameter and refractive index may occur. Changes in length, i.e. elongations, cause variations of the optical path length and thus change in phase in the course of transmission of sufficiently coherent light. The sensed deformation equals the spatial derivative of the local deflection projected onto the axis of the optical waveguide. The strain in the body underneath the fiber, intern, is governed by the mode characteristic of the exciting elastic waves. In case of predominantly longitudinal waves (S modes), the strain at the plate surface is (in first approximation) given by the spatial derivative of the particle displacement whereas for the antisymmetric wave (flexural A modes), the surface strain associated with the curvature of the plate. Intrinsic fiber optical transducers accumulate the local stretching of the fiber axis along the total length of the fiber segment attached to the plate. The intrinsic effect is manifested irrespective of straight, circular or coil fiber forming. As long as loading of the plate by the fiber remains negligible, enhancement of the transduction efficiency is possible with coiled fibers due to the extended interaction length.

The fiber-optic transducer of the interferometric type measures the phase change introduced in the sensing arm by the measurand with respect to an unchanged reference arm. The local light propagation delay  $d\tau$  changes according to the ratio defined by local change in length of a fiber segment  $L$  over the local change in the speed of light,  $c_0/n_{\text{eff}}(\lambda_0)$

$$d\tau = d(n_{\text{eff}}(\lambda_0)L/c_0), \quad (3.3)$$

where  $c_0$  denotes the vacuum speed of light and  $\lambda_0$  the free space wavelength of the transmitted light.

In case of negligible for- and backward light propagation time with respect to the temporal variations of fiber, the change in the total running time is given by the path integral of  $d\tau$ . For small relative deformations and rigid adhesion, the square of the local length change of a fiber segment,  $(dl)^2$  is given by

$$(dl)^2 = \vec{e} \underline{C} \vec{e}, \quad (3.4)$$

wherein said unit vector  $\vec{e}$  points in the fiber's axial direction and  $\underline{C}$  denotes the Cauchy-Greens deformation tensor [83].

Since the local variation depends on the deformation at the structure's surface where the optical fiber is affixed, the component of the deformation parallel to the surface of the plate and perpendicular to the cross-section plane of the optical fiber create the largest sensitivity. The transduction efficiency scales with the cosine of the angle between the local fiber axis and the direction of local strain. Strains perpendicular to the surface are rather ineffective, since they are oriented perpendicular to the fiber axis.

Supply a fiber with a light source, the phase  $\phi$  of a light wave guided by a fiber of short geometrical length  $L$  is given by [84]

$$\phi = n_{\text{eff}} k_0 L, \quad (3.5)$$

where  $k_0 = 2\pi/\lambda_0$  is the free space circular wavenumber of the monochromatic light. The optical path length is given as the product of an effective index of refraction and fiber length  $n_{\text{eff}} \cdot L$ . The effective refractive index  $n_{\text{eff}}$  considers the refractive index of the fiber medium  $n_m$  as well as the influence of the boundary conditions imposed by the waveguide cross section design. Changes in the refractive index  $\Delta n_{\text{eff}}$ , as well as changes in the fiber geometrical length,  $\Delta L$ , will directly influence the optical path length.

If a short fiber segment is subjected to an uniform strain  $\varepsilon = \Delta L/L$ , the phase difference per unit fiber length changes proportional to that strain. The applied strain modifies not only the fiber geometry but also the refractive index of the fiber material. In case of constant strain, the light phase response is proportional to the length  $L$

$$\Delta\phi = \Delta(n_{\text{eff}} k_0 L) = L \cdot k_0 \cdot \Delta(n_{\text{eff}}) + k_0 \cdot n_{\text{eff}} \cdot \Delta L = L \cdot k_0 (\Delta n_{\text{eff}} + n_{\text{eff}} \cdot \varepsilon). \quad (3.6)$$

The first term  $\Delta\phi_n = L \cdot k_0 \cdot \Delta n_{\text{eff}} = L \cdot k_0 (\Delta n_m + \Delta n_w)$  contains the change in the index of refraction  $\Delta n_m$  by the strain-optics effect or photoelastic effect as well as the changes of the propagation constant of the waveguide mode caused by the reduction in diameter of the fiber under axial stress, formally expressed as  $\Delta n_w$ . The second term  $k_0 \cdot n_{\text{eff}} \cdot \varepsilon \cdot L$  represents the optical phase difference due the axial stretching of the fiber.

The complete differential expression describing the effect of uniform strain of cylindrical fiber is

$$\frac{\partial\phi}{\partial\varepsilon} = k_0 n_{\text{eff}} L + L k_0 \frac{\partial n_{\text{eff}}}{\partial n_m} \frac{\partial n_m}{\partial\varepsilon} + \underbrace{L k_0 \frac{\partial n_{\text{eff}}}{\partial D} \frac{\partial D}{\partial\varepsilon}}_{\approx 0} \quad (3.7)$$

where  $D$  is the fiber core diameter. The third term of Eq. 3.7 has been shown in [85, 86] to be negligible. To simplify the further analysis, these lateral deformations of fibers were not considered in the following discussion, and the transmitted light is assumed to remain at the fundamental mode when the fiber length is stretched and compressed. This is essentially the simplification made by Butter and Hocker in their early paper [84] on the subject.

Fortunately, the two remaining effects can both be related to the axial strain. The first contribution to the phase shift  $\phi$  occurs due to axial strain  $\varepsilon$  in a straightforward manner whereas  $n_m$  is determined by the radial strain that is coupled to the axial strain according to  $\varepsilon_r = -\nu \cdot \varepsilon$  in case of pure fiber stretching, where  $\nu$  is the Poisson number of the fiber material.  $\varepsilon_r$  is of relevance for  $n_m$  since the propagating light wave can be decomposed into transverse polarized optical field components [87].

Globally, the changes in the refraction index of any dielectric subjected to a strain is given by the strain-optic law [88] by

$$\Delta \left( \frac{1}{n_m^2} \right)_i = P_{ij} S_j, \quad (3.8)$$

where infinitesimal strain in the  $L$ -direction causes a strain vector  $S_j = [\varepsilon \quad -\nu\varepsilon \quad -\nu\varepsilon]^T$ ,  $P_{ij}$  are the components of the strain-optic or Pockels tensor.

According to Eq. 3.8, in the case of normal circular fiber, the variation of the refractive index  $\Delta n_m$  in case of strain  $\varepsilon$  in axial direction can be expressed by [86]

$$\Delta n_m = -\frac{n_m^3}{2}\varepsilon [(1-\nu)P_{12} - \nu P_{11}]. \quad (3.9)$$

For fused silica the material parameters are  $\nu = 0.17$ ,  $n_m = 1.456$ , and at  $\lambda_0 = 1310$  nm  $P_{11} = +0.121$ , and  $P_{12} = +0.270$  [86].

Equation 3.9 yields negative values for  $\Delta n_m$  leading to a negative contribution to the phase change in case of positive strain  $\varepsilon$ . Within the frame of the chosen approximation, the phase change of a fiber segment of length  $L$  exposed to uniform axial strain  $\varepsilon$  can be now expressed as

$$\Delta\phi = k_0 n_{\text{eff}} L \varepsilon \left\{ 1 - \frac{n_{\text{eff}}^2}{2} [P_{12} - \nu(P_{11} + P_{12})] \right\}. \quad (3.10)$$

For nonuniform axial strain  $\varepsilon(x)$  immediately follows

$$\Delta\phi = k_0 n_{\text{eff}} \left\{ 1 - \frac{n_{\text{eff}}^2}{2} [P_{12} - \nu(P_{11} + P_{12})] \right\} \int_L \varepsilon(x) dx. \quad (3.11)$$

Interferometric transduction is based on the detection of changes in the phase of light emerging the attached monomode fiber with respect to the fixed reference arm. If the strain along the attached fiber segment varies with position, the guided wave phase integrates the local strain effect caused by the elastic wave. On this basis, the total change of phase  $\Delta\phi(\varepsilon)$  is a combination of integral average value of the local changes in length and integral average of the changes in refractive index. Roughly speaking, the index change given by Eq. 3.9 compensates about 30% of the propagation delay caused by a purely geometric stretch of the fiber length [85]. However, this simple dependence on  $\varepsilon$  conceals a rich variety of sensing peculiarities. In this work, first of all, it has to be assured that the repercussion of the attached silica fiber on the exciting elastic wave is negligible, at least to a first order approximation. Also, the local angle  $\theta$  between fiber axis and strain orientation at the plate surface may vary especially for curved fiber or wavefronts.

### 3.6 Interferometric fiber sensors

To achieve sufficiently high sensitivity to strain of arbitrary direction, a fiber-optic transducer must be of the interferometric type and acquire omnidirectional sensitivity. However, it should note here that interferometric transduction represent a large class of extremely sensitive devices, changing the phase of a light wave propagating in a single mode optical fiber is the measurement characteristic [89, 90]. Over the years, many different interferometer systems architectures have been proposed and investigated for transduction purposes. The most important ones can be categorized into four fundamental configurations: Mach-Zehnder, Michelson, Sagnac, and Fabry-Perot interferometer. FBG are not classed in this categorie. Initially applied to the characterization of short lengths of optical fibers [89], the technique has also been used for the characterization of wavelength selective elements such as a grating pair [91] and, more recently, short lengths of photonic bandgap fibers [92]. Indeed, the interferometric principle consists of a superposition of two light waves, coming from one coherent

source, which were divided by a suitable apparatus and sent along different ways toward the target. The light intensity in the region of superposition can be found to vary from point to point between maxima which exceed the sum of the waves intensity and the minima which may be zero. Hence, interference is generated by summing the two coherent light waves with different optical phases. Any phase difference is created by path length differences which can be of pure geometric nature or due to differences of the refractive index. The basis of the fiber-optic interferometric sensor is the measurement of a physical parameter through the phase modulation what induces in the guided optical wave in a sensing element. Thus, the sensing element will be the fiber itself, one talks in above subsection of intrinsic sensor.

In all cases, the length change in one of the interferometer arms induces a change in the relative phase. At the detector, both partial waves are gathered and therefore the intensity at the detector indicate a sinusoidal intensity variation with respect to the phase difference as shown below.

In case of strain measurement, the optical phase shifts in the core of the fiber where strain states are inferred. Considering the optical circuit diagram of a common form of optical fiber interferometer (e.g. Mach-Zehner) in Fig. 3.3, the light propagates in the  $x_1$ -direction, which can be characterized by the accompanying electrical field  $E = E_0 \sin(kn_1 x_1 + \omega_{opt}t)$ , where  $E_0$  is source signal amplitude,  $k$  the wavenumber, and  $\omega_{opt}$  the angular frequency of the optical wave. The light wave is put into the entrance of the interferometer, and split into bundles with a directional coupler  $2 \times 2$  (reference and sensing fiber). If the splitter splits the entering wave  $E_0$  symmetrically, both partial waves do not have any initial phase shift difference  $\phi$ . After crossing respectively the total lengths  $n_1L_1$  and  $n_2L_2$ , the signals through the paths  $P_1$  and  $P_2$  can be expressed as

$$E_1 = E_{01} \sin(kn_1L_1 + \omega_{opt}t) \quad \text{and} \quad E_2 = E_{02} \sin(kn_2L_2 + \omega_{opt}t). \quad (3.12)$$

By installing a photodetector at exit of the system, the light intensity  $I$ , which is connected to the field strength is

$$\begin{aligned} I &= (E_1 + E_2)^2 = E_{01}^2 \sin^2(kn_1L_1 + \omega_{opt}t) + E_{01}E_{02} \cos(k(n_1L_1 - n_2L_2)) \\ &\quad + E_{01}E_{02} \cos(k(n_1L_1 + n_2L_2) + 2\omega_{opt}t) + E_{02}^2 \sin^2(kn_2L_2 + \omega_{opt}t). \end{aligned} \quad (3.13)$$

Using basic trigonometric identities, one obtains

$$\begin{aligned} I &= \frac{E_{01}^2}{2}(1 - \cos(2(kn_1L_1 + \omega_{opt}t))) + E_{01}E_{02} \cos(k(n_1L_1 - n_2L_2)) \\ &\quad + E_{01}E_{02} \cos(k(n_1L_1 + n_2L_2) + 2\omega_{opt}t) + \frac{E_{02}^2}{2}(1 - \cos(2(kn_2L_2 + \omega_{opt}t))). \end{aligned} \quad (3.14)$$

Since practical photodetectors cannot follow intensity variations with twice the light angular frequency  $2\omega_{opt}$ , these terms may be dropped for further considerations. The intensity related output signal of the detector  $I_{PD}$  would therefore be

$$I_{PD} \propto \frac{1}{2}E_{01}^2 + \frac{1}{2}E_{02}^2 + E_{01}E_{02} \cos(k(n_1L_1 - n_2L_2)). \quad (3.15)$$

Obviously  $I_{PD}$  is maximum if the cosine equals  $+1$  and is minimum when the cosine equals  $-1$ . The measured light intensity variation is therefore only dependent on the optical path difference. The variation  $\Delta\phi_n = k(n_1L_1 - n_2L_2)$  is the optical path length difference between the both branches of the Mach-Zehnder interferometer.

The phase of the light emerging from a fiber section is modulated by the environmental variable to be detected. Depending on the phase difference, interference varies from destructive to constructive, thereby producing intensity modulation at the detector.

### 3.6.1 Waveguide based interferometer types

The most commonly used interferometric fiber-optic sensors exploits the Michelson configuration, which is suitable for measuring acoustic waves, electric and magnetic fields, temperature and strain. The Mach–Zehnder interferometer type is capable of measuring any of the above parameters including current. The Sagnac type offers rotation and wavelength measurement capability, and acceleration sensing. The Fabry–Perot system depends on an external optical resonator in addition to fiber-optic couplings to light source and detector [93].

**Mach-Zehnder interferometers** (see Fig. 3.3) based on optical waveguides are predestined for sensing applications. Developed by the physicists Ludwig Mach and Ludwig Zehnder, the incoming light is split into two paths at coupler. In case of sensor applications one (or both) paths are equipped with components that cause minute changes of the optical path length in response to an external influence. Hence, the separated optical fields acquire some phase difference relative to each other. Afterwards, they are recombined with another coupler allowing interference at the surface of a photodetector. Depending on the actual phase difference, the interference at the detector varies from destructive to constructive, thereby producing an intensity modulation at the detector [94, 95]. For defined transduction by the sensing part, the reference part must be main-

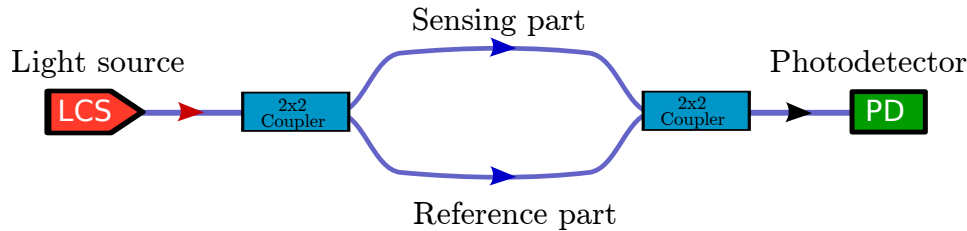


Figure 3.3: Mach-Zehnder interferometer scheme based on fiber-optic.

tained under stable conditions. A disadvantage of this interferometer type is that any initial path imbalance converts the phase noise of the light source output into intensity noise and hence deteriorates the performance of the sensor system.

**Michelson interferometer** in Fig. 3.4 is similar to the Mach–Zehnder. Invented by Albert Abraham Michelson, the major difference is that there is only a single coupler acting as light wave splitter as well as wave recombination unit at the entrance of the interferometer legs. Furthermore, mirrors have been put at the output of the interferometer legs. One part of the light propagates to the reference mirror on which it is reflected. The other part of the light is reflected at the measuring object. Both reflected light waves are guided to the detector. The displacement of a single moving mirror (object) from a reference position can be calculated with a high degree of precision. The Michelson interferometer uses highly reflective terminations at the ends of the interferometer arms and detects intrinsic variations of the optical waveguide properties. The Michelson fiber-optic sensor presents high sensitivity to stress-strain along the entire length of the optical fibers [96].

**Sagnac interferometer** (named after the French physicist Georges Sagnac) is based on an optical fiber coil and can act as rotation sensor or gyroscope [97] and was used to

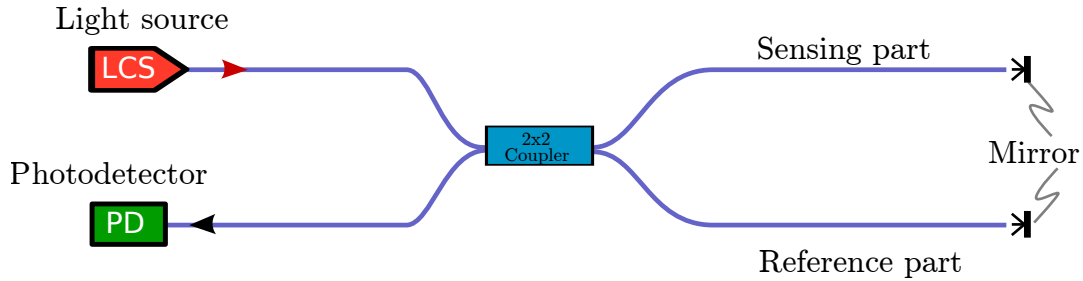


Figure 3.4: Schematic of Michelson Interferometer.

measure the rotational speed of the earth. It is also be employed to measure time-varying effects such as acoustics, vibration, and strain [98, 99]. In this interferometer configuration, light from the source is split into a clockwise beam (CW beam) and a counterclockwise beam (CCW beam). The CW beam travels through the polarization controller loop first and then through the fiber coil, while the CCW beam travels through the fiber coil and then through the controller loop. Because of the non-symmetrical positioning of the fiber coil, the phase difference induced by a time varying measurand in the fiber coil is translated into a phase difference between the two guided waves as they meet again at the coupler. This phase difference in turn is converted into intensity modulation when the waves are combined by the coupler. Sagnac interferometer can be used as a distributed sensor capable of measuring the location of a disturbance. One of its rare uses of the Sagnac interferometer in vibration

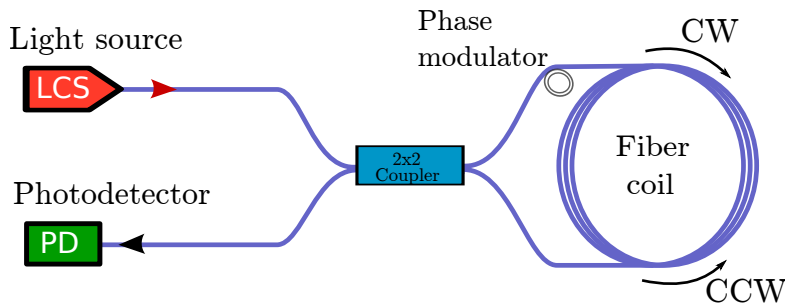


Figure 3.5: Fiber Sagnac interferometer sensor system.

monitoring was reported by Harvey et al. [100, 101].

**Fabry–Perot interferometers** may sense temperature, strain, and ultrasonic pressure in different structures, e.g., composite materials [102, 103]. This interferometer is built of two mirrors of reflectance  $R_1$  and  $R_2$  separated by a cavity of length  $L$  along the optical axis of the fiber, as shown in Fig. 3.6. The reflectance or/and transmittance of the resonator can be monitored. Fabry–Perot interferometer can be made extremely sensitive to perturbations that affect the optical path length ( $n_{eff} \cdot L$ ) between the two mirrors. A strain induced change in the optical path length  $n_{eff} \cdot L$  between the two mirrors of the Fabry-Perot sensor leads to a corresponding shift in the cavity mode frequencies and related intensity variations of transmitted and reflected light waves.

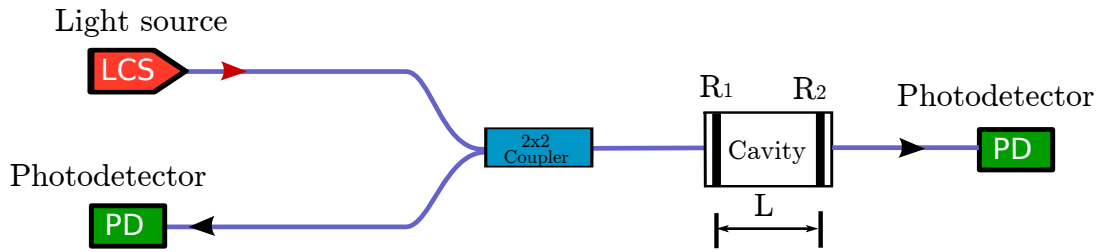


Figure 3.6: Fabry-Perot Interferometer system.

### 3.6.2 The employed double Michelson interferometer

In this work, an extension of the basic fiber-optic Michelson interferometer transducer configuration depicted in Fig. 3.4 is used. The double Michelson interferometer has the advantage of giving two simultaneous interferences which differ by a constant phase offset of  $2\pi/3$  with respect to the interference patterns of the optical fields. This avoids a main problem of the simple Michelson interferometer where the transduction of the path difference exhibits two broad conversion minima around constructive and destructive interference. The  $3 \times 3$  coupler produces two phase shifted interferograms simultaneously where at least one of them shows strong variation with path length changes. A stable output with a large signal dynamic range and a minimum detectable phase shift in the micro range has been achieved [50].

**Fiber-optic double interferometer setup:** A system overview of a practical implementation of the double interferometer transduction method is illustrated in Fig. 3.7. The arrangement is built around a  $3 \times 3$  fiber-optic directional coupler made of single mode fiber. Light emitting from a coherent source, is transmitted by the coupler towards to two optional fiber-optic coils serving as sensing and reference arms. These arms have perfectly reflecting end faces while the third output fiber features negligible reflection since its end face is cut with a slope of 8 rad/mm (low reflective). The light hitting photodiodes PD1 and PD2, comprises the reflected wave of the same fiber and, additionally, corresponding components received via fiber-to-fiber transmittance between neighboring fibers in the coupler.

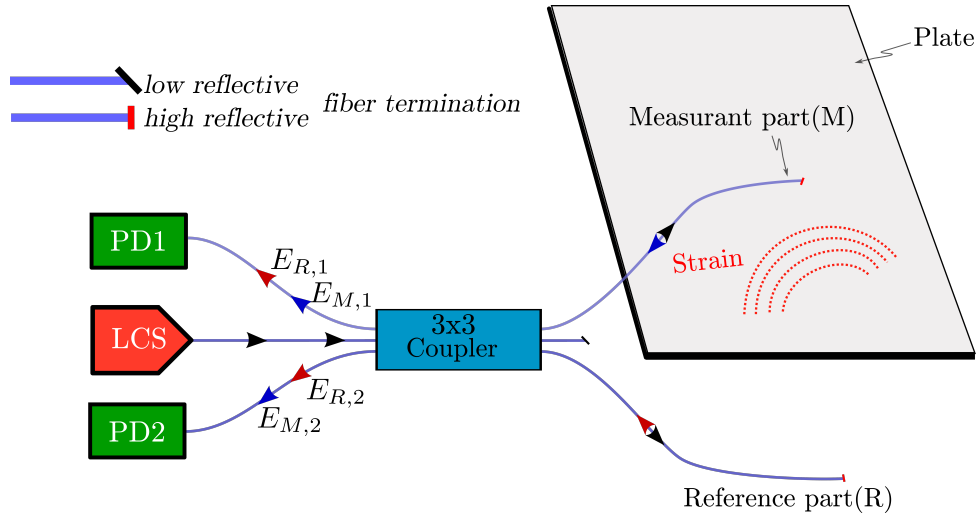


Figure 3.7: Essential components of the fiber-optic transduction setup. PD1, PD2 - photodiodes, LCS - low coherence source, 8 rad/mm cut slope, the sensing coil is exposed to an external perturbation as indicated.

Assuming uniform stretch along the attached fiber, the interferometer sensitivity increases with interacting fiber length. For homogeneous strain the interaction length can be increased by meandered [86] or coiled fiber segments. If the fiber bending radius has no detrimental effect on the efficiency of the optical wave guide and the loading of the sample remains negligible, the number of turns of the coil may be increased taking advantage of the increased transduction efficiency.

**Fiber-optic double interferometer function:** A deformation of the plate leads to a change of the time needed for forward and backward propagation of guided light in the measurement coil. Then, both photodetector signals vary according to the changing phase  $\phi$  retardation, which in turn, is coupled to the plate deformation. This enables a convenient computation of the phase difference between measurement and reference arms [104].

The intensity of the interfering light can be processed conveniently after transforming it into electrical signals.

As the Lamb wave causes a time variable path length difference only in the attached fiber, a respective phase shift  $\phi = \phi(t)$  between the reflected light waves of measurement and reference coil branches occur at the  $3 \times 3$  fiber-optic directional coupler. The  $3 \times 3$  coupler distributes all reflected waves and introduces an further phase shift of  $2\pi/3$  if a partial wave is transferred between two fibers [105].

The intensities of the interference signals were converted with photodiodes into photocurrents ( $i_{D1}$  and  $i_{D2}$ ). For the moment, ideal conversion characteristics are assumed. In fact, a difference in intensity  $I_1 \neq I_2$  will be observed due to non-perfect symmetry of the elements. That means, there are four different optical field amplitudes  $E_{M,1}$ ,  $E_{M,2}$ ,  $E_{R,1}$ ,  $E_{R,2}$  arriving at the detectors and the evaluation of the interference signals must take this into account. Here the subscripts M and R stand for the measurement and reference arm, while 1 and 2 indicate the two detector arms.

In the simplest case (the same length of the fiber coils at rest, perfect coupler, perfect

coherence), the intensities  $I_1, I_2$  on the detectors are

$$I_1 = [E_{M,1} \cdot e^{j\omega t} + E_{R,1} \cdot e^{j(\omega t + \phi + 2\pi/3)}] \cdot [E_{M,1} \cdot e^{-j\omega t} + E_{R,1} \cdot e^{-j(\omega t + \phi + 2\pi/3)}], \quad (3.16)$$

$$I_2 = (E_{M,2} \cdot e^{j(\omega t + 2\pi/3)} + E_{R,2} \cdot e^{j(\omega t + \phi)}) \cdot [E_{M,2} \cdot e^{-j(\omega t + 2\pi/3)} + E_{R,2} \cdot e^{-j(\omega t + \phi)}], \quad (3.17)$$

$$i_{D1} \propto E_{M,1}^2 + E_{R,1}^2 + 2E_{M,1} \cdot E_{R,1} \cos(\phi - 2\pi/3), \quad (3.18)$$

$$i_{D2} \propto E_{M,2}^2 + E_{R,2}^2 + 2E_{M,2} \cdot E_{R,2} \cos(\phi + 2\pi/3), \quad (3.19)$$

where  $\omega = 2\pi f$  denotes the circular frequency of the optical waves. Equations 3.18 and 3.19 reveal that the derivatives of the detector currents with respect to  $\phi$  have no coinciding extrema. The zeroes of  $\partial I_D / \partial \phi$ , correspond to extrema of the interferometric transduction which are a major drawback of single interferometers. When surface strain induced by guided waves deform temporarily one leg of the interferometer setup, the relative phase becomes time dependent, i.e.,  $\phi = \phi(t)$ .

The conversion of the photocurrents  $i_{D1}, i_{D2}$  into voltage signals is performed by transimpedance amplifiers.

Accordingly, these voltages are each composed of a constant and an interference-related component which is now assumed to exhibit time dependence determined by the temporal path length variation in the measurement arm

$$V_1(t) = V_{1,0} + V_{1,1} \cdot \cos(\phi(t) - 2\pi/3), \quad (3.20)$$

$$V_2(t) = V_{2,0} + V_{2,1} \cdot \cos(\phi(t) + 2\pi/3). \quad (3.21)$$

The availability of two voltage signals  $V_1, V_2$  allows the determination of the sought phase angle  $\phi(t)$  [104], if the static values  $(V_{1,0}, V_{2,0})$  and the maximal variations due to interference  $(V_{1,1}, V_{2,2})$  are known. Plotting  $V_1(t), V_2(t)$  against each other in a Cartesian coordinate system, the instantaneous value moves along an elliptical arc if  $\phi$  changes. In case of low coherence light, the Lissajous figure of  $V_1$  vs  $V_2$  forms an elliptic spiral which should be taken into account in case of large phase shifts. The center of the ellipse is given by  $V_{1,0}, V_{2,0}$ , whereas the side lengths of the circumscribed rectangle parallel to the axes are  $2 \cdot V_{1,1}, 2 \cdot V_{2,1}$ . By conversion of the equations 3.20, 3.21, one obtains

$$\tan(\phi(t)) = \frac{(V_2(t) - V_{2,0}) \cdot V_{1,1} - (V_1(t) - V_{1,0}) \cdot V_{2,1}}{(V_2(t) - V_{2,0}) \cdot V_{1,1} + (V_1(t) - V_{1,0}) \cdot V_{2,1}} \cdot \frac{\cos(2\pi/3)}{\sin(2\pi/3)}. \quad (3.22)$$

From 3.22, the argument  $\phi(t)$  the total length change of the coiled fiber,  $\int \varepsilon dl$ , can be computed based on 3.10

$$\int_L \varepsilon(t) dl = \frac{\phi(t)}{k_0 n_{\text{eff}} (1 - \frac{n_{\text{eff}}^2}{2} [P_{12} - \nu(P_{11} + P_{12})])}, \quad (3.23)$$

where the integral path extends along the complete attached fiber (coil) featuring a total fiber length  $L$ .

It should be noted, that this simple derivation presumes that the temporal variation of  $\varepsilon(t)$  is negligible within the turnaround period of the light in the interferometer arms. The fiber length of a typical multiple-turn coil is of the order of 1 m. Hence, for a propagation velocity of roughly  $2 \cdot 10^8$  m/s the forward and backward propagation delay is about 10 ns. This limits the allowed frequency range for strain variations to  $\ll 100$  MHz for interferometer operation, while 1 MHz is typical for Lamb wave applications [106].

### 3.7 Transduction of plane waves by a circular fiber segment

Guided waves are typically produced by piezoelectric ceramic devices glued on the plate. Depending of the device shape and the distance between the source and sensing object, various forms of the guided wavefront are observed. In this section, some fundamental consequences of the guided wave detection with circular fiber-optic transducers are discussed. To enable a straightforward treatment, one considers only plane Lamb waves. Such plane Lamb waves may be produced by pulses of uniform displacement or stress applied to a straight plate edge. Fortunately, at a large distance from an actuator the circular excited wavefronts can be regarded as nearly flat. Hence, similar effects are observed for circular fiber transducers in response to sufficiently separated piezoelectric actuators.

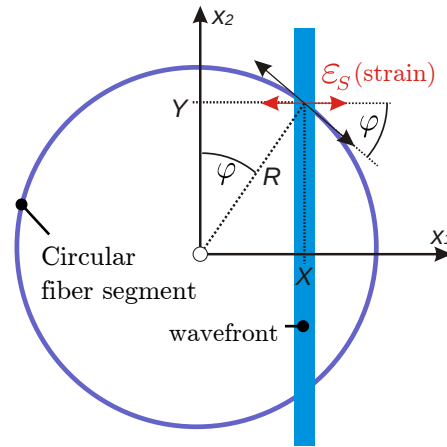


Figure 3.8: Derivation of the strain conversion by circular fibers for plane compressional waves.

Figure 3.8 shows a snapshot of the interaction of a plane wavefront (colored bar) with a circularly bent fiber. The pure compressional wave is assumed to propagate along the  $x_1$ -direction and therefore the strain  $\varepsilon_S$  at the plate surface is also parallel to  $x_1$ . The wavefront under consideration crosses the circuit at a distance  $X < R$  from its center. Then the cosine of the crossing angle  $\varphi_C$  between surface strain orientation and the tangent to the circuit is given by

$$\cos(\varphi_C) = Y/R = \sqrt{1 - X^2/R^2}.$$

The axial strain of the fiber at the cross over location is given by  $\varepsilon_S \cdot \cos(\varphi(X))$ . Simply spoken,  $\cos(\varphi(x_1))$  is the spatial sensitivity characteristic of the circular fiber in case of plane compressional waves. To obtain the total length change of the circular fiber at a specified moment  $t_0$ , one has to integrate the effect along the full circular path, which is equivalent to

$$2 \cdot \int_{-R}^R \varepsilon_S(x_1, t_0) \cdot \cos(\varphi(x_1)) dx_1. \quad (3.24)$$

To compute the time dependent response to a compressional wave, the propagation of the wavefront must be considered. This is most easily done for stable wave packet shape functions i.e., non-dispersive waves. Then a time shift  $d\tau$  corresponds to a wavefront propagation distance  $dx_1 = v_{PH} \cdot d\tau$ . In other words, the strain pattern is shifted by  $dx_1$  with respect

to the circular integration path, or, the other way round, the sensitivity function is shifted against the snapshot of the wave strain pulse. The complete response of the circular fiber to a compact wave packet can be computed from a convolution integral of the strain shape function and the fiber sensitivity curve in the space domain. If the strain pulse has a duration of  $\tau_P$ , its spatial extension measures  $l = \tau_P \cdot v_{PH}$  and the total convolution response requires a shift distance  $\geq (l + 2R)$ . Hence

$$f(x) = \int_{x_0-R}^{x_0+l+R} s(\xi) w(x-\xi) d\xi, \quad (3.25)$$

where  $s(\xi)$  denotes the strain pulse shape in the space domain, starting at  $\xi = x_0$ , and

$$w(x) = 2\sqrt{1 - x^2/R^2}, \quad x^2 < R^2. \quad (3.26)$$

is the sensitivity function of the circular fiber, where the factor of two results from the two intersections of the wavefront and the circle.

Alternative window functions are

$$w(x) = 2d \cdot \frac{\sqrt{1 - x^2/R^2}}{\sqrt{d^2 + R^2 - 2dx}}, \quad x^2 < R^2, \quad (3.27)$$

and

$$w(x) = \frac{(2xd - R^2)}{R\sqrt{d^2 + R^2 - 2dx}}, \quad x^2 < R^2, \quad (3.28)$$

for the radial and tangential strain of circular crested waves emerging from a center at distance  $d$  from the center of the fiber circle, respectively.

It should be noted that the tangential and radial strain decrease with  $R^{-3/2}$  and  $R^{-1/2}$ , respectively, with  $R$  the distance from the center of the circular wave. For a single straight fiber of length  $2R$  oriented in propagation direction of a plane compressional wave one obtains.

$$w(x) = 1, \quad x^2 < R^2.$$

Figure 3.9 depicts the window functions for these four cases for a distance  $d = 2R$ . The peak of the circular window functions is twice that of the single straight fiber since the circle crosses the wavefront twice.

It is obvious that the convolution integral of Eq. 3.25 extends the response  $f(x)$  by  $2R$  compared to the strain pulse  $s(x)$ . In the time domain, the argument of the response has to be replaced, i.e., the temporal response reads  $g(t) = f(x/v_{PH})$  and it is prolonged by  $2R/v_{PH}$  compared to the duration of the strain pulse (see Fig. 4.14).

The plate deformation can be deduced directly from Eq. 3.23 only for wavelengths of the elastic perturbation much larger than the fiber coil diameter.

### 3.8 Robust fiber-optic transducer system

A serious disadvantage of most fiber-optic transducers is their mechanical fragility, as it complicates the handling and requires special attention in harsh environments. Furthermore, an interferometric transduction that utilizes optical waveguides is highly sensitive to spurious variations of the environment like nonuniform temperature changes along the fiber-optic

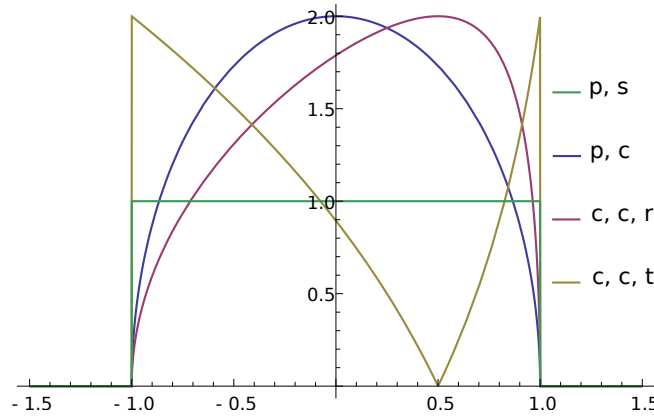


Figure 3.9: Window functions for wavefront conversion. The considered cases cover: plane wave conversion by a straight piece of fiber of length  $2R$  along the propagation direction as well as the conversion by a circular bent fiber of radius  $R$  for plane and circular crested wavefronts where a center to center distance  $d = 2R$  was chosen. The first character of the legend denotes the wavefront type (plane, circular) the second character the fiber geometry (straight, circular) and the last item indicates the strain components of circular crested waves (radial, tangential).

setup. Such influences may cause high signal drifts and, in case of limited coherence length, signal fading as well. To largely eliminate this disadvantages, a novel, mechanically robust arrangement of the fiber-optics has been developed. The new transducer design employs a sandwiched structure in L-form including a thin plate carrier, which is attached to the body of interest with one surface and bears the coiled measurement fiber on the opposite side. The support material must be resistant to be buckled during handling and at the same time compliant to the elastic deformations accompanying Lamb waves. The reference fiber coil is attached to another L-shaped carrier in mirror-imaged configuration.

The measurement and reference arms of the fiber-optic interferometer will be attached to their respective carriers with a rigid adhesive as shown in in Fig. 3.10. Afterward the arrangement is folded, keeping sufficient distance between the carriers to accommodate the fiber-optic coupler in between. Finally, the gap between the carriers is filled with soft silicone elastomer. The resulting structure comprises concentric positioned coils of optical measurement fiber carried by support A and reference fiber glued on the support B.

The folded configuration protects the enclosed fiber segments from mechanical damage. Furthermore, the carriers together with the soft silicone rubber greatly reduce spurious temperature differences between measurement and reference arm.

Two 5 turn spiral fiber coils of 25 mm in diameter were used for the sensing and reference coil implementation. The carrier of the measurement coil is affixed to the plate under investigation. The fiber tip of the middle output arm of the  $3 \times 3$  coupler is polished at  $8^\circ$  angle in order to suppress the back-reflection from this arm.

It is obvious that the stiffness of the fiber coil carriers as well as the mechanical coupling of measurement and reference coil by the elastomer is detrimental for the fiber-optic detection of guided waves in the attached plate. The question to be answered by finite element analyses and experiments is whether or not the Lamb wave sensitivity of the robust transducer construction is significantly reduced compared to the conventional setup.

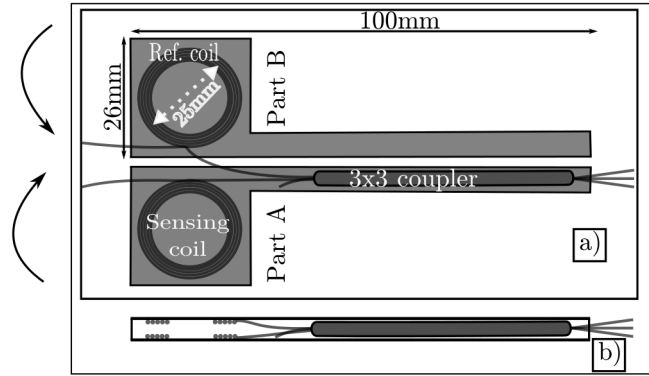


Figure 3.10: Design of the robust sensor system, reference and measurement fiber coil are glued on Part A and B respectively. a) Open structure and b) the finished transducer with wave attenuator between support A and B.

### 3.9 Summary

Mechanical deformations of an optical fiber affects the light propagation as a consequence of the changes in the fiber core and the cladding geometry and changes in the refractive index caused by the mechanical strain. When a single-mode optical fiber is deformed, the speed of light in the optical fiber is changed. This property of the fiber is used for sensing application. A common feature of all fiber-optic transducers is the mechanical vulnerability of the fibers. Numerous concepts are available while only a few have been discussed in this chapter.

Intrinsic interferometric fiber-optic transducers enable distributed acquisition of an interacting quantity. As these transducers usually integrate the interfering effect, their transduction may be improved by simply extending the fiber length. The described double Michelson interferometer system presents significant advantages over single interferometers.

Length changes in the optical fibers result in variations in the phase of the emerging light. A linear relation between changes of the geometrical length of the fiber path and the guided light propagation constant is established. The interferometric detection of changes of the fiber length with two photodetectors and a reference fiber employing a  $3 \times 3$  fiber coupler was discussed. An analytical result describing the distortions introduced by the transduction of plane compressional guided waves by circular bent optical fibers and plane guided waves is established.

The main aim of this work is the development of a *robust* and *reusable* interferometric detector that can achieve an *omnidirectional* sensitivity characteristic to elastic deformations in plates. The fragile monomode fiber of the measurement and reference arm are mechanically protected by appropriate carrier sheets. Possible detrimental effects of the carriers on the transducer sensitivity will be investigated by FEA described in subsequent chapters leading to an efficient design. Measurements performed on a practical implementation of such a device proved the sensibility of designed transducer.

# Chapter 4

## Modeling

Theoretical models of physical interrelations typically rely on rough abstractions of the practical implementations used to observe related phenomena. Finite element analysis (FEA) are a beneficial tool to bridge the gap between theory and experiment. Modern FEM suites enable the computation of highly dynamic mechanical deformations of bodies carrying firmly attached fiber segments. In the course of this thesis, numerous FE analysis were applied to examine various arrangements for Lamb wave generation, its propagation and detection.

First, a prototype model of fiber-optic strain transduction is devised that enables a quantitative comparison of FEM and interferometric measurement results. An encouraging match between simulation and measurement has been found which is briefly discussed. Having confirmed the basic function of the fiber-optic transducer, further models were devised to study secondary effects like the loading of the plate by the fiber-optic transducer or the signal distortions introduced by the finite extent of the sensing fiber segment. Finally, FE models that tackle the most complex case of FE modeling comprising wave excitation and propagation in stratified media such as CFRP will be presented. Two different levels of accuracy were tried: (i) a rough approximation of CFRP by a synthetic orthotropic material and (ii) a rather sophisticated approach to the actual CFRP as layered composite material where each layer exhibits unidirectional symmetry of the elasticity tensor and where the orientation of these layers varies.

Based on the positive experience with the applied FEM analysis, the modeling of rather complex cases like plate wave excitation a propagation in stratified material or modeling a specifically robust constructions of the fiber-optic transducer were successfully tackled.

### 4.1 A benchmark setup for Lamb wave excitation and detection

To confirm the theoretical model of the intrinsic fiber-optic transduction mechanism, a specific setup for guided wave studies is required. This setup must be designed to allow easy experimental implementation as well as efficient FE analysis. Such a setup should enable a quantitative comparison of model and experiment. As the numeric models cover the excitation and propagation of elastic plate waves as well as their conversion into changes of the optical path length, a verification of the complete transduction chain is feasible.

In case of verification of the applied FEM analysis, the modeling of rather complex cases like plate wave excitation a propagation in stratified material or modeling a specifically robust constructions of the fiber-optic transducer can be envisioned.

### 4.1.1 Concept

To study the transduction mechanism of the fiber-optic strain transducer, both theoretically as well as experimentally, an appropriate setup has to be found. Elastic plate wave pulses are the preferred excitation of dynamic deformations that can be sensed by the fiber-optic transducers of interest. The related short term signals are not affected by slow variations of ambient variables like plate temperature. Furthermore, the typical strain amplitudes delivered by piezoelectric actuators matches perfectly into the dynamic range of intrinsic fiber-optic transducers. Use of a homogeneous plate material and guided wave pulses with plane or isotropic wavefront are advisable. Using piezoelectric actuators, however, only the excitation of circular crested guided waves is straightforward.

As reflections at plate boundaries introduce a major complication of Lamb wave response analyses, impractically large plates would be desired for basic investigations. A minimum complexity regarding the boundary reflections of Lamb waves may be expected from implementations based on isotropic plate waves and circular plates. If wave pulses expand from the center of the plate, their reflection is compressed into a single echo pulse if caused by the concentric plate boundary. Hence, a promising implementation is the use of circular piezoelectric actuator disks fixed at the center of circular plates featuring a radius that maintains a sufficient echo delay.

The chosen model implementation comprises two piezoelectric disk actuators, firmly attached in opposite position at the surfaces of the circular plate as shown in Fig. 4.1. The upside-downside symmetry of the arrangement prevents mode conversion from symmetric into antisymmetric plate wave modes and vice versa. Symmetric, antisymmetric, and mixed-mode guided waves can be generated individually under in-phase, opposite phase, and out-of-phase excitation, respectively.

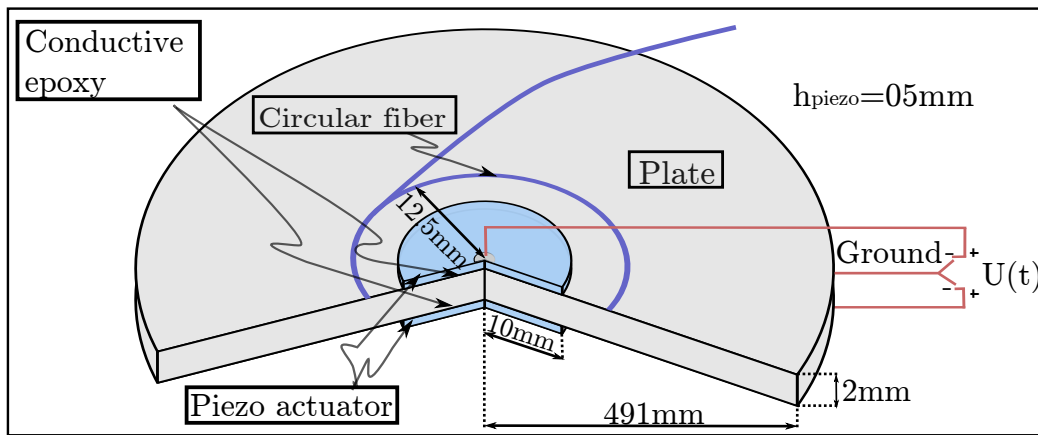


Figure 4.1: Schematic view of the simulation model geometry for fiber-optic transducer function verification of aluminum plate. A pair of piezoelectric disc actuators are glued with a low viscosity, conductive epoxy resin (Epotek H20E-LV) to the circular aluminum plate. The sensing fiber encircles the top placed actuator. All diameters are not to scale.

The affixed optical waveguide forms a concentric circle as shown in Fig. 4.1. Moreover, the circular waveguide senses changes of the circumference by circular crested compressional plate waves. In this special configuration, the hoop strain  $S_{\Theta\Theta}$  is directly proportional to

the radial displacement component  $u_r$ ,

$$S_{\Theta\Theta} = 2\pi u_r. \quad (4.1)$$

For this specific setup geometry, the circular fiber-optic transducer can be considered as radial displacement transducer, too. At the same time, the sensing fiber section has virtually zero extension in radial direction, i.e., in the direction of wave packet propagation. Hence, the extent of the attached sensing fiber segment introduces no frequency dependence of the mechanical transduction. Because of the axisymmetry of the complete setup, efficient two dimensional simulation models are applicable and the demand for computational capacity can be covered by ordinary PC's. Aluminum is a very common reference material for Lamb wave studies. Figure 4.2 depicts the phase and group velocities of the lowest Lamb wave

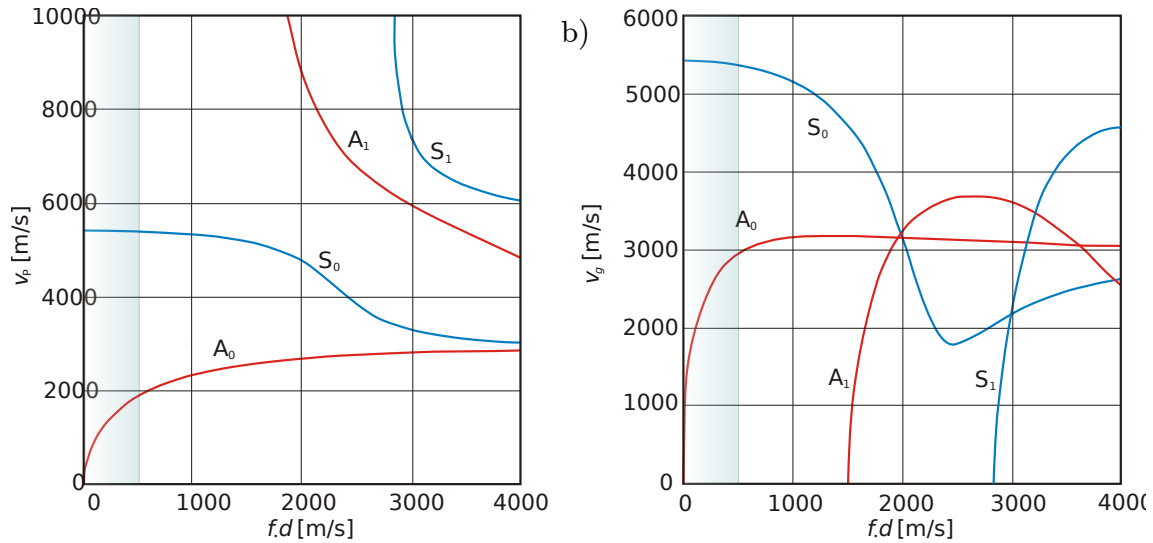


Figure 4.2: Typical phase and group velocity dispersion diagrams for the lowest two symmetric and antisymmetric modes of Lamb waves in aluminum plates. a) Phase velocity and b) group velocity.

modes versus the frequency-thickness product of the plate,  $f \cdot d$ . To ensure single mode operation, the product of the highest excitation frequency and the plate thickness, must not exceed the cut-off threshold for higher order modes, i.e.  $f \cdot d \approx 1500$  m/s. To avoid severe complications due to wave dispersion, however, the  $S_0$  mode should be used exclusively and the  $f \cdot d$  product should not exceed the indicated limit of about 500 m/s as indicated in Fig. 4.2, corresponding to a maximum frequency of about 250 kHz for a plate thickness  $d=2$  mm.

Suitable excitation signals for piezoelectric actuators are time-bandwidth limited pulses of the Morlet wavelets family, e.g.,

$$U(t) = U_0 \sin(2\pi f_0 t) \exp(-\ln(2)f_0^2 t^2), \quad (4.2)$$

where  $f_0$  denotes the center frequency and  $U_0$  scales the excitation voltage.

Such excitation forms are essential for the temporal separation of excitation pulses from their reflections. Temporal separation of primary and reflected signals becomes feasible if the minimum propagation time  $t_p$  from the winding radius of the fiber-optic transducer  $r_F$ , toward the plate periphery and back to the transducer's radial position exceeds the duration of the excitation pulse.

For optimum results,  $t_p$  must be uniform for all directions. According to the applied Morlet wavelet pulse of Fig. 4.3, the condition  $t_p \approx D/v_g \geq 6/f_0$ , where  $D$  stands for the plate diameter and  $v_g$  denotes the group velocity of the excited Lamb wave mode. The chosen Morlet wavelet guarantees  $f_{max} \approx 2f_0$  and for  $S_0$  in aluminum the low dispersion criterion translates into  $f_{max} \cdot d \ll 500$  m/s or  $f_{max} = 250$  kHz for  $d = 2$  mm.

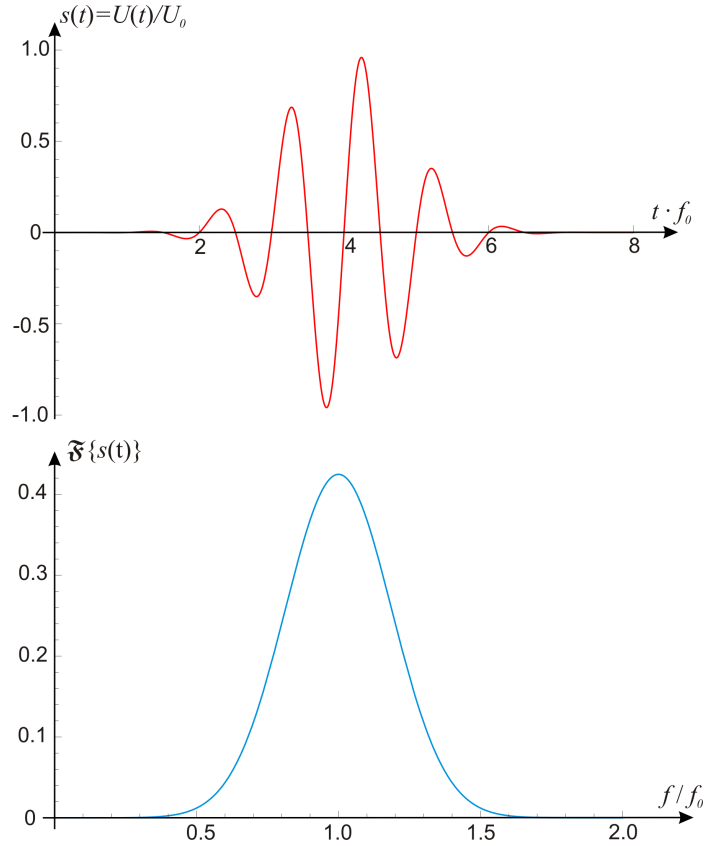


Figure 4.3: Temporal (top) and spectral (bottom) characteristic of a typical Morlet wavelet according to Eq. 4.2.

Equation 4.1 states that any axially symmetric radial displacement due to circular crested elastic waves leads to a uniform elongation or compression in tangential direction, i.e., along the direction of the fiber axis. As long as the tangential force exerted by the fiber doesn't modify the tangential strain in the plate appreciable, the mechanical loading due to the intrinsic fiber-optic transducer can be neglected. To achieve this, a sufficient plate thickness must be chosen.

The tangential fiber axis point perpendicular to the propagation direction of the circular crested waves, thence the transducer senses the tangential strain along the circular wavefront that is directly linked to the radial displacement by the wave. Assuming a rigid coupling between fiber and plate, the propagation constant of the light guided by the fiber follows the imposed strain immediately at least for the typical frequency range of ultrasound diagnostics. The radial position of the optical fiber,  $r_F$ , should be far enough from the plate circumference to reliably discriminate echoes from primary signal on the one hand, and far enough from the piezoelectric actuator to enable sufficient diminution of the evanescent higher order elastic wave modes on the other hand. For good separation between echoes and primary excitation,

$f_0$  should be chosen as high as possible to shorten the pulse length. However, the higher  $f_0$  the smaller the thickness of the plate according to the dispersion dictated  $f_{max}d$  limit.

### Design guidelines for the reference model.

For a straightforward comparison with measurements, the parameters of the FEM model should consider the limits imposed by the accessible equipment and materials. For the current work, the maximum feasible sampling rate of 500 kHz imposes a severe bandwidth limit for the Lamb waves of  $f_{max} \leq 250$  kHz. Circular disks exhibiting a diameter of up to 0.5 m could be obtained from EN AW6082 plate material, which is an easily machinable Al-Si-Mg-Mn alloy.

The discussed conditions result in design rules for the FE model as follows: for aluminum, the cut-off of higher order Lamb wave modes requires  $f_{max}d < 1.5 \cdot 10^3$  m/s, which is equivalent to  $d < 6$  mm while the more severe dispersion requirement suggests  $d < 2$  mm for  $f_{max} = 250$  kHz. With the propagation velocity of compressional waves pulses of about  $v_g \approx 5500$  m/s in aluminum, the relation for  $t_p$  derived above, requires plate diameters of  $D$  [m]  $> 3.3 \cdot 10^4 / f_0$  [Hz]. For the experiments  $f_0 = 100$  kHz or  $f_{max} = 200$  kHz seems appropriate leading to a minimum plate diameter of 0.33 m.

### 4.1.2 Implementation

The implemented plate has a diameter of 0.491 m to achieve some extra pulse echo separation and a thickness  $d = 2$  mm, which was adopted for the FEM as well. Accurate material parameters for the plate material EN AW6082 were not found, hence, for the simulations data for EN AW6070 (UNS A96070) were taken from the COMSOL material library (Young's modulus  $E = 69.14$  GPa, shear modulus  $G = 26$  GPa, Poisson's ratio  $\nu = 0.33$ , density  $\rho = 2700$  kg/m<sup>3</sup>). In accordance with the planned experiments, the aluminum alloy plate of the FE model was instrumented with a pair of piezoelectric actuators exhibiting a diameter and thickness of  $2r_{PZT} = 10$  mm and 0.5 mm, respectively. The piezoelectric material used in the present section has been chosen from the COMSOL Multiphysics material library. This database offers the material PZT-5A (see Tab. 4.1), a PbZrTi ceramics featuring quite comparable properties to PIC255 used for the measurement setup.

The minimum bending radius  $r_F$  of the optical fiber cannot be derived as simple as the plate dimensions. Beside the disappearance of evanescent modes, the damping of guided light waves due to fiber axis curvature must be considered. The assumption of negligible evanescent modes at  $r_F$  can be checked by inspection of the FEM results. The implemented fiber for experimental investigation was chosen as  $r_F = 12.5$  mm based on prior experiences [50].

The schematic of the simulation model in Fig. 4.4 gives an impression of the small cross-section of the fiber (0.25 mm diameter inclusive cladding and coating). Because of the small cross section of the optical fiber it is usually omitted in the finite element models which is justified from a comparison of with/without fiber results. The low viscosity of the super glue adhesive used for the implementation leads to an extremely small gap between fiber coating and plate, which has negligible effect on the mechanical coupling between fiber and plate. Consequently, the adhesive gap is omitted in the FE model.

An electrical excitation signal according to Eq. 4.2 is applied to each piezoelectric actuator of the model with  $f_0 = 100$  kHz,  $U_0 = \pm 40$  V, in a fashion that evokes the excitation of symmetric Lamb wave modes preferably.

Characteristics	symbol	PZT 5A	PIC255
Density	$\rho$ [Kg/m <sup>3</sup> ]	7750	7800
Curie temperature	$T_c$ [°C]	-	350
Relative permittivity in the polarization direction	$\varepsilon_{33}/\varepsilon_0$	1700	1750
Perpendicular to the polarization	$\varepsilon_{11}/\varepsilon_0$	1730	1650
Dielectric loss factor	$\tan \delta$ [10 <sup>-3</sup> ]	0	20
Piezoelectric deformation coefficient, piezo modulus	$d_{31}$ [pm/V]	-171	-180
	$d_{33}$ [pm/V]	374	400
	$d_{15}$ [pm/V]	584	550
Elastic Constant	$s_{11}^E$ [10 <sup>-12</sup> m <sup>2</sup> /N]	16.4	16.1
	$s_{33}^E$ [10 <sup>-12</sup> m <sup>2</sup> /N]	18.8	20.7
Mechanical quality factor	$Q_m$	-	80

Table 4.1: Characteristics of piezoelectric PZT-5A of COMSOL Multiphysics material library and PIC255 from the PI Ceramic company.

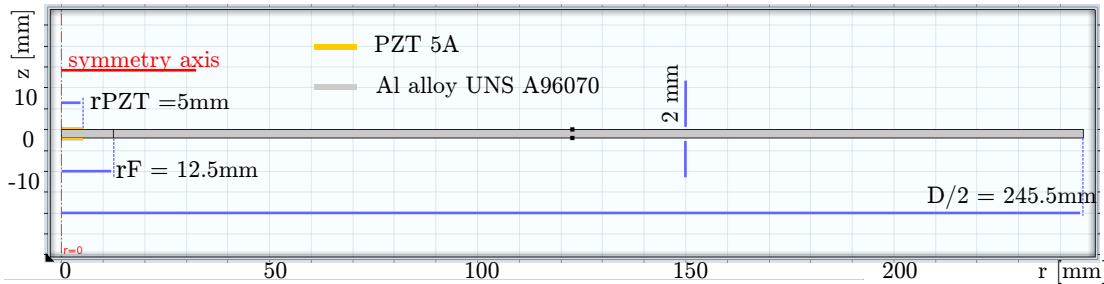


Figure 4.4: Geometry of the implemented 2D cylinder symmetric FE model featuring zero force at all edges. The aluminum plate is kept at ground potential and a common excitation potential is applied to the free base surfaces of the antiparallel polarized PZT discs. Instead of an attached fiber, an artificial domain boundary is introduced to probe the simulation results at  $r = r_F$ .

FEM simulations of the transient behavior of the described setup were performed for a period of 1 ms using time step parameters  $\leq 200$  ns.

### 4.1.3 FEM results

The twin circular actuator configuration enables the exclusive excitation of either symmetric or antisymmetric guided waves as well as controllable mixtures of both types [107]. The actuators polarizations are parallel which is different from the experimental work, where anti parallel orientation was chosen, in Fig. 5.2. Figure 4.5 displays the excitation signals applied to the actuators, whereas Fig. 4.6 shows the time course of the radial displacement at the circumference of the actuator disks,  $r = r_{PZT}$ . The simulations reveal, that a single excitation pulse evokes a virtually unlimited chain of echoes with a delay corresponding to the round-trip time of the pulse towards the plate periphery and back to the axis. Hence, reflections of the guided wave pulse packets at the periphery are complemented by a similar effect at the axis. It was been shown with excitation at the periphery that the reflections at the axis occur if the piezoelectric actuators are not present. Furthermore, the transient results indicate an echo delay of about 90  $\mu$ s that gives sufficient separation of subsequent

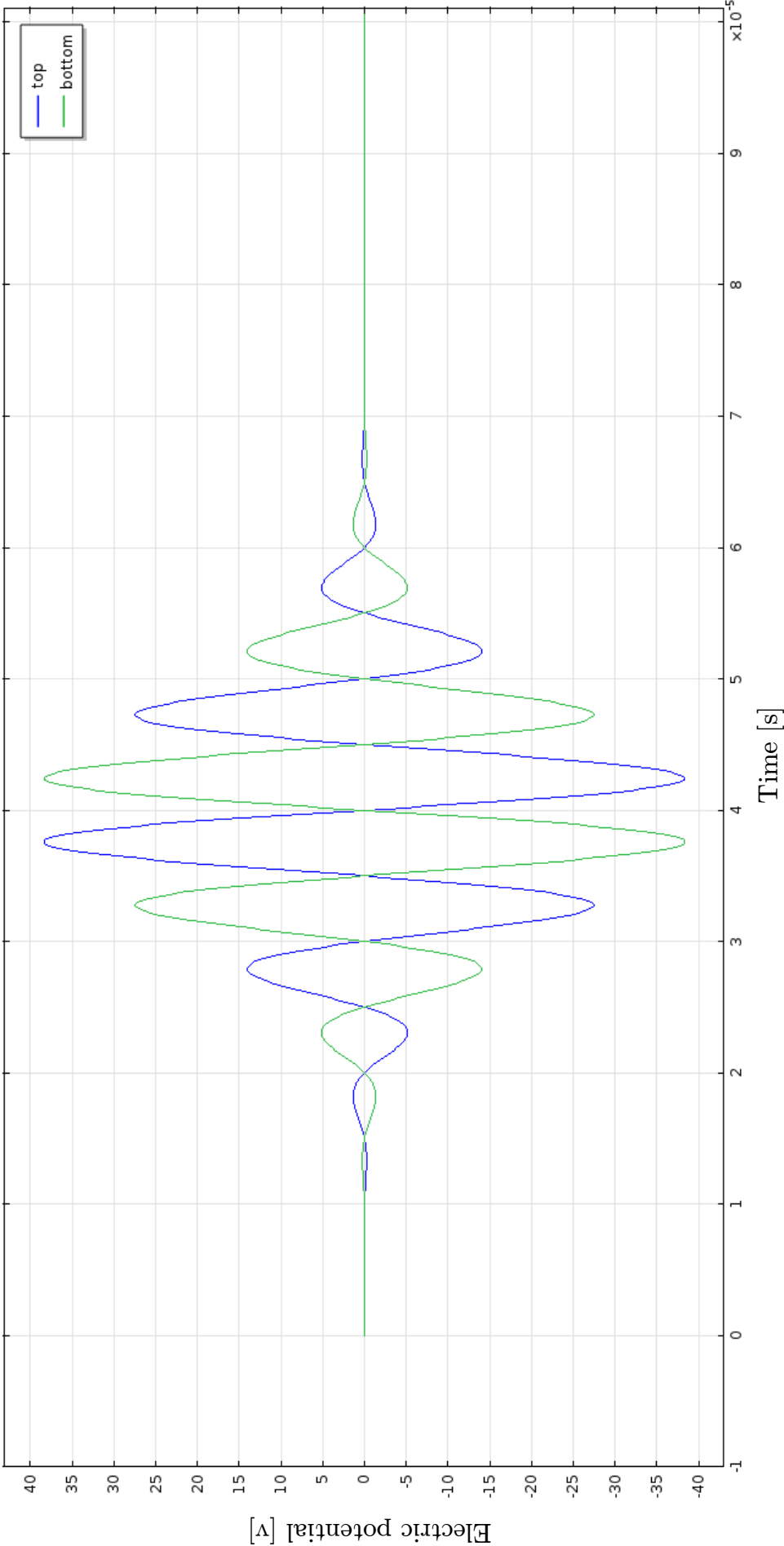


Figure 4.5: Excitation voltages applied to the top and bottom PZT actuator disks exhibiting parallel polarization. With the selected polarity, the top and bottom actuator disks exhibit identical deformation.

pulses.

The train of varying pulse echoes exhibit a regular delay of about 90  $\mu\text{s}$  confirming that a single propagation velocity predominates. Furthermore, the compact pulses indicate low dispersion. From the echo repetition and the plate diameter of about 0.5 m a propagation velocity of 5500 m/s can be concluded. These findings confirm that the  $S_0$  mode of the aluminum plate is excited exclusively. As the plate material model is assumed to be free of mechanical loss, the magnitude of the multiple echoes and the pulse length doesn't change appreciably with elapsed time. Noticeable losses due to the excitation of evanescent modes required for the satisfaction of the boundary conditions around the actuator disks can be excluded as well.

At the circumference of the actuator disk, the echoes are smaller in amplitude by a factor of about four for two reasons. First, the displacement causing the primary pulse contains contributions by the evanescent modes, since the excitation happens right at the plate surfaces which implies a stress distribution in the plate that differs from any single Lamb mode. Then, the simulated displacement of the echoes represents a superposition of the wave packet propagating toward the axis and the subsequent packet expanding towards the periphery. The magnitude of these echoes is further diminished due to the loading of the plate by the rigid piezoelectric actuator disks which cause distributed reflections.

Contrary to the radial displacement at the piezoelectric actuator disks, the magnitude of the echoes at  $r_F$  is somewhat larger than the primary pulse Fig. 4.7. Two assumptions support this surprising feature. First, the evanescent modes of the excited plate waves have disappeared at  $r_F$ . Second, due to the vicinity of the symmetry axis, the radial displacement at  $r_F$  comprises contributions from the inward propagating as well as from the outward propagating pulse packets. Because of the small dispersion of the  $S_0$  Lamb wave mode, the wavelength  $\lambda \approx v_g/f_0 = 5.5$  cm is decisive for interference effects. At  $r_F \approx \lambda/4$ , constructive interference of the packets occurs because of the displacement node forced by symmetry at the axis. In contrast, partial destructive interference is to be expected at the actuator circumference because  $r_{PZT} \ll \lambda/4$ .

The FEM model enables answers to the question how far the evanescent modes reach into the plate. Figure 4.8 shows the result of a symmetric actuation at the top and bottom surface of the plate. The intended  $S_0$  Lamb wave mode leads to virtually flat wavefronts with respect to the vertical coordinate. The grid deformation shown in Fig. 4.8 signals that the evanescent deformation extend only for about 1 mm beyond the disk actuators. At the radial position of the fiber-optic waveguide, indicated by a vertical domain boundary, only the propagating wave contributes to the radial displacement. Finally, the radial displacement at the plate circumference is displayed in the Fig. 4.9. The simulated pulse repetition period amounts about 91.9  $\mu\text{s}$  determined from the lag of the 9th echo with respect to the primary pulse, i.e., 827  $\mu\text{s}$ . That finding corresponds with a propagation velocity  $v_G = 5343$  m/s. Very precise estimates are not feasible as the pulse shape varies from echo to echo. The pulse magnitudes at the plate circumference are significantly smaller than that near the axis and determined by two effects (see Figures 4.6, 4.7 and 4.9). First, energy conservation requires, that the magnitude of any circular crested wave packet decreases with  $1/\sqrt{r}$  from the symmetry axis. Second, the free surface condition at the plate circumference leads to a constructive superposition of the displacement induced by the expanding wave packet and the subsequently contracting wave packet traveling toward the plate axis.

To conclude this section, it can be said that the FE model of the reference setup works as expected. Exclusive excitation of the  $S_0$  mode was obtained by symmetric actuation. The chosen bending radius of  $r_F = 12.5$  mm of the optical waveguide, corresponding to a radial

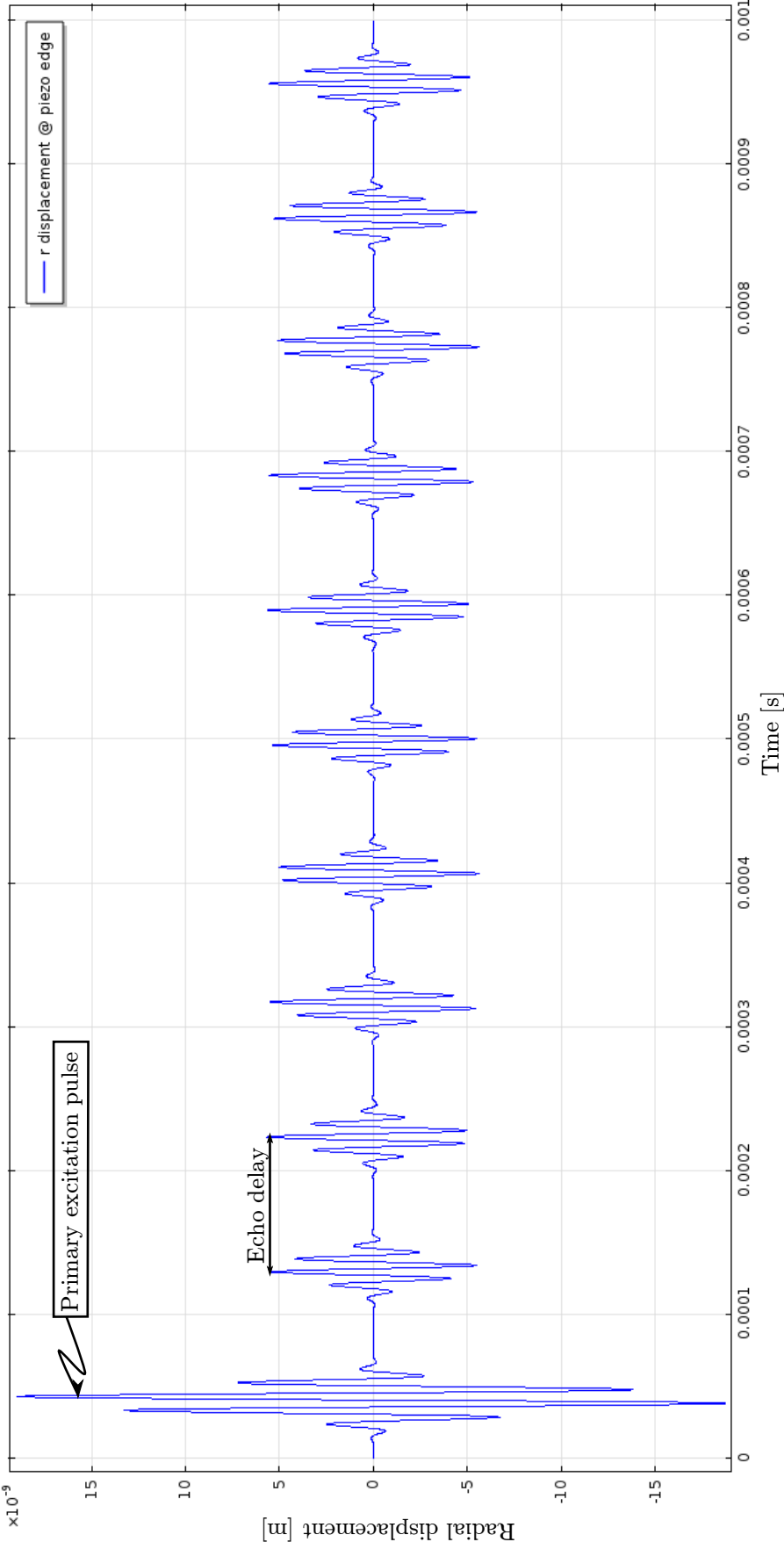


Figure 4.6: Simulated radial displacement of the top and bottom plate surface right at the circumference of the piezoelectric disks  $r = r_{PZT}$ . Besides the primary pulse numerous echoes occur.

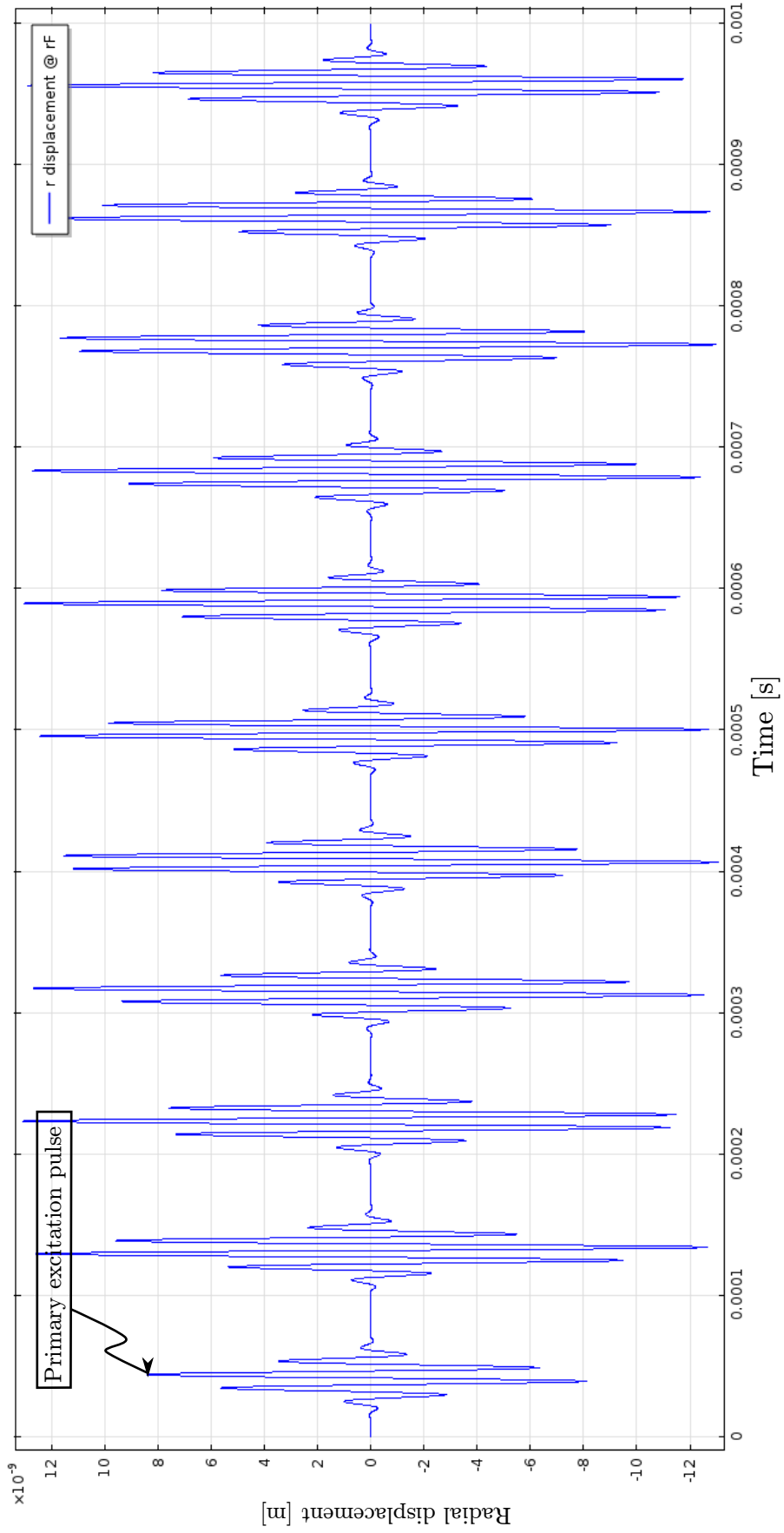


Figure 4.7: Displacement at the assumed radial position of the optical waveguide ( $r_F = 12.5$  mm).

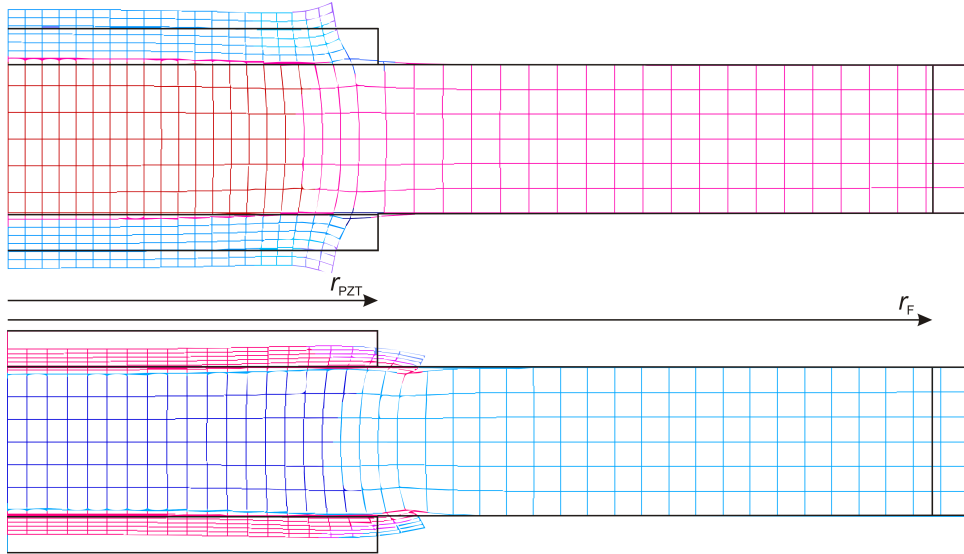


Figure 4.8: Highly exaggerated snapshots of transient deformations near the piezoelectric actuators. The grid color encodes the volumetric strain. The pictures are taken at the moments of extreme deformation. The undistorted shape is indicated by black lines. Symmetric actuation with a center frequency of 100 kHz was used for the simulation.

distance of 7.5 mm from the actuator disk, guarantees sufficient by large delay of evanescent distortions. Thanks to the low dispersion of the  $S_0$  mode, the plate response consists of an elastic wave packet that bounces quasi periodically outward and inward in the aluminum disk. Further consideration will be performed in conjunction with experimental outcomes reported in chapter 5 and the comparative discussion and interpretation in chapter 6.

#### 4.1.4 Exploration model for spurious effects of fiber-optic transducers

The transduction efficiency of interferometric fiber-optic transducers can be enhanced markedly by extending the length of the interacting fiber segment. An elegant method is to form a fiber coil with multiple turns. That results in an omnidirectional sensitivity characteristic but implies also a very specific frequency dependence of the transduction of plane guided waves. Roughly speaking, the frequency dependence is determined by the ratio of the coil diameter to the wavelength of the guided wave.

It is of great interest whether or not such fiber-optic transducers impose loading effects on the plate to be investigated. For this purpose, a specific 3D FE model was devised which is based on small rectangular plates of a homogeneous material. Therefore, multiple echoes due to boundary reflections severely limit the period of simple interpretation of the FEM results. Nevertheless, important transduction characteristics and eventual spurious effects of the fiber-optic transducer can be visualized.

More application related material parameters are used for this work that aim at the popular CFRP family of materials. However, to avoid computational costs, an orthotropic one is first used.

The selected carbon fiber reinforced polymer consists of six laminated layers as described in subsection 2.4.3 where, each layer contains parallel aligned fibers embedded in epoxy resin.

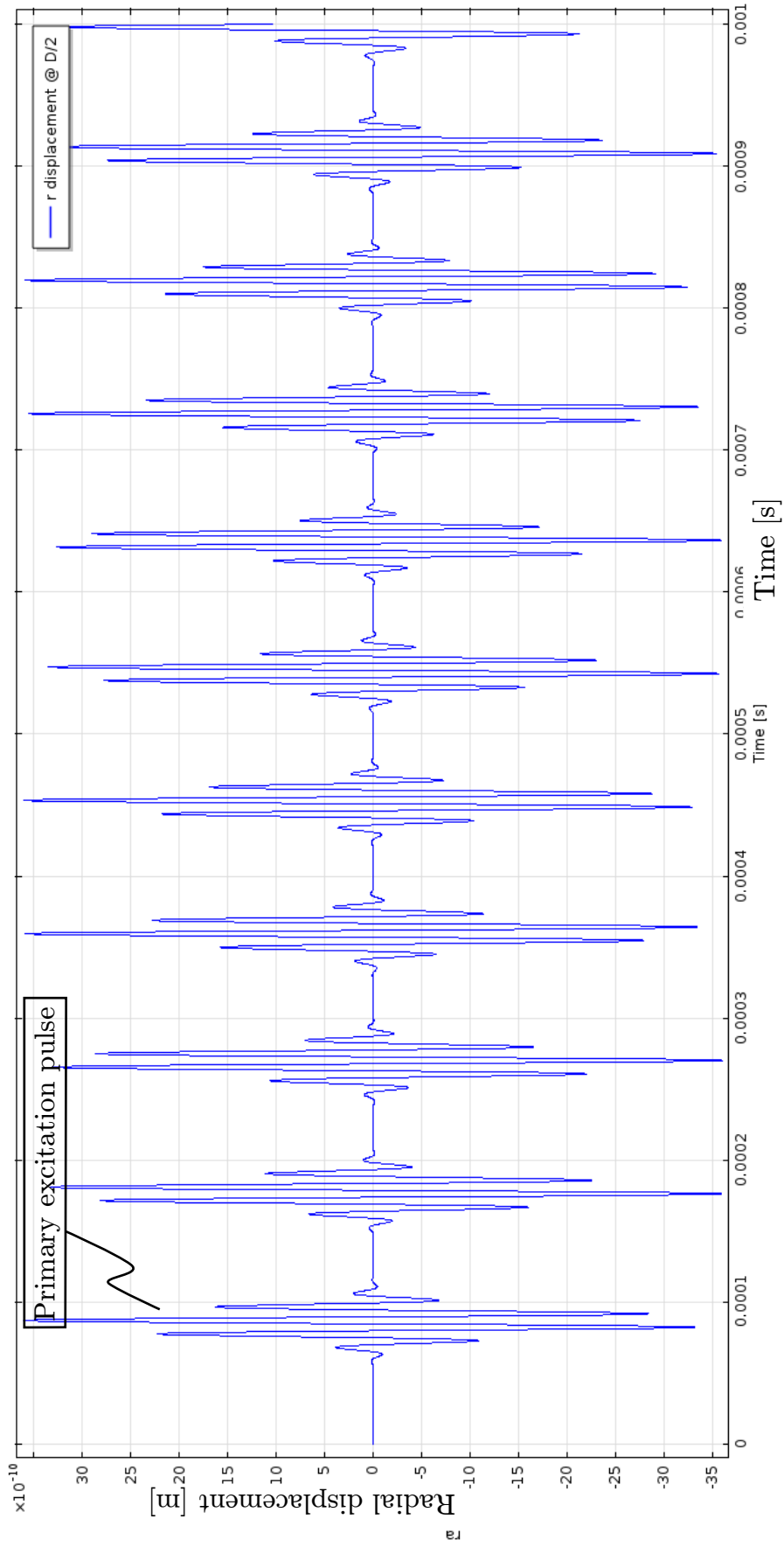


Figure 4.9: Radial displacement at the plate circumference  $r = r_D$ .

Thus, each layer features unidirectional or transverse isotropic symmetry of the elasticity tensor [108]

$$\mathbf{c} = \begin{bmatrix} c_{11} & c_{12} & c_{13} & 0 & 0 & 0 \\ c_{12} & c_{22} & c_{13} & 0 & 0 & 0 \\ c_{13} & c_{13} & c_{33} & 0 & 0 & 0 \\ 0 & 0 & 0 & c_{44} & 0 & 0 \\ 0 & 0 & 0 & 0 & c_{55} & 0 \\ 0 & 0 & 0 & 0 & 0 & (c_{11} - c_{12})/2 \end{bmatrix}.$$

The fiber orientations in each layers are rotated from layer to layer according to the sequence -45, 45, 0, 90, 45, and -45 degree. Thus the stratified CFRP plate lacks of a symmetry plane and the six layer composite forms an inhomogeneous and anisotropic solid. For the purpose of this subsection, it is supposed that the 6-ply laminate plate can be approximated well by an orthotropic bulk material. The simulation of this multilayer material is postponed to subsection 4.1.5 while this subsection deals with the orthotropic approximation.

Orthotropic symmetry of the elasticity matrix means nine independent elastic constants of the compliance matrix, given by [109] or chapter 2.:

$$[\mathbf{c}]^{-1} = \begin{bmatrix} 1/E_{11} & -\nu_{21}/E_{22} & -\nu_{31}/E_{33} & 0 & 0 & 0 \\ -\nu_{12}/E_{11} & 1/E_{22} & -\nu_{32}/E_{33} & 0 & 0 & 0 \\ -\nu_{13}/E_{11} & -\nu_{23}/E_{22} & 1/E_{33} & 0 & 0 & 0 \\ 0 & 0 & 0 & 1/G_{23} & 0 & 0 \\ 0 & 0 & 0 & 0 & 1/G_{13} & 0 \\ 0 & 0 & 0 & 0 & 0 & 1/G_{12} \end{bmatrix},$$

with  $\nu_{12}/E_{11} = \nu_{21}/E_{22}$ ,  $\nu_{13}/E_{11} = \nu_{31}/E_{33}$ , and  $\nu_{23}/E_{22} = \nu_{32}/E_{33}$ .

A set of the orthotropic elasticity parameters was selected for these simulations to approximate typical mechanical properties of carbon fiber reinforced material (Young's moduli,  $E_{11} = E_{22} = 31.51$  GPa,  $E_{33} = 8.05$  GPa; Shear moduli  $G_{12} = 12.2$  GPa,  $G_{23} = G_{13} = 3.07$  GPa; Poisson ratio:  $\nu_{12} = 0.239$ ,  $\nu_{23} = \nu_{13} = 0.423$  and density  $\rho = 1600$  kg/m<sup>3</sup>). Target of the simulations is a plate of thickness  $d = 0.75$  mm with typical dimensions  $4.5$  cm  $\times$   $12.5$  cm and a complementary piece of the plate ( $4.5$  cm  $\times$   $2$  cm). This extension of the plate features marked Rayleigh damping  $\alpha_{dM} = 1000$  1/s and  $\beta_{dk} = 1e^{-6}$  s. It was added to the model in order to reduce the influence of the reflected wave packet. They emerge at the opposite edge of the plate, which was kept fixed. At the lateral side faces of the plate, symmetry conditions were applied to avoid reflections and energy loss at these boundaries. The small thickness of the plate helps to see loading effects by the optical fiber.

Plane Lamb waves are used to enable easy analysis. They are excited artificially at one edge face of the plate by imposing a uniform time dependent displacement there. The structure is preferably excited by a single-sine-burst pulse displacement  $s(t)$  according to Eq. 4.3 which was imposed on one edge of the plate. Due to the obeyed  $f \cdot d$  product, this excitation yields exclusively compressional waves of the  $S_0$  mode resulting in very instructive patterns of the excitation.

### Mechanical modeling of fiber-optic coil transducers

Made of single mode fiber, the strain detectors are alternatively implemented as flat spiral coil featuring 5-, or 10-turn as well as a cylindrical coil with 5 turns. All coils feature an outer diameter  $d$  of 25 mm. In contrast to the practical fiber, the model for numerical analyses exhibit a  $250 \mu\text{m} \times 250 \mu\text{m}$  square cross section. This approach results in a tremendous decrease

of the mesh complexity which reduces computational efforts accordingly. The cross section manipulation requires a corresponding adaptation of the mechanical data. The core and cladding of the monomode fiber have the Young's modulus of vitreous silica,  $E_F = 73$  GPa, a Poisson number of  $\nu_F = 0.28$ , and a density of  $\rho_F = 2201$  kg/m<sup>3</sup>. Compared to these specifications, the coating has a much lower rigidity. Hence, the Young's modulus and the density of the synthetic square-shaped fiber is computed according to the cross sectional ratio of the 125  $\mu\text{m}$  fiber core and the 250  $\mu\text{m}$  square replacement,  $\pi/16$ , leading to  $E = 14.3$  GPa. Similarly,  $\nu = 0.22$  and  $\rho = 431.95$  kg/m<sup>3</sup> is obtained for the Poisson number and the density of the square fiber replacement, respectively.

To take into account the strength of the coating, a rough approximation was made by taking  $E_F/4 = 18.25$  GPa for the simulations. This value is  $\sim 10\%$  higher than a value of  $16.56 \pm 0.39$  GPa derived from the measured modulus of a coated fiber [110]. The higher value of 18.25 GPa seems more appropriate since the simple cross section scaling does not consider the strength of the adhesive that forms a fillet underneath the coated fiber.

In all cases, the simulated transducer response is derived from changes of the computed length of the spiral coil or helix of the model. This length change is obtained by numerical integration of the strain along one edge of the square shaped fiber model. Such integrations are carried out for each simulation time step of typically 0.2  $\mu\text{s}$  for an excitation of  $\omega = 2\pi \cdot 10^5$  s<sup>-1</sup>. As an example, a 10-turn spiral wound fiber coil model can be seen from Fig. 4.10 aside with the applied plate model.

The generation of Lamb waves, either the symmetric compressional  $S_0$  or the antisymmetric flexural  $A_0$  mode, happened at the right end face of the plate model. A time dependent displacement according to Eq. 4.3 called single-sine burst is applied in parallel to either the  $-x$ -direction to excite compressional  $S_0$  waves, or parallel to the  $z$ -direction for preferably antisymmetric  $A_0$  flexural waves.

$$s(t) = A \sin(\omega t) \sin^2(\omega t/2), \quad 0 \leq t \leq 2\pi/\omega. \quad (4.3)$$

The parameter  $A$  (typically  $10^{-4}$  mm) in Eq. 4.3 denotes the displacement amplitude and  $\omega = 2\pi \cdot 10^5$  s<sup>-1</sup> the angular frequency of the excitation. The center frequency of the excitation was chosen low enough to enable exclusively the fundamental  $S_0$  or  $A_0$  modes which propagate in the  $-x$ -direction. The transient simulation covered typically a time span of 100  $\mu\text{s}$ . As the propagation velocity of compressive wave pulses is about 5000 m/ $\mu\text{s}$ , the primary wave experiences multiple reflections within the simulation period. The used waves packet excitation is shown in Fig. 4.11.

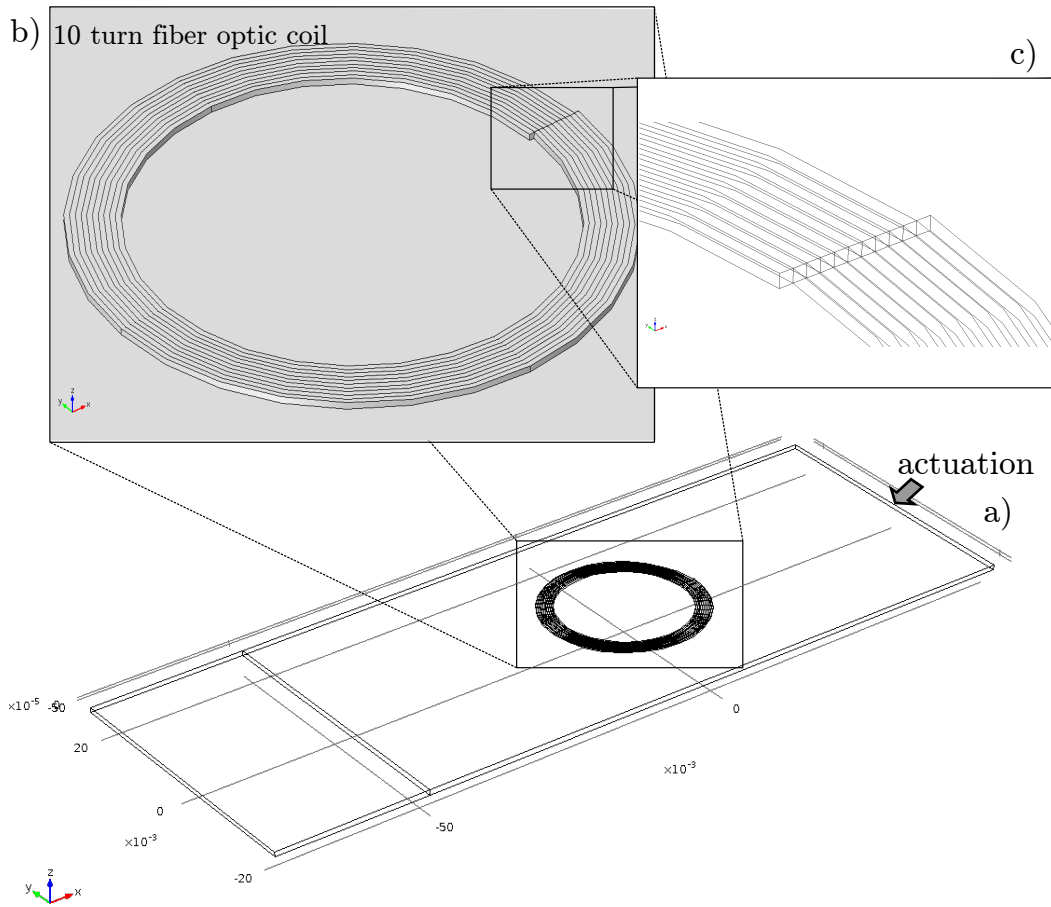


Figure 4.10: FEM model of the fiber coil. a) the selected  $x$ ,  $y$ , and  $z$  plate dimensions are 125, 45, and 0.75 mm, respectively. The insets b) and c) depict the approximations applied to the (10-turn) fiber-optic coil.

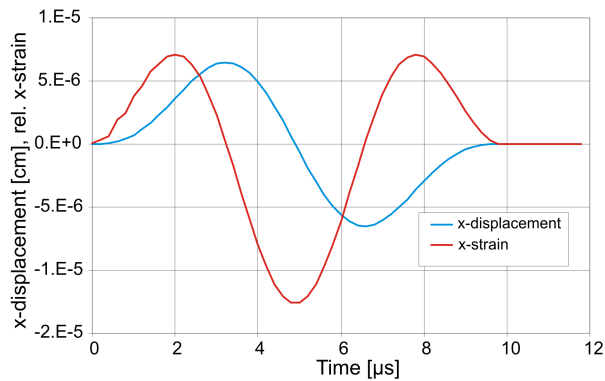


Figure 4.11: Wave packet excitation function used for edge face excitation. The uniform displacement  $s(t)$  in  $x$ -direction at a lateral plate border excites a compressional  $S_0$  mode. The resulting strain for this case is also drawn.

In case of a helix coil transducer model, a pile of five circles of the square shaped fiber was formed. The diameter and position remained as in the previous case.

### Simulation results for spiral fiber coils

Figure 4.12 shows snapshots of the simulated propagation of a Lamb wave packet where the colors scales the displacement in  $x$ - and  $y$ -direction. A 5-turn fiber coil was used in this case. A plate of dimensions, thickness  $d = 0.75$  mm,  $4.5$  cm  $\times$   $12.5$  cm and a complementary piece of the plate ( $4.5$  cm  $\times$   $2$  cm) like in previous sections is used.

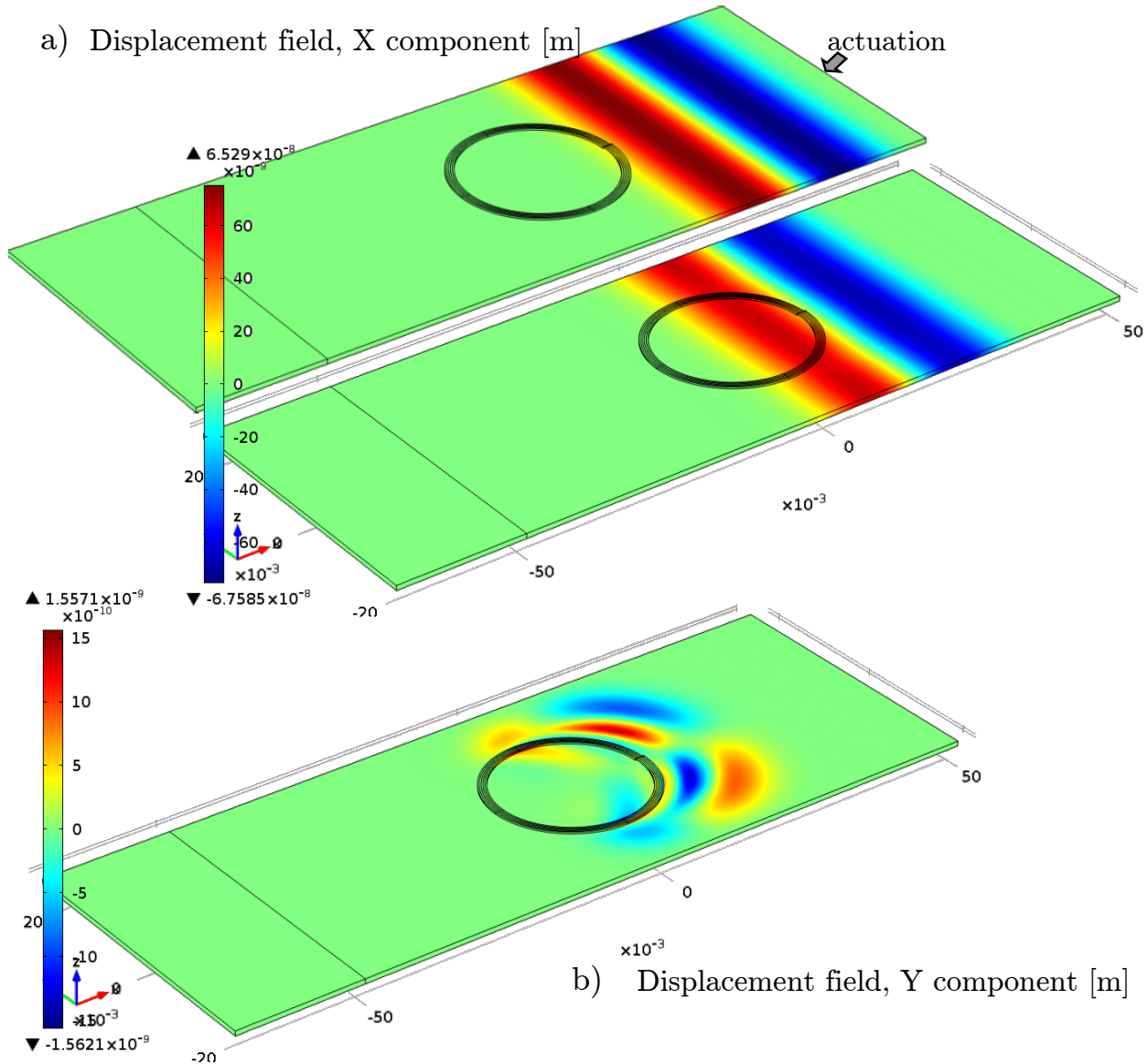


Figure 4.12: Snapshots of the simulated propagation of an  $S_0$  sine-burst wave with 100 kHz center frequency. The color scales displacement components at the plate surface due to the elastic wave. From top to bottom:  $x$ -displacement at  $10 \mu\text{s}$  and  $13 \mu\text{s}$ , and  $y$ -displacement at  $13 \mu\text{s}$ . As the primary wave lacks any  $y$ -displacement, the bottom picture signals repercussion by the attached fiber coil.

According to the applied edge excitation, the main constituent of the pulse packet should be an  $S_0$  mode guided wave featuring a typical propagation velocity of about 5000 m/s. This picture is confirmed from a comparison of the two snapshot pictures of wave packet related  $x$ -displacements Fig. 4.12 a. As the primary wave packets lacks any  $y$ -displacement, the bottom

sub-figure indicates reflections by the attached fiber coil. It can be further concluded from Fig. 4.12 *a*, that the repercussion effect of the attached coil is small since the resolution of the applied color scale of sub figure 4.12 *b* is enhanced by a factor of about 40 compared to the  $x$ -displacement pictures. In addition, weak mode conversion from symmetric modes to antisymmetric modes, or vice versa, must take place since the attachment of the fiber coil to only one of two free surfaces disturbs the symmetry of the model.

Figure 4.13 details the simulated time courses of the relative fiber elongation for a 5-turn and a 10-turn spiral wound fiber-optic coil.

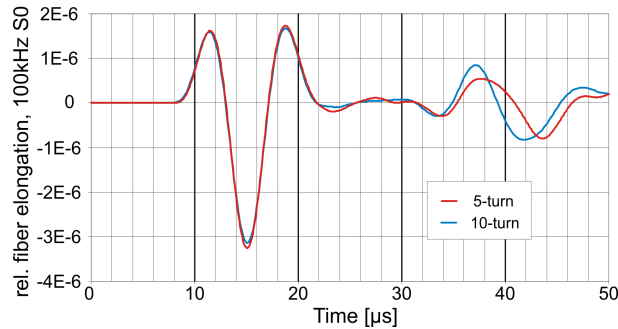


Figure 4.13: Simulated relative elongation of spiral coils of the glass fiber 0.75 mm CFRP for a 100 kHz  $S_0$  mode with an excitation amplitude of 100 nm. Spiral coils 5- and 10-turn, and an outer diameter of 25 mm were applied, respectively. The strain signal associated with the Lamb wave and the excitation function at the edge are not to scale and shown to illustrate their time dependencies.

A comparison of the fiber elongation responses with the signals of Fig. 4.11 confirms that, in case of plane plate waves the fiber-optic coils acts as strain transducers. As the relative sensitivities of both coil arrangements are comparable, one can conclude that the plate loading by the attached optical fiber has no significant influence on the conversion efficiency. In absolute terms, peak elongations of  $-1166$  nm and  $-2286$  nm are obtained for the 5-turn and 10-turn spiral coil, respectively. These elongations compare well with a peak to peak  $x$ -displacement of the Lamb wave pulse of 130 nm as the 5-turn and 10-turn wound fibers approximate the  $x$ -axis orientation 10 and 20 times, respectively.

As discussed in Chapter 3, the spatial extension of a fiber-optic transducer implies convolution distortions of the transduced signal which becomes significant at short wavelengths of the guided elastic waves. The main effect is an extended pulse length relative to the strain pulses in the plate. Figure 4.14 shows the normalized responses to an edge displacement excitation according to Eq. 4.3 with  $\omega = 2\pi \cdot 80$  kHz.

The normalized curves of the plate strain and the simulated fiber elongation illustrate the temporal stretching due to the spatial extension of the 5-turn spiral fiber coil featuring an outer diameter of 25 mm. At 80 kHz, the wavelength of  $S_0$  Lamb waves amounts to 62.5 mm. However, the spectra of the single sine-burst pulse as well as the strain pulse contain much higher frequencies than 80 kHz as Fig. 4.15 reveals.

### Simulation results for helical fiber coils

Further studies were devoted to helical fiber coils as an alternative option for spiral strain transduction. The helical fiber coil is composed of five circular fiber, placed on the top of

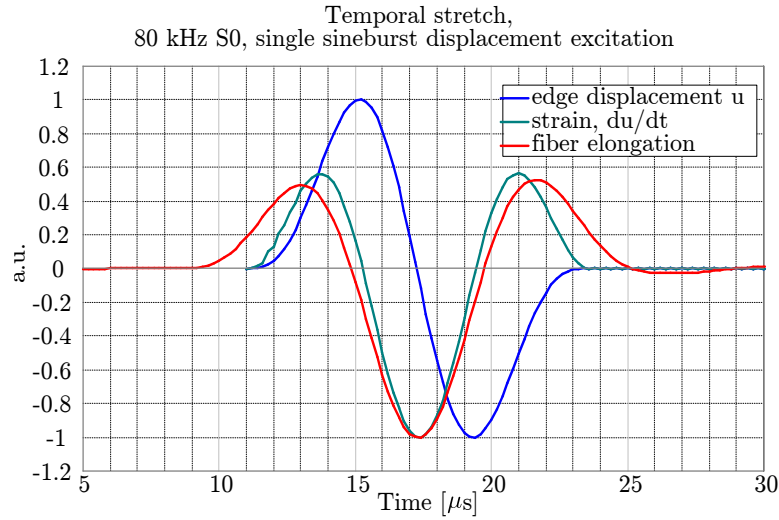


Figure 4.14: Normalized traces of the exciting edge displacement, the related strain pulse, and the simulated fiber elongation indicating the temporal extension of the fiber-optic response.

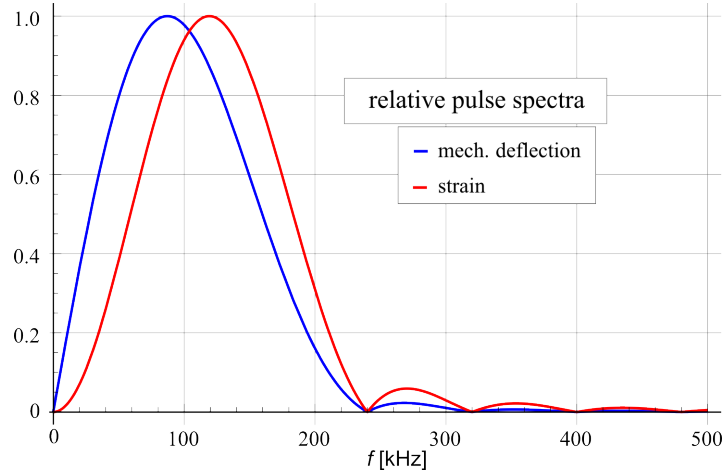


Figure 4.15: Relative amplitude spectra of the 80 kHz single sine-burst displacement excitation (blue) and the corresponding strain pulse (red).

each other, forming a hollow helix with 25 mm diameter and  $5 \times 250 \mu\text{m}$  of height. The helical transducer is placed at the center of the 100 mm square orthotropic structure with isotropic damping of  $\eta_s = 0.001$ . The main monitoring structure is completed at the left part with the same material  $100 \text{ mm} \times 20 \text{ mm}$  with Rayleigh damping (mass  $\alpha_{dM} = 1000 [1/\text{s}]$  and stiffness  $\beta_{dK} = \exp(-6) [\text{s}]$ ). The excitation signal 4.3 has been applied at the right edge in the  $-x$ -direction for symmetric Lamb wave and  $z$ -direction for antisymmetric. For the mechanical simulations, the helix was modeled as a staple of five,  $250 \mu\text{m} \times 250 \mu\text{m}$  square cross section fiber rings.

As expected, the simulated sensitivities for  $S_0$  Lamb waves are quite comparable to the results obtained for spiral fiber coils but here with a stronger wave reflection at transducer level in  $z$ -displacement, which can be seen in the Fig. 4.16. The  $x$ - and total displacement view of the  $S_0$  elastic wave in the snapshots in the figures 4.16 c 4.16 d, respectively, relative the transducer influence of the propagated waves.

A marked difference was observed for  $A_0$  Lamb waves, where flexural plate deformations lead to interesting out-of-plane effects. The fiber deformations are not uniform along the

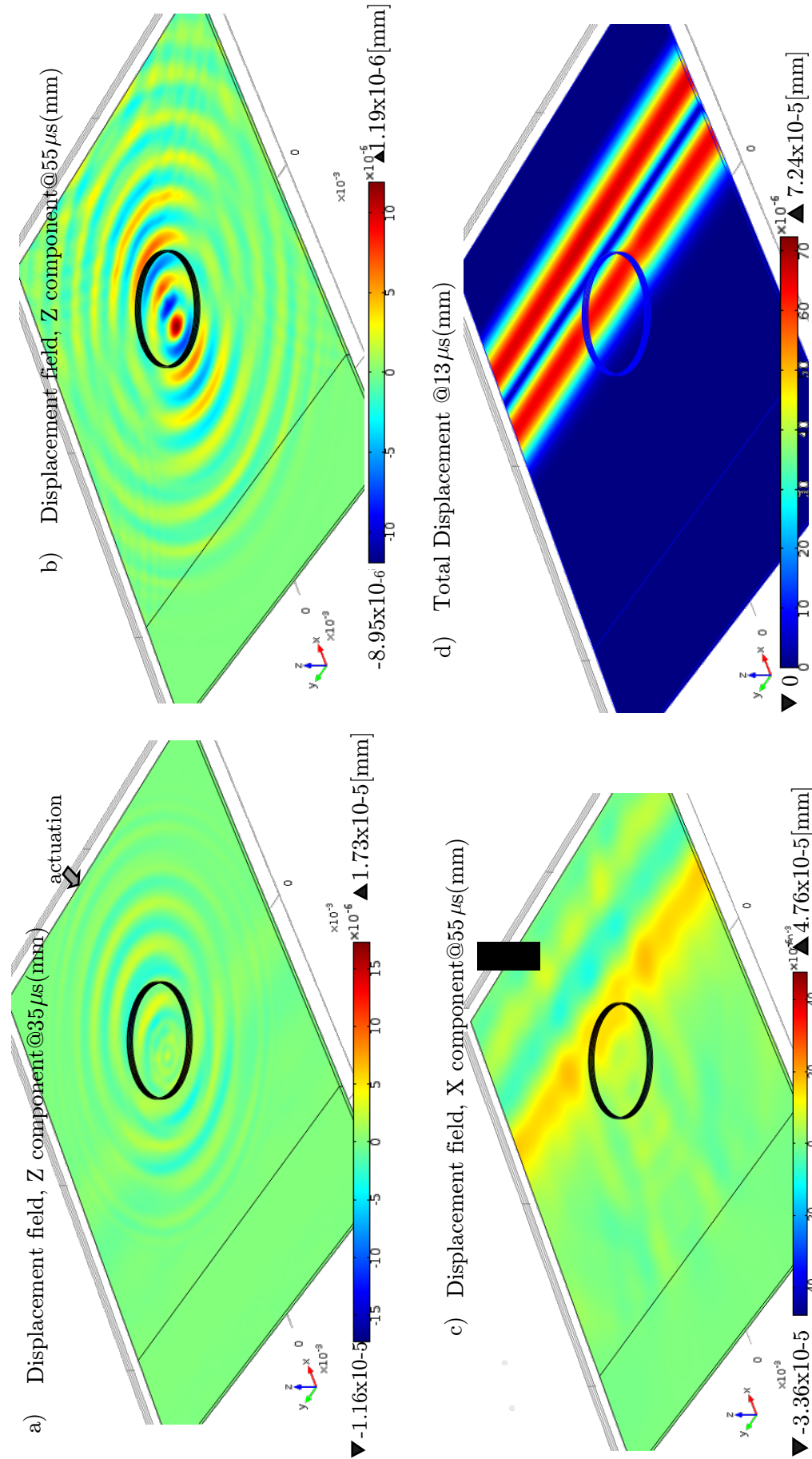


Figure 4.16: Snapshots of the simulated propagation of an  $S_0$  sineburst wave with 100 kHz center frequency. a) and b)  $z$ -displacement at 35  $\mu$ s and 55  $\mu$ s, respectively. c)  $x$ -displacement at 55  $\mu$ s and d) total-displacement at 13  $\mu$ s.

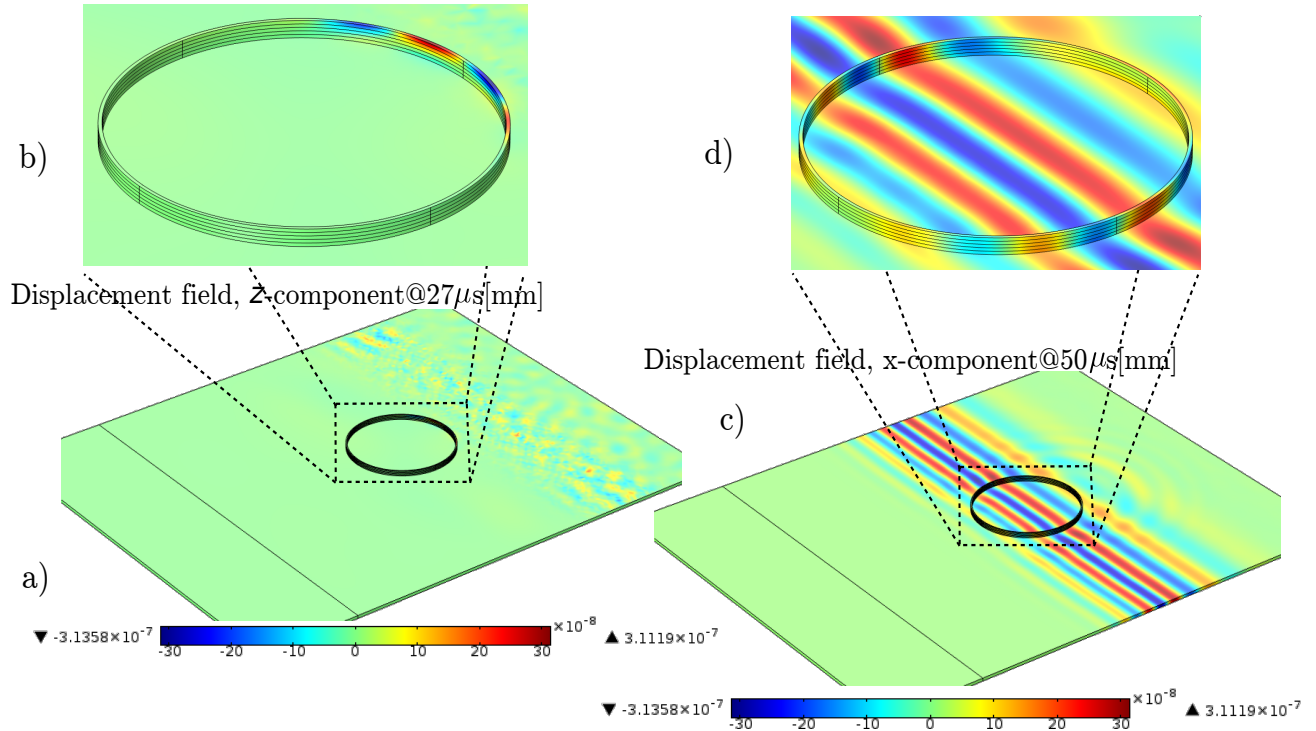


Figure 4.17: Helical fiber coil deformation, from the top and bottom: a) and c) illustrate  $z$ - and  $x$ -component displacement of antisymmetric at 65 kHz mode simulation snapshot, respectively. b) and d) are helical fiber deformation details.

height of the helical wound fiber, as one may infer from Fig. 4.17. The simulation snapshots of  $x$ - and  $z$ -displacement illustrate the disproportional helix coil deformation. Furthermore, the helical transducer impacts the propagating wave in the structures, as expected. Figure 4.18 shows the effect of the helical fiber on the propagating  $A_0$  Lamb wave.

The fiber elongation curves in Fig. 4.19 and 4.20 for respectively  $A_0$  at 10 kHz and  $S_0$  at 100 kHz, prove the sensitivity of the helical transducer of symmetric as well as antisymmetric Lamb waves. The elongation was computed right at the plate (bottom), at half height of the coil (mid) and on top (top). The average characteristic corresponds with the arithmetic mean of the three curves which is approximately proportional to the total length change of the complete helical coil. In case of symmetric excitation, the bottom (blue) elongation shows strong similarity with 5-turn coil fiber elongation in Fig. 4.13. However, the mid and top elongations deviate drastically from this behavior although they feature much larger magnitude. As this combination of plate wave mode and fiber coil configuration leads to severe transduction distortions with respect to the plate strain, it can be used only for tasks like threshold detection. Due to the flexural deformation along the helical fiber height, the fiber elongation varies from the top to down of the helical fiber as shown in the Figs. 4.19 and 4.20. The disparity between the elongation of the top fiber and the plate-coil interface concerns not only on the amplitude. The greater the distance from the plate, the stronger the ringing tail of the signal in response to the short exciting pulse.

In the antisymmetric case and at much lower frequency, the fiber elongation is consistent with the plate structure deformation but with clear difference between the elongation on the bottom and on top fiber ring.

To conclude, the simulations based on orthotropic plates enable the judgment of the

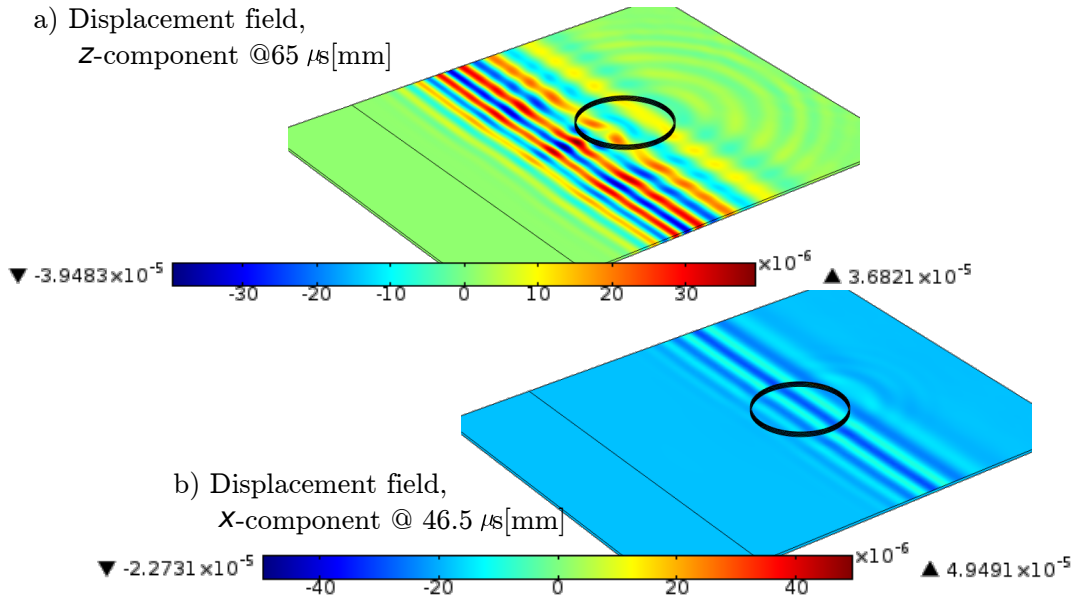


Figure 4.18: Snapshots of the simulated propagation of an  $A_0$  sineburst wave with 65 kHz center frequency. From top to bottom:  $x$ -displacement at 46.5  $\mu\text{s}$  and  $z$ -displacement at 65  $\mu\text{s}$ .

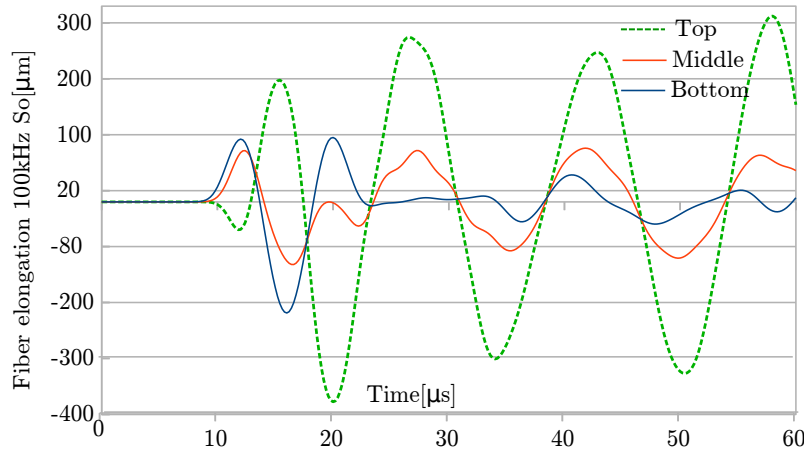


Figure 4.19: Fiber elongation of helical fiber by dominant symmetric  $S_0$  Lamb wave. The measurement have been done at different points of helix height.

transducer fidelity as strain transducer and allow the choice of appropriate transducer forms. The flat spiral coil is best suited as transducer for Lamb wave strain measurements. In general, helical fiber coils are not capable of distortion free strain transduction. They may have some advantage as threshold detectors and perform better in case of flexural plate waves. Therefore, the 5-turn spiral fiber coil is preferably used for sensing in the rest of the following work.

#### 4.1.5 FEM analysis of stratified CFRP plates

The following discussions seeks to extend the modeling work of previous subsections. This section examines the transducer sensitivity by full complexity models of a practical CFRP. It

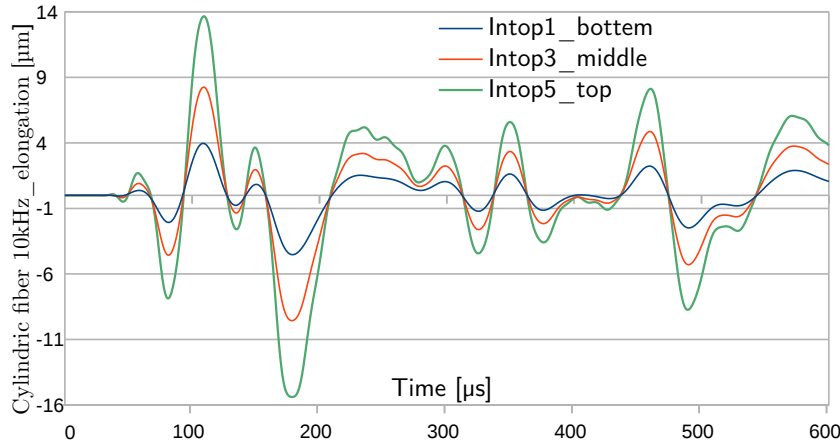


Figure 4.20: Fiber elongation of helical fiber with dominant antisymmetric  $A_0$  Lamb wave.

enables the judgment of the meaningfulness of the approximate orthotropic models. Piezoelectric actuators as well as excitation at the material edge are used for plane quasi Lamb wave sources. Five-turn coil representation of the omnidirectional fiber transducer is employed. The entire system was modeled using the Comsol 4.2 FEA environment.

### Composite modeling in comsol

The individual layers of the composite are assumed to have unidirectional fibers in a matrix and are modeled as being transversely isotropic with uniform density. The modeling have been done as described in subsection 2.4.

The investigated composite CFRP plate has a total thickness  $d = 0.75$  mm, dimensions  $4.5$  cm  $\times$   $12.5$  cm and consists of a stack of 6 plies. The fibers orientations have the directions:  $-45$ ,  $45$ ,  $0$ ,  $90$ ,  $45$ , and  $-45$  degree. All ply in a laminate possess the same thickness of  $0.125$  mm. Due to the different orientations of the reinforcing fibers in the layers, it is useful to describe each layer with a dedicated Cartesian vector base  $(X_1, X_2, X_3)$  distinct from the global coordinate system  $(x, y, z)$  of the model. Figure 4.22 depicts a unidirectional laminate. The  $x$ -axis is aligned with the fiber direction. The fiber cross section lies in the  $X_2$ - $X_3$  plane. In Comsol, the  $X_1$  inclination is given by the projection of the unit vector on the global coordinate system. The direction  $X_3$  is along the thickness of lamina. The orientation of each lamina with respect to the  $x$ -axis is indicated by the angle between the fiber direction and the  $x$ -axis. Positive angles are measured counter-clockwise from the  $x$ -axis when looking toward the lay-up surface.  $E_1 = 135$  GPa  $E_2 = E_3 = 8.55$  GPa,  $G_{12} = G_{13} = 4.2$  GPa,  $G_{23} = G_{32} = 3.5$  GPa,  $\nu_{12} = \nu_{13} = 0.278$ ,  $\nu_{23} = \nu_{32} = 0.352$   $\nu_{21} = \nu_{31} = 0.0176$ . At the lateral sides of the plate, symmetry boundary conditions are imposed which doesn't meet the real behavior exactly. For the simulation, four  $(X_1, X_2, X_3)$  bases were used (Tab. 4.2).

A small piece of material with the same elastic constants but significant damping (Rayleigh damping) was added to the model in order to reduce the influence of waves that have been reflected at the opposite edge, which was kept fixed. The fiber-optic transducer was modeled as before.

For CFRP numerical analysis, two different excitation methods have been used. On one hand, a single sineburst displacement  $s(t)$  according to Eq.4.4 which was imposed to one

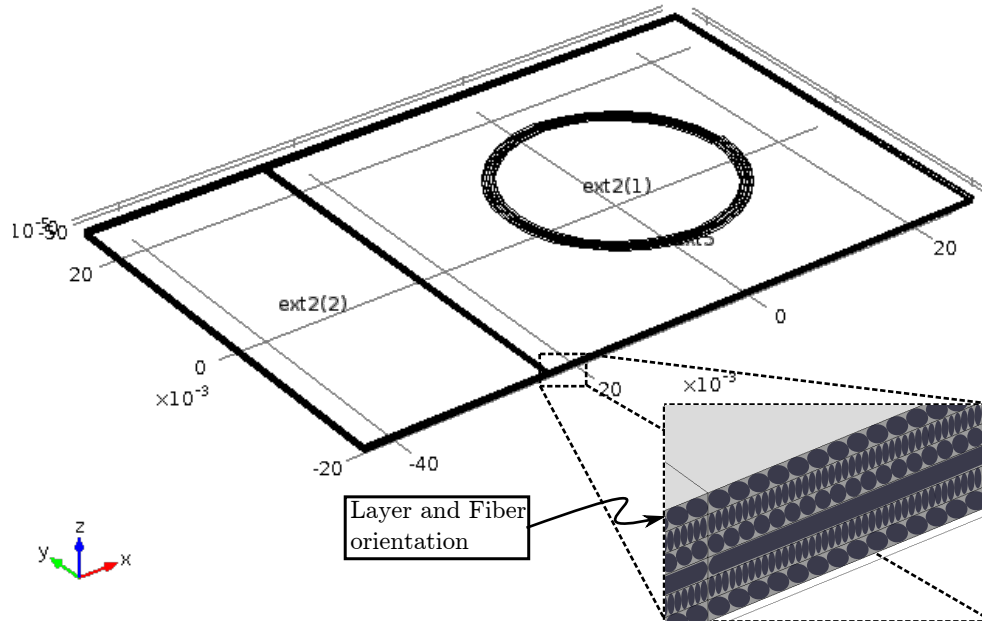


Figure 4.21: CFRP model with transducer; detailed Layer and unidirectional fiber orientation.

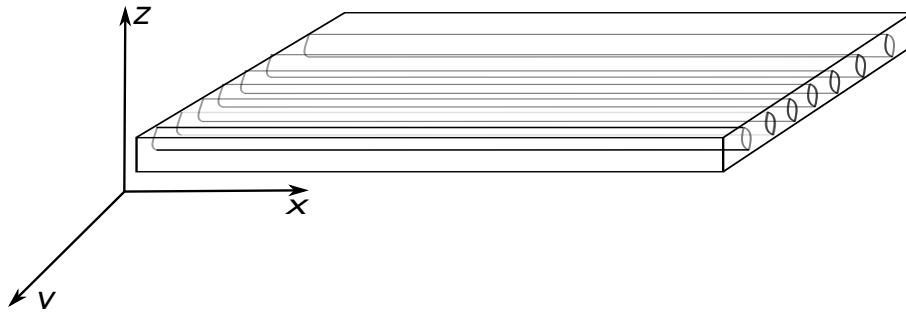


Figure 4.22: Ply with unidirectional fiber with Cartesian vector base.

edge of the plate in  $x$ -direction,

$$s(t) = A \sin(\omega t) \sin^2(\omega t/2), \quad 0 \leq t \leq 2\pi/\omega, \quad (4.4)$$

and on other hand a pair of piezoelectric actuators are applied as described in subsection 2.3 of the chapter 2. Piezoelectric discs of 5 mm diameter and 0.1 mm thickness were used and actuated with a voltage signal according to Eq. 4.5. They were placed on both surfaces of the 6-ply composite plate with coinciding axes. PZT-5A (see characteristic in Tab. 4.3) from COMSOL database was used for this modeling.

### Simulation results for edge face excitation

According to the uniform displacement excitation of an edge face  $x = \text{const.}$ , the main constituent of the packet should be a quasi- $S_0$  wave. The term quasi- $S_0$  indicates that due to the anisotropic layers and their asymmetric sequence, the mode patterns of displacement and stress differ from their respective shape of ordinary  $S_0$  plane Lamb wave and the term fundamental compressional mode seems to be more appropriate. The center frequency of the

Basis	$x$	$y$	$z$
unrotated	1	0	0
Vector base $_90^\circ$	0	1	0
Vector base $_45^\circ$	$\sqrt{2}/2$	$\sqrt{2}/2$	0
Vector base $_{-45^\circ}$	$\sqrt{2}/2$	$-\sqrt{2}/2$	0

Table 4.2: Components in the global coordinate system  $(x, y, z)$  of the unit vector in fiber direction (X1) of the material coordinate system for all rotated-ply layers. Corresponding values for the X2 axis have been omitted and the X3 axis coincides with  $z$  in all cases.

Property	Value	Unit																																				
Density $\rho$	7750	kg/m <sup>3</sup>																																				
Elasticity matrix $C_E$	<table border="1" style="display: inline-table; vertical-align: middle;"> <tbody> <tr><td>120.35</td><td>75.18</td><td>75.09</td><td>0</td><td>0</td><td>0</td></tr> <tr><td>75.19</td><td>120.35</td><td>75.09</td><td>0</td><td>0</td><td>0</td></tr> <tr><td>75.09</td><td>75.09</td><td>110.9</td><td>0</td><td>0</td><td>0</td></tr> <tr><td>0</td><td>0</td><td>0</td><td>21.05</td><td>0</td><td>0</td></tr> <tr><td>0</td><td>0</td><td>0</td><td>0</td><td>21</td><td>0</td></tr> <tr><td>0</td><td>0</td><td>0</td><td>0</td><td>0</td><td>22.57</td></tr> </tbody> </table>	120.35	75.18	75.09	0	0	0	75.19	120.35	75.09	0	0	0	75.09	75.09	110.9	0	0	0	0	0	0	21.05	0	0	0	0	0	0	21	0	0	0	0	0	0	22.57	GPa
120.35	75.18	75.09	0	0	0																																	
75.19	120.35	75.09	0	0	0																																	
75.09	75.09	110.9	0	0	0																																	
0	0	0	21.05	0	0																																	
0	0	0	0	21	0																																	
0	0	0	0	0	22.57																																	
Coupling matrix $d$	<table border="1" style="display: inline-table; vertical-align: middle;"> <tbody> <tr><td>0</td><td>0</td><td>0</td><td>0</td><td>12.29</td><td>0</td></tr> <tr><td>0</td><td>0</td><td>0</td><td>12.29</td><td>0</td><td>0</td></tr> <tr><td>-5.35</td><td>-5.35</td><td>15.78</td><td>0</td><td>0</td><td>0</td></tr> </tbody> </table>	0	0	0	0	12.29	0	0	0	0	12.29	0	0	-5.35	-5.35	15.78	0	0	0	C/m <sup>2</sup>																		
0	0	0	0	12.29	0																																	
0	0	0	12.29	0	0																																	
-5.35	-5.35	15.78	0	0	0																																	
Relative permittivity $\epsilon_{rs}$	<table border="1" style="display: inline-table; vertical-align: middle;"> <tbody> <tr><td>919.1</td><td>0</td><td>0</td></tr> <tr><td>0</td><td>919.1</td><td>0</td></tr> <tr><td>0</td><td>0</td><td>826.6</td></tr> </tbody> </table>	919.1	0	0	0	919.1	0	0	0	826.6	1																											
919.1	0	0																																				
0	919.1	0																																				
0	0	826.6																																				
Poisson's ratio	0.31	1																																				

Table 4.3: Piezoelectric actuator characteristics (PZT-5A).

excitation was chosen low enough to enable exclusively the fundamental compressional mode which propagates in the  $-x$ -direction. As can be seen from Fig. 4.23, the propagating wavefronts are not uniform. The reinforcing fiber orientation in each ply influences the preferred direction of wave propagation. Figure 4.23 depicts snapshots of the simulated propagation of a dominant symmetric Lamb wave packet where the colors scale the displacement in  $x$ - and  $y$ -direction. The mode pattern signals nonuniform wave propagation in the  $x$ -direction where the orientation of the carbon fibers in the top and bottom layer, i.e.,  $-45^\circ$ , seems to be distinguished. The deformation happens preferably perpendicular to that direction, which is the direction with the lower in-plane elastic modulus of the top and bottom layer. Also the side face with  $y > 0$  exhibits higher intensity than the opposite face. It can be suspected that the elastic energy proceeds preferably along the fibers in the outmost layers. In addition, reflections of the wave occur at the side faces  $y = const.$  in spite of the symmetry condition there. This is a consequence of the inclined fibers that are mirrored rather than prolonged beyond the model border, which means that symmetric boundary condition means no simple continuation of the material.

Furthermore, corresponding simulations have been performed but for an edge displacement excitation parallel to the  $z$ -axis, which then preferably excites flexural antisymmetric wave modes. Figure 4.24 shows snapshots of the simulated propagation of a dominant antisymmetric Lamb wave packet where the colors scale the displacement in  $z$ - and  $y$ -direction, respectively. Interestingly, the propagating wavefront were parallel until the first boundary

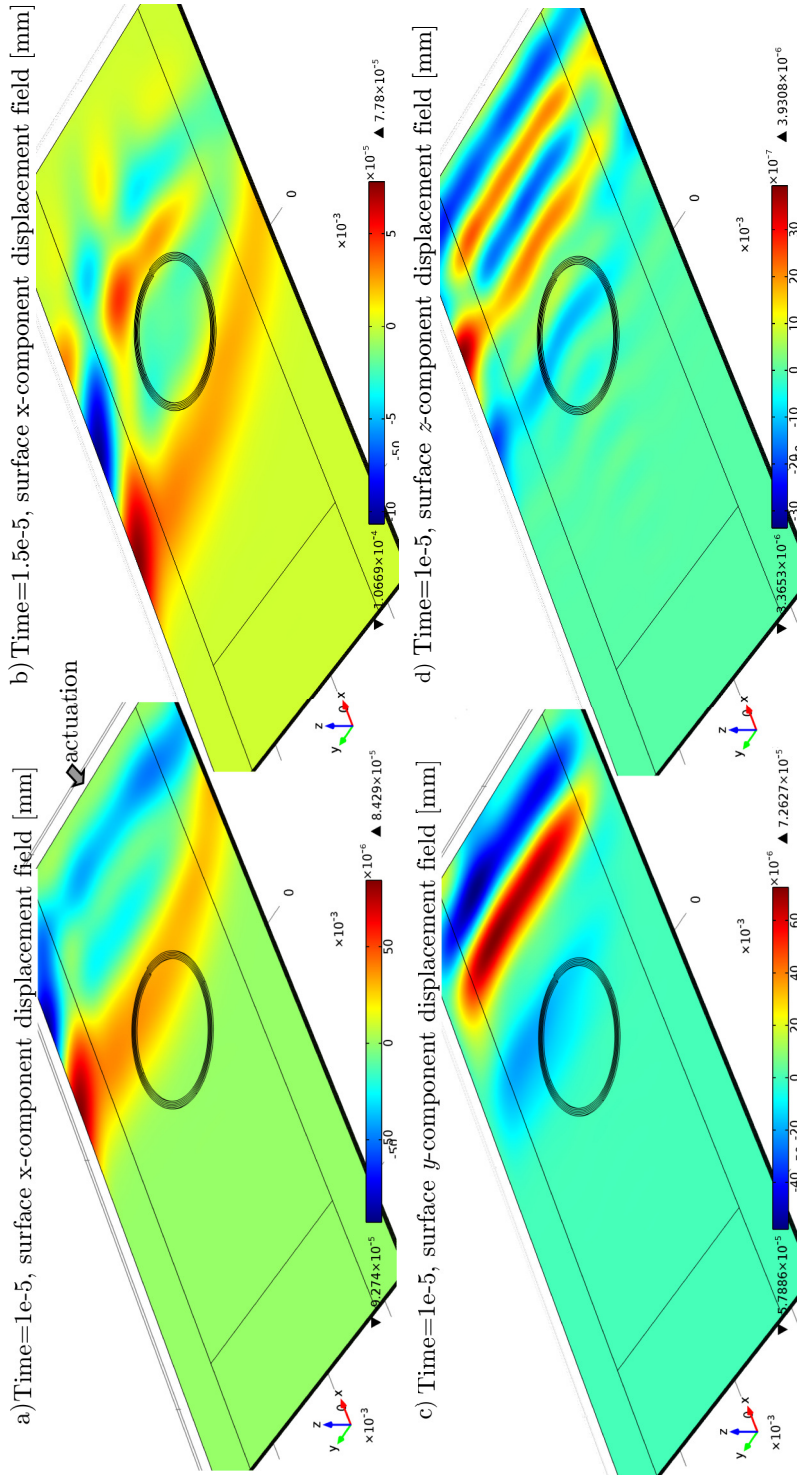


Figure 4.23: Snapshot of compressive Lamb wave that are generated at the an edge face edge of the 6 plies composite laminate. a) and b) illustrate  $x$ -component of displacement for 10 and 15  $\mu s$  elapsed time, respectively. At 15  $\mu s$ , the displacement of  $y$ - and  $z$ -component, by c) and d) respectively.

reflection occurs. However, inspection of other components of the displacement indicates slight reflections by the attached fiber.

The fiber elongation curves in Fig. 4.25, collect in both cases from the deformation of the plate surface, proves the sensitivity of the transducer by symmetric as well as antisymmetric plate waves.

### CFRP with piezoelectric actuator results

In this subsection, the previous plate model is used together with a pair of piezoelectric actuators for elastic wave production and a flat spiral fiber-optic transducer. The local deformations underneath the affixed optical waveguide, generated by the piezoelectric actuators are relevant to the fiber-optic transducer. Dominant antisymmetric as well as symmetric elastic waves are generated in the 6-ply plate depending on the relative electrical phase of the actuation voltages. In both cases, the circular wavefront is quickly reflected close by boundaries. The flexural plate displacement taken at the two points shown in Fig. 4.26 is depicted in Fig. 4.27 and correspond exactly to the used single-sine burst excitation signal applied to the piezoelectric actuators.

The elongations of the transducer fiber for antisymmetric excitation is shown in Fig. 4.28. This result confirms that the plies orientation has less influence on the fiber elongation by antisymmetric excitation. This elongation agrees well with the recorded displacement in Fig. 4.27.

Figure 4.29 represents a simulation snapshots of a piezoelectric actuated CFRP. Parallel poling direction are applied to the piezoelectric actuator, producing dominant symmetric waves. Contrary to the edge excitation of  $S_0$  in the previous section, the fiber orientation in CFRP have less influence of the propagating waves. The fiber elongation illustrated in Fig. 4.30, is equivalent to the strain signal.

In conclusion, the edge excitation allow to proportional some simulation's times but is not optimal for CFRP excitation.

## 4.2 Robust strain transducer

The fiber-optic sensing element is hard to handle in harsh environment. Furthermore, the interferometric signal suffers from nonuniform temperature variations of the environment of both the measurement and the reference arm. The fiber-optic transducer analyzed in the previous sections, is now modeled with appropriate support material for getting a robust and eventually reusable strain transducer. The construction of the fiber interferometer is such that unwanted interferences are reduced to a minimum. The 5-turn spiral coiled fiber sections are fixed to L-shaped supports, which supposedly protect the fragile fibers. The fiber coils (sensing and the reference parts) are now positioned face to face with a mm sized gap in between. The gap is filled with soft a silicone elastomer to achieve a uniform thermal conditions but acoustic decoupling between measurement and reference coil. In this subsection, numerical modeling of this robust transducer is presented for different supporting materials.

Since the experiment is done with the available 16-ply composite the model approximates this arrangement. However, the numerical analysis are performed for an orthotropic plate in lieu of the 16 layered composite structure. A pair of piezoelectric actuators is applied to enable the generation of symmetric and antisymmetric elastic waves.

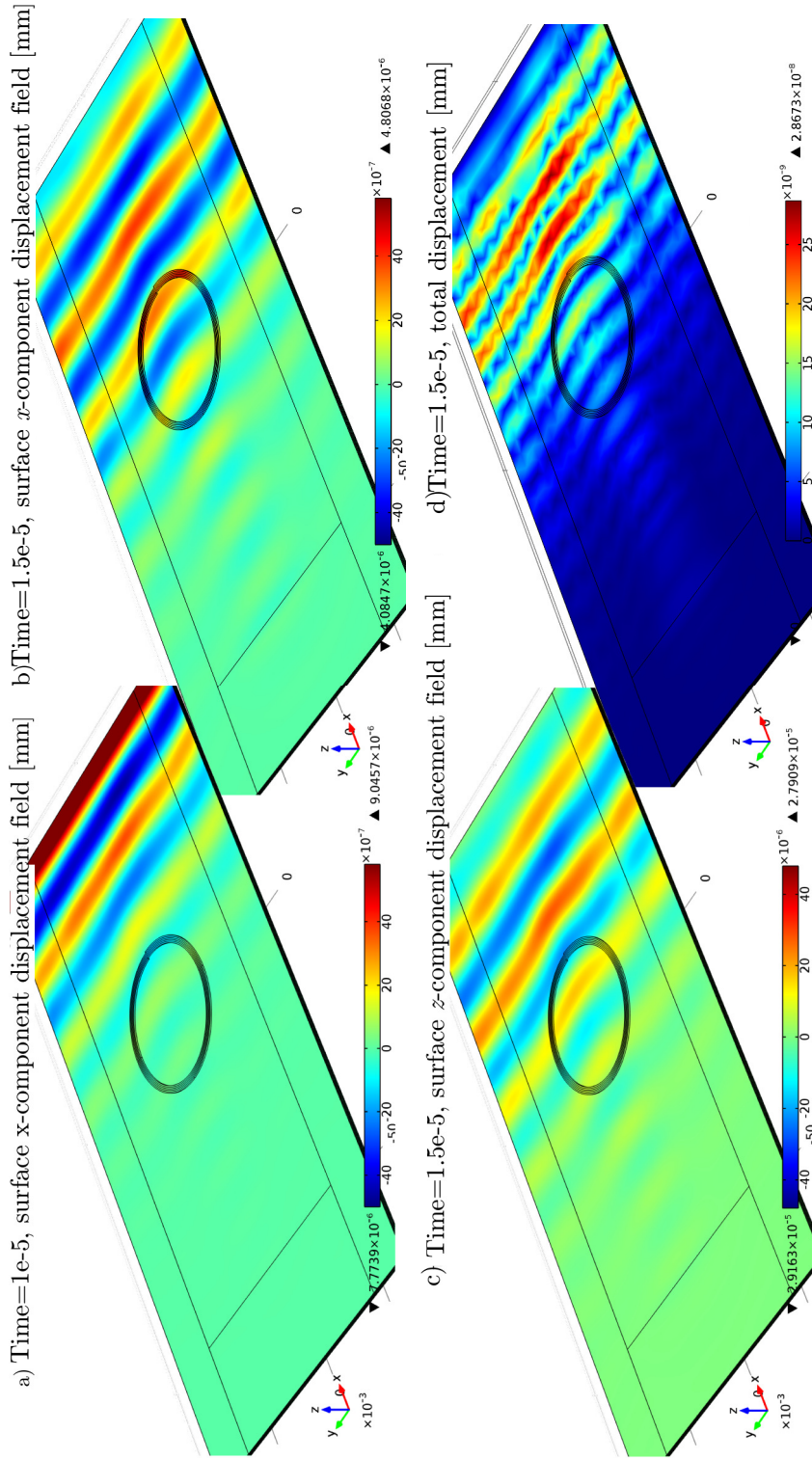


Figure 4.24: Snapshot of antisymmetric Lamb wave that are generated at the edge of a 6 plies composite laminate. Displacement at 15  $\mu$ s  $x$ ,  $y$  and  $z$  component in a), b) and c) respectively. d) depicts the total displacement at 15  $\mu$ s.

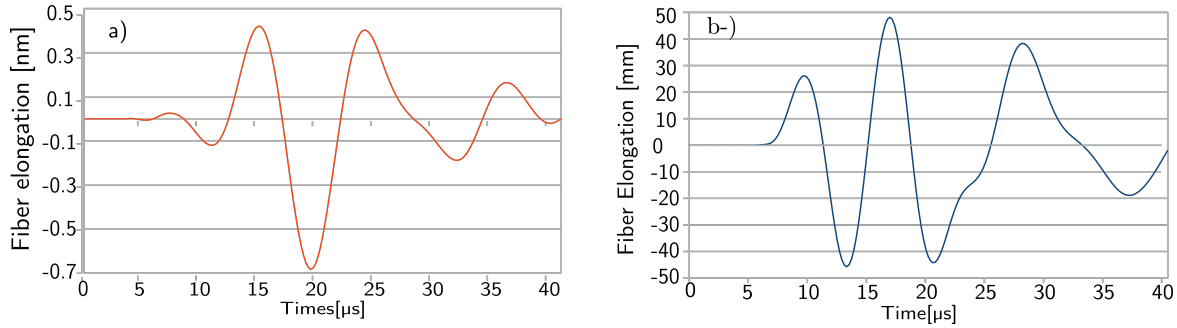


Figure 4.25: Fiber elongation curve of 5-turn coil on CFRP excited at edge; a) dominant antisymmetric and b) symmetric mode.

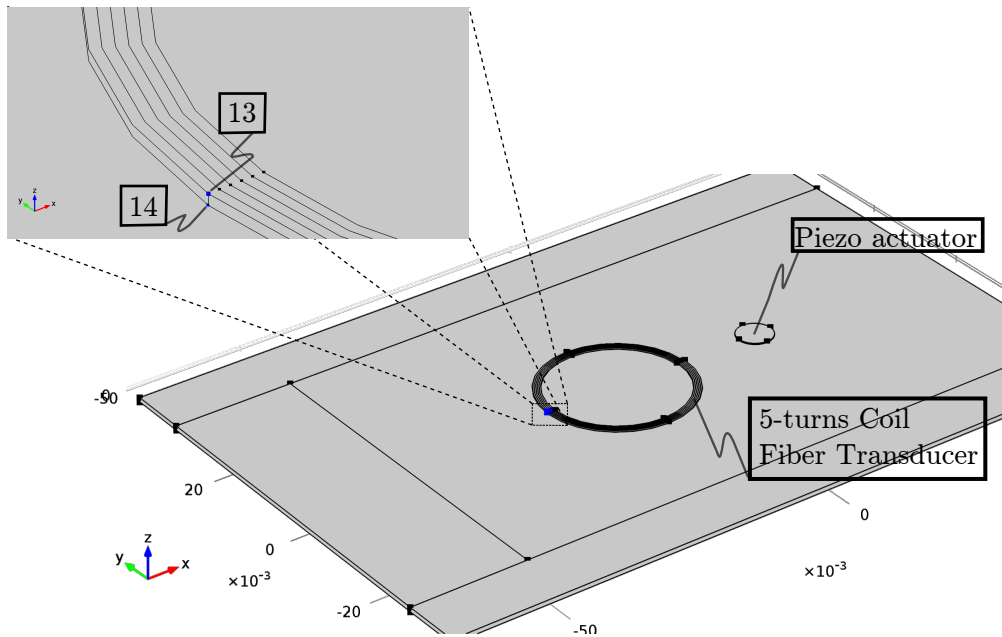


Figure 4.26: Recording positions for simulated displacement, fiber and piezoelectric actuators on the plate, 13 and 14 are the measurement points ,

### 4.2.1 Model of the robust transducer

For the examination of its sensitivity a finite element model is applied to simulate the embedded fiber coil in stainless steel ( $E=190$  GPa,  $\rho=7930$  kg/m<sup>3</sup> and  $\nu=0.3$ ) as well as in polyimide. The detection system is attached on the composite plate which is supplied with transient elastic waves coming from the pair of piezoelectric actuators. The simulated device is a 40 cm×20 cm orthotropic plate (same parameters as in previous sections) with a total thickness  $d=5$  mm. The piezoelectric actuators are placed of the plate at 5 cm distance from the fiber-optic transducer and a voltage  $V(t)$  according to 4.5 is applied to them.

$$V(t) = 100 \sin(\omega t) \cdot \sin^2\left(\omega \frac{t}{2}\right), \quad \text{with } 0 < t < 1/f. \quad (4.5)$$

Figure 4.31 shows the main components of the robust transducer prior to the final assembling. The material parameters of intermediate silicone elastomer between the carriers and polyimide support are taken from the Comsol material browser.

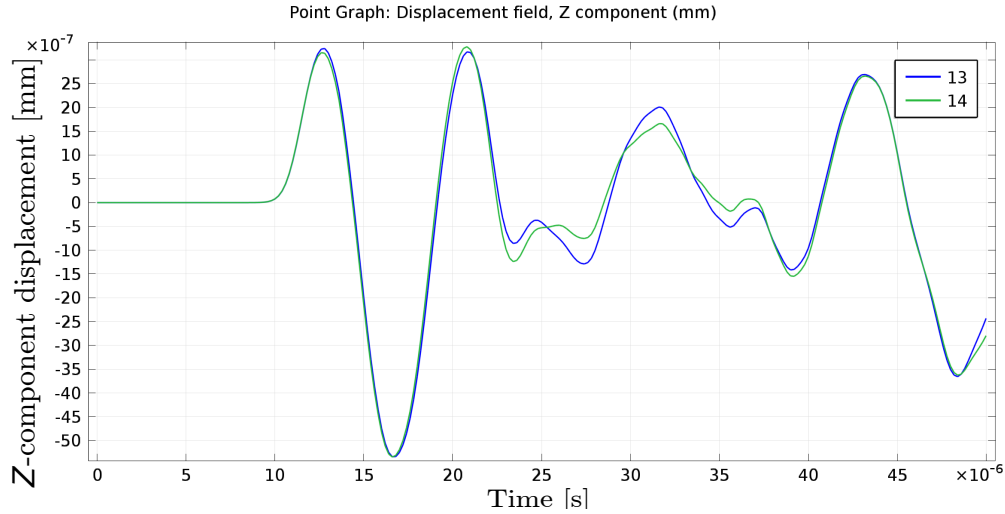


Figure 4.27: Z-displacement recorded by a fixed fiber transducer for dominant  $A_0$  excitation at 65 kHz and 100 V excitation.

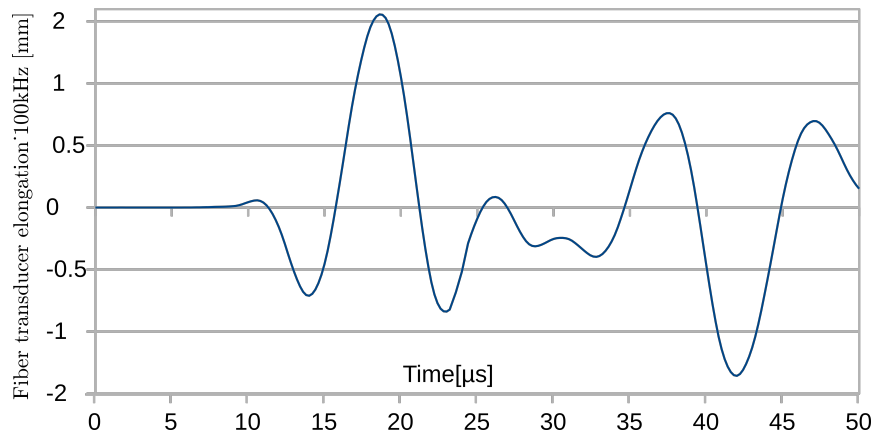


Figure 4.28: Fiber elongation by CFRP actuated with piezoelectric actuator, antisymmetric at 65 kHz.

The applied electrical fields are chosen for synchronous deformation of both actuators in case of symmetric excitation and antiphase deformation for antisymmetric elastic wave generation. The main constituent of the packet should then be a compressional or flexural elastic wave according to whether symmetric or antisymmetric production featuring a typical propagation velocity of roughly 5000 m/s or 1500 m/s, respectively. The center frequency of the excitation was chosen low enough to prefer the fundamental  $A_0$  (25 kHz) or  $S_0$  (100 kHz) mode.

## 4.2.2 Simulation results for robust transducer

A fiber elongation curve for antisymmetric excitation, illustrated in Fig. 4.32, proves the feasibility of the robust transducer. The pair of piezoelectric actuators is supplied antisymmetrically and is excited with a voltage single-sine burst signal from the Eq. 4.5 with 25 kHz center frequency and an amplitude voltage of 100 V. The elongation curve of the reference coil is nearly zero. A comparison of the fiber elongation of the dominant antisymmetric case, signal reveals that the robust sensor is strain transducer and that the propagation

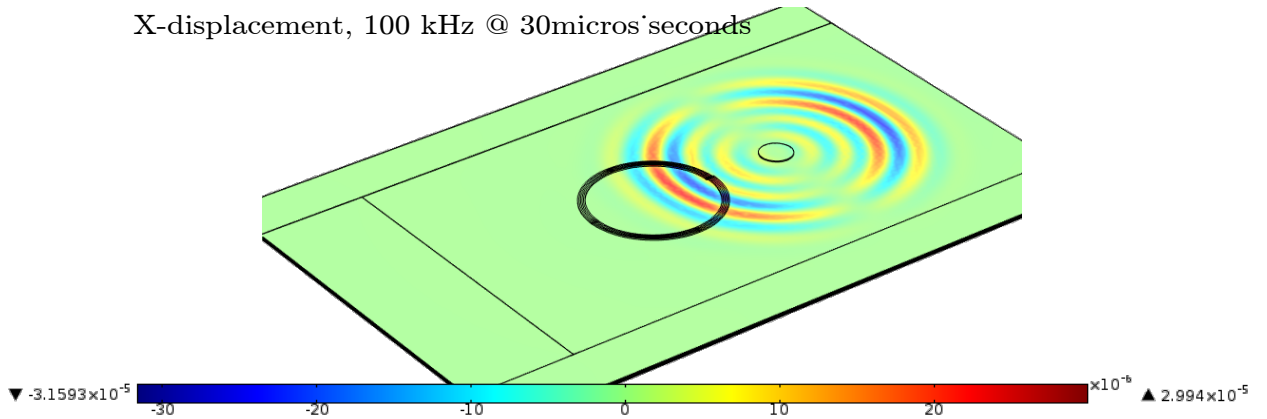


Figure 4.29: Snapshots of plate waves in a 6-ply CFRP actuated piezoelectrically with 100 kHz symmetric wave at 100 V.

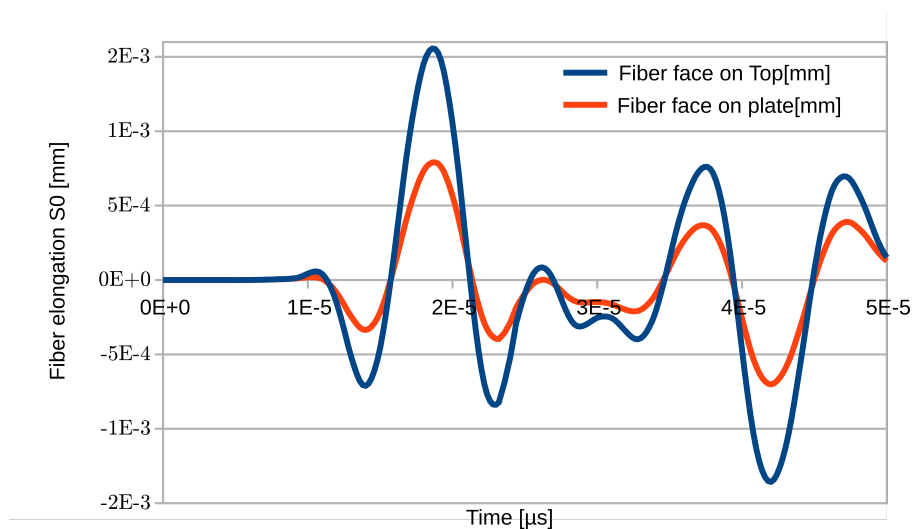


Figure 4.30: Fiber elongation by CFRP actuated with piezoelectric, symmetric, single-sine burst at 100 kHz and 100 V.

delay from the piezoelectric actuator to the coil center agrees with an ultrasound velocity of 1500 m/s. Figure 4.33 details the time course of the fiber elongation for at center frequencies of 100 kHz for symmetric elastic waves. Figure 4.34 shows snapshot of the symmetric simulated propagation of an elastic wave packet. The pattern indicates reflections by the attached transducer and at plate boundary. In addition, mode conversion from antisymmetric modes to symmetric mode has to be expected as the attached sampler brake the symmetry of the plate.

The FEA of the propagation of Lamb wave packets in plates of orthotropic material that bear the carrier of a robust sensor spiral coil of an optical fiber was successfully performed. The chosen simulation setup is well suited to study propagation and the transduction characteristics of elastic plate waves with the computing power of standard PCs. The temporal change of the fiber length for the spiral coil prove the sufficient sensitivity of the novel transducer. The attached robust sensor causes only moderate distortions of propagating elastic waves packets. The proposed transducer features a compact packaging of the interferometer arms enabling high immunity against environmental influences like temperature variations.

Finally, the configuration used for the transducer experiments was modeled. The plate

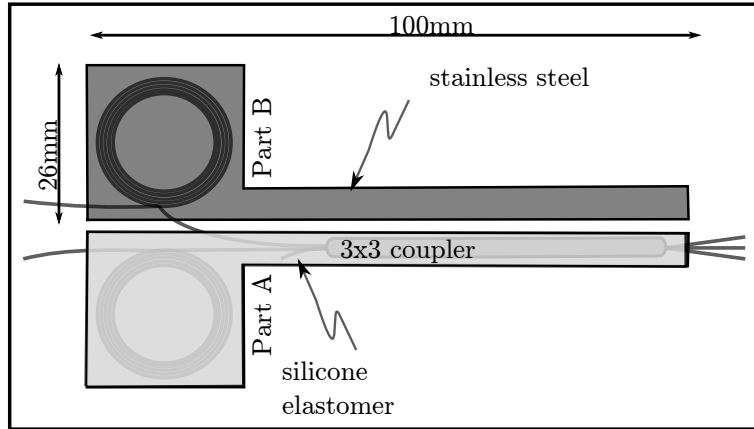


Figure 4.31: Schematic of the simulation model for the robust fiber optic transducer.

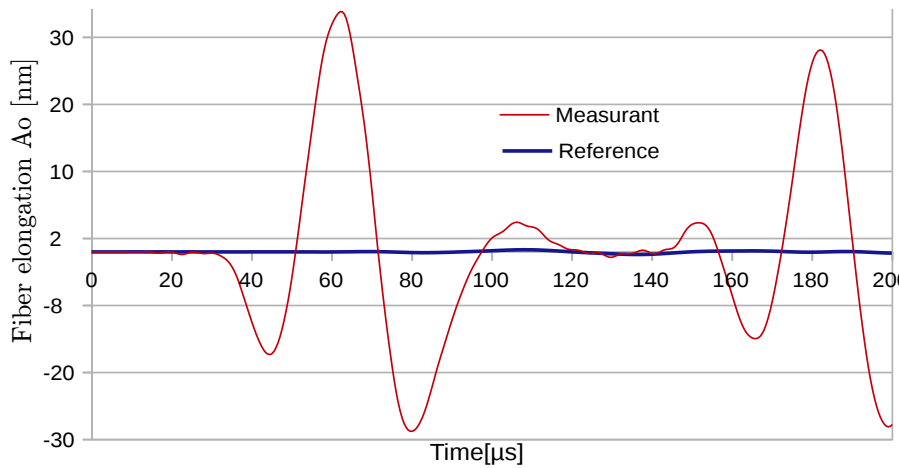


Figure 4.32: Fiber elongation by excitation with antisymmetric  $A_0$ , with 25 kHz center frequency at 100 V.

dimensions are 400 mm  $\times$  80 mm  $\times$  5 mm, four piezoelectric actuators are positioned symmetrically 1 cm and 4 cm near the corners of the plate. The center of the robust transducer fiber coils is situated at 152 mm in x, and 37 mm  $y$  directions. The active actuator is powered with a single-sine voltage burst of 100 V magnitude and 10 kHz nominal frequency. Figures 4.36 and 4.37 show the fiber length responses of the measurement and reference fibers for the actuation with piezoelectric actuator 1 and actuator 3, respectively.

The curves traces of Figs 4.36 and 4.37 are typical of practical measurements of plate waves. The complex signals indicate the simultaneous excitation of fundamental flexural and fundamental compressional modes and multiple reflections at the plate boundaries. Because of its complex nature, the shown responses cannot be analyzed in terms of flexural or compressional waves. Therefore, practical systems for SHM should always employ the deviations of the measured response with respect to a reference measurement on the same plate object.

### 4.3 Summary

The strict mathematical analysis of elastic waves in inhomogeneous and anisotropic composite material is extremely difficult to accomplish. The motion equations become intractable

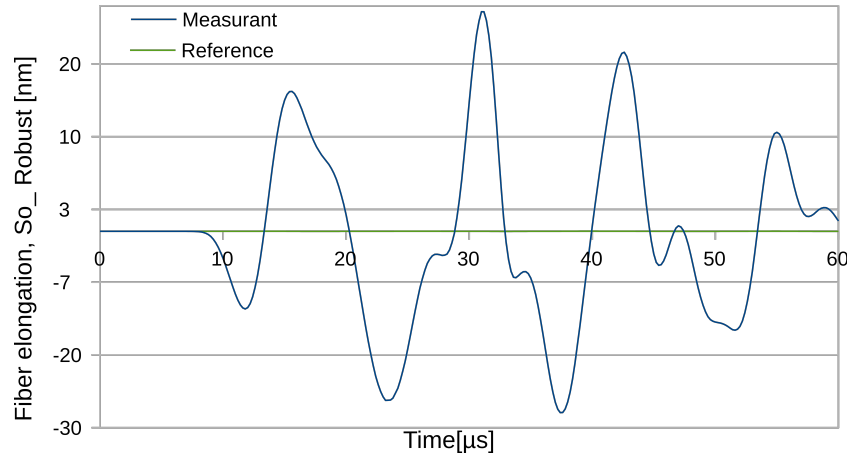


Figure 4.33: Fiber elongation by dominant  $S_0$ , 100 kHz center frequency at 100 V.

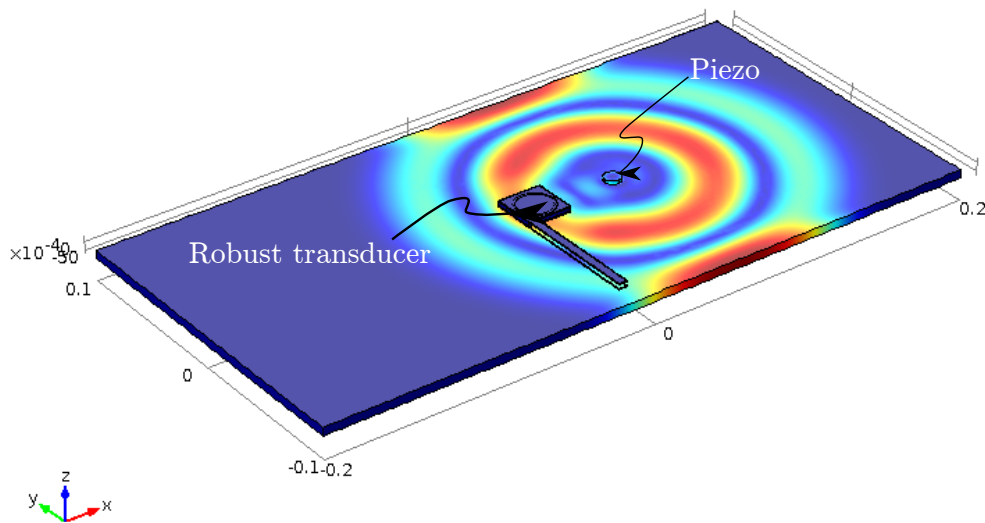


Figure 4.34: Snapshot at  $40 \mu\text{s}$  of the simulated total displacement of a symmetric plate wave. Excitation parameters are single-sine burst wave with 100 kHz center frequency, Voltage 100 V.

for complicated geometries or for non-homogeneous materials such composites. Therefore, numerical simulations with finite element method for example are more appropriate to tackle such problems.

The mechanical response to plate wave induced strain of a circular fiber attached to the investigated plate was studied with FE analyses. The fiber coil forms the measurement arm of an interferometer to enable a high sensitivity against plate deformations. The transducer response is derived from the changes of the computed length of the spiral coil. A comparison of two different transducer designs (5 and 10 turns) reveals that the loading of the plate by the spiral coil fiber has no significant influence on the transducer efficiency.

Directly mounted fiber-optic transducers have been simulated for the homogeneous and isotropic aluminum specimen, for an orthotropic CFRP replacement material, and a fully featured 6-ply plate.

An artificial orthotropic material was used with computational advantage for the comparison of two different transducer designs (5 and 10 turns). Furthermore, the small loading

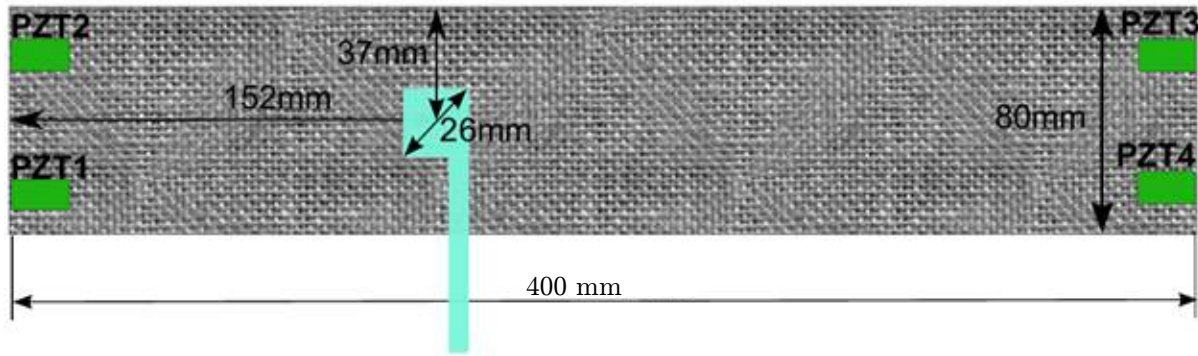


Figure 4.35: Setup of the robust sensor and the four piezoelectric actuators on the composite plate.

effects by the bare fiber-optic transducer as well as the impacts of the robust fiber-optic transducer studied within this frame. However, simulations using the orthotropic CFRP replacement material don't yield accurate results with respect to the peculiarities of plate wave propagation in strongly anisotropic stratified materials.

Simulations for homogeneous and orthotropic plates were performed with a modern desktop PC equipped with 16 GB RAM. Typical computation times for a transient simulation of 500 time steps range up to 3000 seconds for normal-resolution meshes. For all simulations with the full complexity of CFRP material a workstation with memory of 32 GB and swap of 16 GB was used.

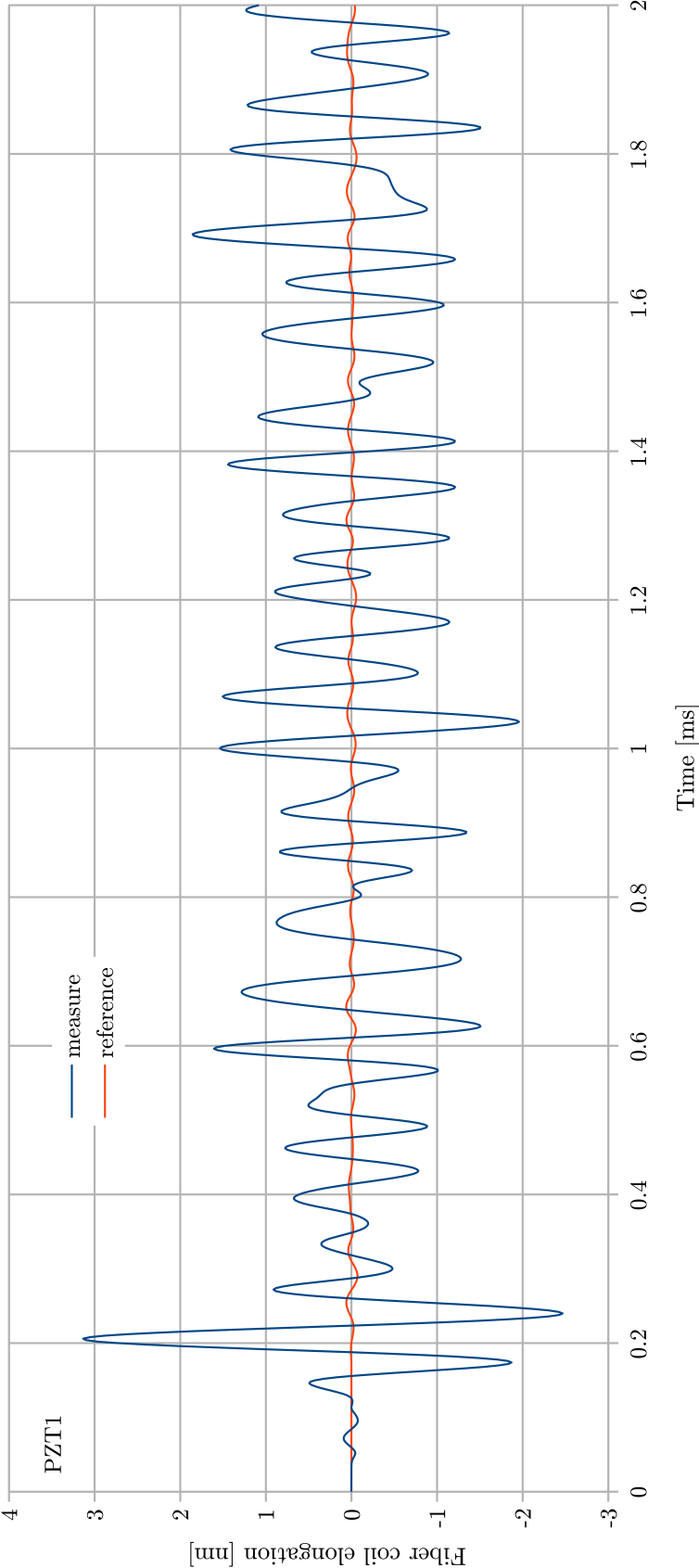


Figure 4.36: Fiber elongation in response to a single-sine burst activation (10 kHz, at 100 V) of actuator PZT\_1 in Fig. 4.35.

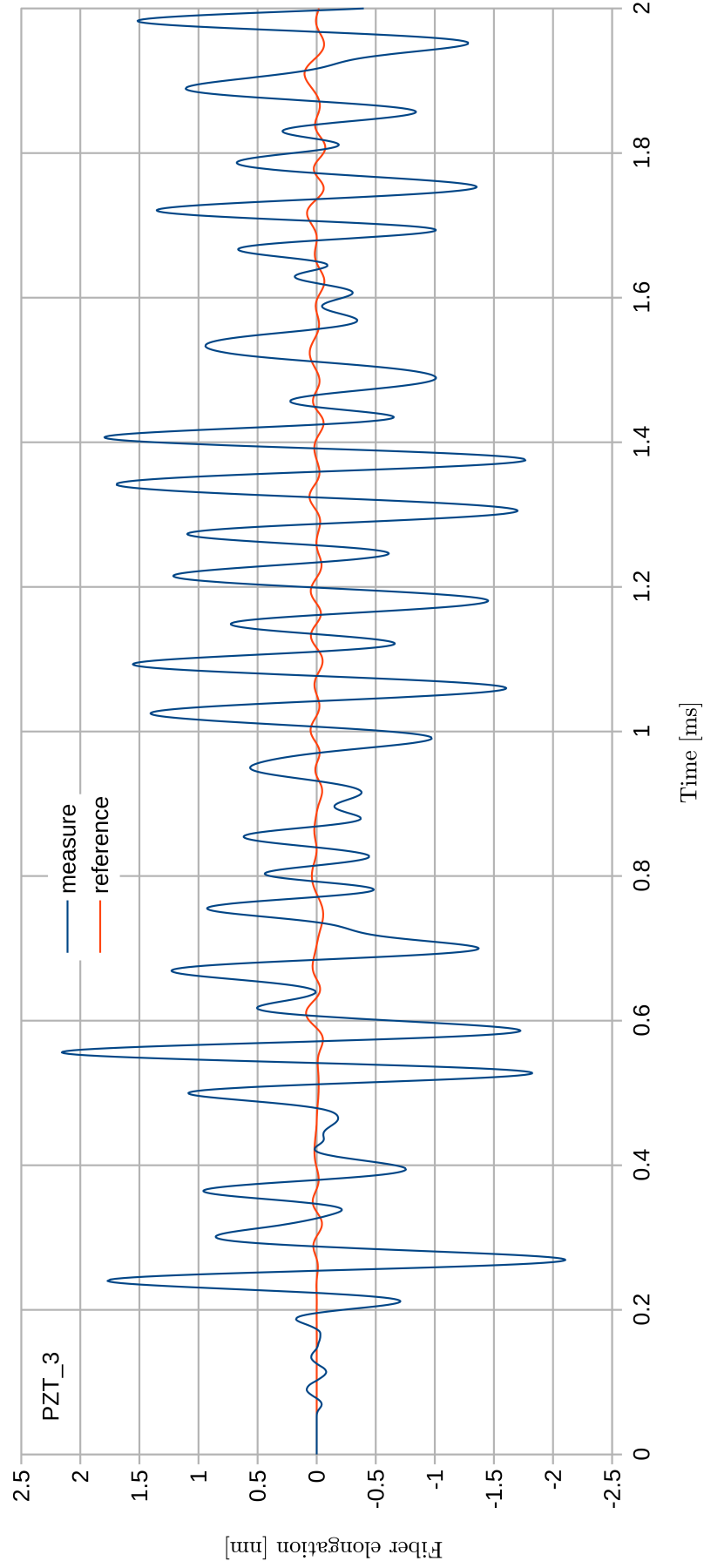


Figure 4.37: Fiber elongation in response to a single-sine burst activation (10 kHz, 100 V) of actuator PZT\_3 in Fig. 4.35.

# Chapter 5

## Experimental investigations

To confirm the analytical and numerical modeling results presented in the previous chapters, two distinct implementations of fiber-optic transducers combined with elastic wave actuators and suitable plate geometries were designed, built, and experimentally investigated.

First, a bare circular fiber-optic transducer was affixed concentrically around a piezoelectric disc on a homogeneous circular plate. This setup enables the experimental characterization of the pulse transfer over the complete transduction chain and thus a direct comparison with related outcomes of numerical simulations.

Second, a pair of equal fiber coils mounted on a stainless steel supporting carrier each and fixed face-to-face with soft silicone in between, were employed as an implementation of the robust and reusable transducer. This device was firmly attached to a 5 mm thick CFRP plate equipped with several commercial piezoelectric guided wave actuators. This setup serves for the experimental verification of the robust fiber-optic strain transducer concept.

This chapter covers all aspects of the experimental procedure. After a brief description of the experimental setups and the description of their components, the symmetric and antisymmetric wave generation with piezoelectric actuator is explained. Then, sensitivity and efficiency of the omnidirectional and novel robust transducer are measured. Finally, an overview of the different plates used in the experiments is given and the verification of fiber-optic transduction method is developed. All experiments were performed at room temperature.

### 5.1 General instrumentation

The experiments were made with specific implementations of the system depicted in Fig. 5.1. All experiments made use of the same optoelectronic modules and electronic instrumentation. The experiments mainly differ in the way of position of the piezoelectric actuation as well as in the design of the fiber-optic component for the detection of guided elastic waves.

The low coherence light source (LCS, Superlum SLD-561-HP2-DIL-SM, wavelength: 1310 nm) was operated with controlled current and over temperature protection using a stabilized power supply (Superlum, Pilot 4/AC). To allow the transmission of produced light in only one direction, dual stage optical isolator OI (S/N\_ 60001971), P grade, 1310 nm wavelength, SMF from Opneti communication company is placed between the LCS and the following coupler. The 3×3 coupler 00928517 from JDSU company, the coupler branches were single mode corning 28<sup>e+</sup> fiber (SMF) with 9/125/250 μm in core/cladding/coating diameter, respectively. The extended fiber is used for the transducer manufacturing. The pulse shapes for the excitation of the piezoelectric actuator, comprising Morlet and sineburst

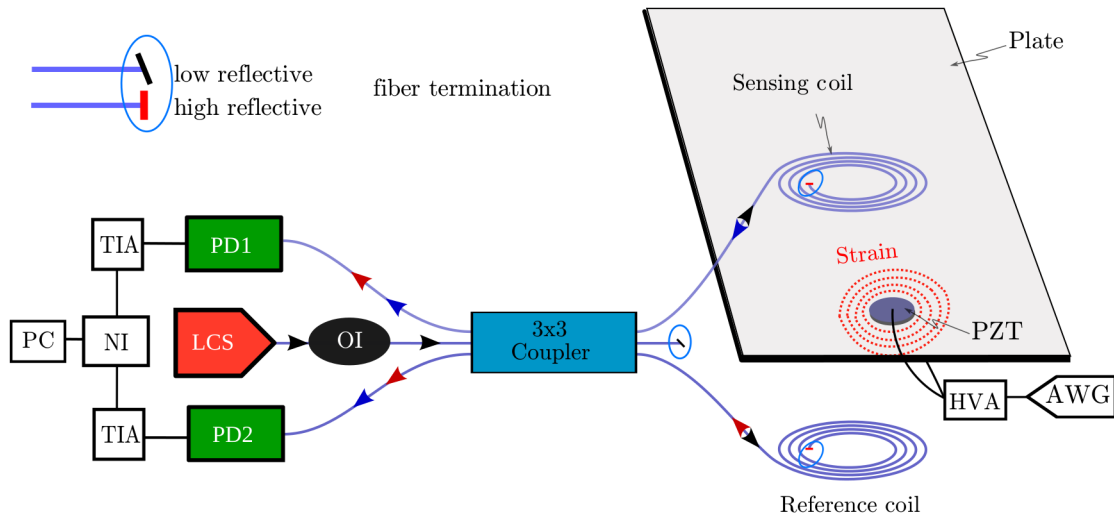


Figure 5.1: System overview of the experimental setup. The Sensing and reference coils are only representative for the measurement and reference arm of the interferometer.

(single, 3 and 5-cycle bursts) pulses, were defined by either an arbitrary waveform generator (AWG, Tektronix AFG3252 or a function generator Stanford Research Systems DS345, with a maximum frequency for sine wave of 30 MHz). The output of these generators were input into a high voltage amplifier (HVA, New Focus Model 3211) that enables peak voltages up to  $\pm 200$  V. The amplifier output was then supplied to the different piezoelectric actuators introducing elastic waves.

On the detection side, a pair of InGaAs photodiodes (PD1, PD2 of type PF-series from Roithner Laser Technik GmbH) were used to convert the interferometer output intensities into electrical currents. The diode currents were amplified and converted into voltage signals with transimpedance amplifiers (TIA, custom made bandwidth 1.5 MHz, conversion gain 9 V/A). Their output signals were directly fed into a data acquisition module (NI, National Instruments NI-USB-6225) and both channels were sequentially digitized with 500 kHz sample rate per channel and 16 bit resolution. The data streams were collected with a PC for later evaluation. The data processing and numerical analyses were performed offline using custom routines written in Python.

## Guided elastic wave actuation and detection

The piezoelectric actuators element should be displaced far enough from all plate boundaries to avoid quick reflections (see Fig. 5.2). The employed piezoelectric actuators are polarized in parallel with the piezoelectric disc axis. The shown example features antiparallel polarization orientation so that is one signal applied between their contacts and the grounded plate cause the thickness and radius of the disc to contract or expand in phase. Due to the adherent plate, however, the piezoelectric actuator experiences a more complex deformation pattern. Then, the dynamic actuator deformation creates a symmetric elastic wave within the plate material that propagates through the plate and eventually strains the fiber-optic sensor. Both symmetric and antisymmetric elastic wave modes can be produced from the circuit shown in Fig. 5.2 playing around with symmetrically and antisymmetrically polarized actuators and in-phase or opposite phase actuation voltages. Depending on the mode to be produced, the appropriate frequencies range between 10 and 300 kHz.

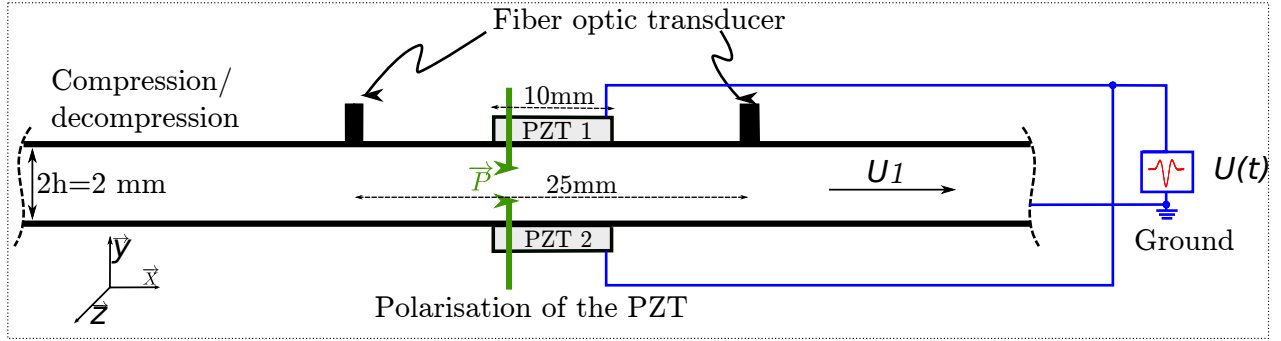


Figure 5.2: Schematic of measurement setup with piezoelectric actuator fixed to the plate: Two PZT discs were used in pair to generate dominant symmetric guided waves in the plate.

## 5.2 Reference model implementation

The purpose of the first series of experiments was to verify the presumed physical models of piezoelectric actuation of elastic waves, their propagation and conversion with intrinsic fiber-optic transducers in all details. Design guidelines for the implementation and the resulting dimensions of the aluminum plate as waveguide are described in section 4.1.2 in conjunction with the modeling of the reference experiment.

The main scope of design was to use only components that enable a well defined description of their transduction effect. Accordingly, piezoelectric disc actuators made of PIC255 piezoelectric ceramics (PI Ceramics GmbH) polarized in parallel with the disc axis (3-axis) and uniform electrodes at the circular faces were selected to ensure a nearly homogeneous electric actuation field. This arrangement permits uniform deformation of the piezoelectric disc in response to the applied field and ensures that guided waves are excited primarily through radially symmetric deformations via the transverse piezoelectric coupling coefficient  $d_{31}$ . To be conform with the simulations, one piezoelectric disc actuator was centrally attached on each surface of the circular plate and the other one in the opposite face. They were fixed to the plate using silver-filled conductive epoxy resin (Epotek H20E-LV). The twin actuator arrangement enables the specific excitation of symmetric and antisymmetric guided elastic waves. The relative polarization orientation of the piezoelectric discs was anti-parallel, which means corresponding electrodes adhered to the aluminum plate. The aluminum plate is connected to ground with an alligator clip fastened at the circumference (see Fig. 5.3 a). It serves as electrically conductive path needed to impose the defined electric field to the piezoelectric actuators. To reduce the influence of the mechanical support of the plate a foam rubber mat was positioned between plate and table as shown in Fig. 5.3.

The arbitrary waveform generator produces a wavelet signal according to Eq. 4.2 with typically amplitude of  $U_0 = 40$  V and frequency  $f = 100$  kHz and feeds it into the high voltage amplifier which is connected to the piezoelectric actuators. However, the time variable  $t$  in this equation refers to the center of the pulse rather than the trigger moment of the generator. This signal was supplied to each piezoelectric disc. Because of the selected polarization orientation of the actuators, they must be connected in parallel to the amplifier output to achieve symmetric actuation. For the applied frequency range, the variation of the radial displacement at the transducer-plate interface can be expected in proportion to the voltage  $U(t)$  applied to the electrodes.

Light from the LCD is distributed to the interferometer arms with the help of an  $3 \times 3$  fiber-optic directional coupler. Reflected light from both interferometer arms (“Meas” and

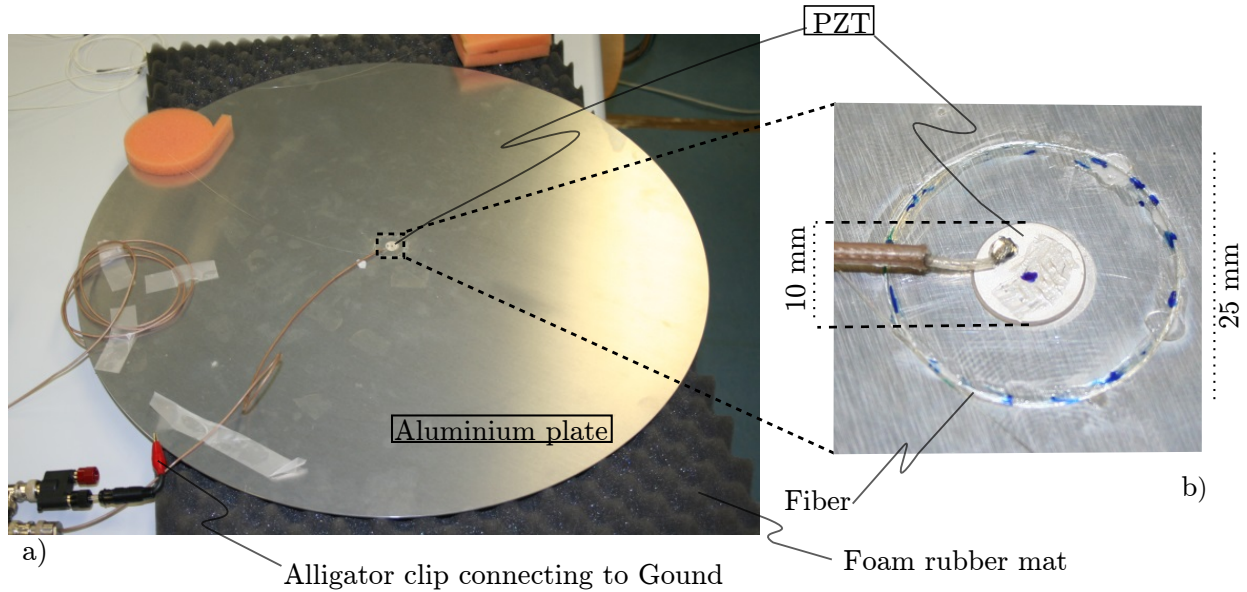


Figure 5.3: Fixed piezoelectric actuator surrounded by the circular measurement path of the fiber-optic transducer on the aluminum plate. a) Aluminium plate with all connection, piezoelectric and fiber; b) Zoom in on the aluminium plate center with fiber and piezoelectric actuator.

“Ref”) is guided to PD1 as well as PD2. The implemented measurement arm comprises a circular bent fiber segment that is fixed to the aluminum plate with cyanoacrylate adhesive (Loctite 401) while the straight reference arm was loosely resting on the table. Both arms consist of extended single mode fibers of the directional coupler. The transducer section of the measurement arm formed a circle of 25 mm diameter.

A schematic overview of the experimental configuration is shown in Fig. 5.4.

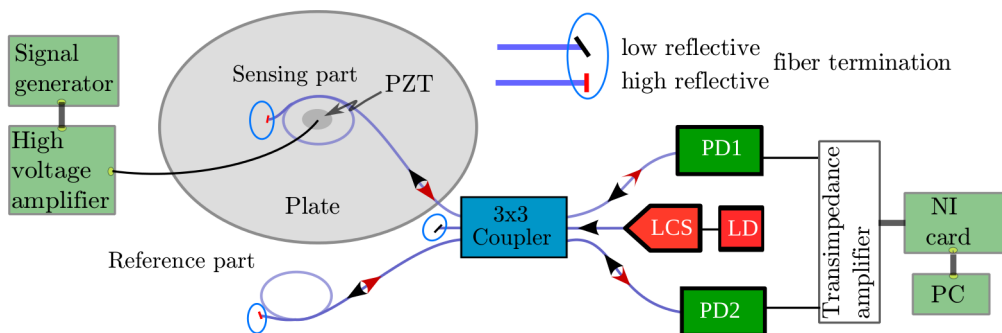


Figure 5.4: Block diagram of the experimental setup. Blue lines symbolize optical waveguides. Piezoelectric actuators fixed to the plate: two PZT discs (10 mm diameter, 0.5 mm thick) were used in pair to generate  $A_0$  and  $S_0$  mode Lamb wave in a 450 mm diameter plate. A circle fiber-optic transducer is used as sensor to collect the wave signal.

### 5.2.1 Data processing

To extract the hoop strain imposed by the angular or circular crested elastic wave from the interferometric data stream, additional signal processing of the sampled photodetector

outputs is mandatory. As the data acquisition module NI USB 6225 card applies sequential sampling of the channels a time shift of  $1 \mu\text{s}$  between subsequent signal samples is caused. Thus a time lag of  $1 \mu\text{s}$  between the samples of the first and second channel results. Hence, the data samples must be preprocessed to gain synchronous sampling. Afterwards, these preprocessed signals have to be evaluated according to the interferometric transduction scheme.

A Whittaker-Shannon interpolation of the raw data was performed to generate intermediate data points in each sample stream. The interpolation density must be chosen in such a way that sampled or interpolated points are found in both streams that belong to the very same nominal time. Prior to the interpolation, a Tukey window was applied to the raw data to avoid aliasing effects. To achieve synchronous pseudo sampled sequences, a specific number of data points must be discarded at the beginning of the first as well as at the end of the second channel sequence.

Whittaker-Shannon interpolation presumes that the probed signal lacks of frequency components beyond half the sampling rate. In the current case, the interferometer output signals satisfies this condition. To avoid violation of the sampling theorem by, e.g. photodetector noise, the TIA output can be filtered accordingly. This measure proved to be unnecessary due to a high signal to noise ratio.

The applied evaluation of the phase retardation follows the ellipse evaluation algorithm presented in [104] developed for field-quadrature interferometers.

According to the interferometer function for perfect coherent light, the acquired photodetector signals

$$V_1(t) = V_{10} + V_{11} \cos(\delta(t) + \varphi) \quad (5.1)$$

$$V_2(t) = V_{20} + V_{22} \cos(\delta(t) - \varphi) \quad (5.2)$$

vary with the cosine of the phase variation of the measurement arm,  $\delta(t) = 4\pi \Delta l(t) / \lambda$ , where  $\varphi$  denotes the actual coupler phase shift,  $\Delta l(t)$  means the optical path length difference of the interferometer arms and  $\lambda$  is the wavelength of the guided light. An orthogonal plot of  $V_1(t)$  versus  $V_2(t)$  has the form of an ellipse. Since guided elastic waves (GEWs) cause only small variations of  $\delta(t)$ , the parameters  $V_{10}$ ,  $V_{11}$ ,  $V_{20}$ ,  $V_{22}$ , and  $\varphi$  must be derived from an ellipse fit to the acquired data. The phase retardation  $\delta(t)$  can then be obtained from:

$$\tan \delta(t) = \frac{V_{11} (V_2(t) - V_{20}) - V_{22} (V_1(t) - V_{10}) \cos \varphi}{V_{11} (V_2(t) - V_{20}) + V_{22} (V_1(t) - V_{10}) \sin \varphi}. \quad (5.3)$$

Due to the limited coherence length of the SLD LED, however, the Lissajous presentation of the photodiode signals forms an elliptic spiral rather than a single ellipse [50]. Nevertheless, an approximate ellipse fit [111] works fine as the typical detuning of the interferometer due to GEW waves is much smaller than a wavelength. The applied approach is only approximate although the introduced error is small compared to other experimental uncertainties discussed below. Near-to-optimum parameters of the double interferometer ellipse fit to the data were found by visual judgment of the fit quality (see, e.g., Fig. 5.5) and deliver the parameters  $\varphi$  and  $V_{10}$  to  $V_{22}$ . This cumbersome procedure is more reliable than available ellipse fitting algorithms since the available data points mostly cover only a small segment of the elliptical spiral.

The sought quantity, i.e.  $\delta(t)$ , is insensitive to variations of the LCD output power. The circumferential elongation  $l_C(t)$  at  $r_F$  is obtained from:

$$l_C(t) = \frac{\delta(t)}{4\pi} \frac{\lambda_0}{n_{\text{eff}} - 0.3141}, \quad (5.4)$$

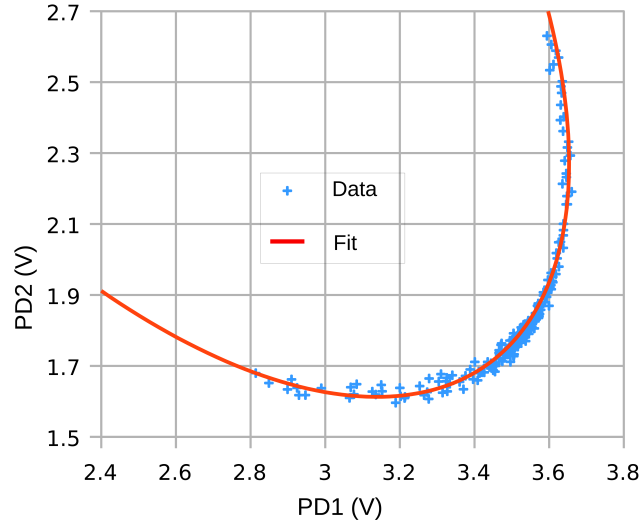


Figure 5.5: Example of an ellipse fit to the interpolated photodiode signal pseudo samples. Fit parameters: main axis inclination  $\varphi = 124^\circ$ , maximum peak-to-peak variation  $V_{11} = 1.323$  V,  $V_{22} = 1.689$  V, and ellipse center  $V_{10} = 2.34$ ,  $V_{20} = 3.31$  V.

with  $\delta(t)$  derived from Eq. 5.3 where  $\lambda_0$  denotes the vacuum wavelength of the guided light,  $n_{\text{eff}}$  the effective refractive index for the guided light, and the constant in the denominator is a consequence of the strain optic effect according to Eq. 3.23 [86]. The corresponding radial displacement  $u_{\text{TF}}$  measures  $u_{\text{TF}} = l_{\text{C}}(t)/2\pi$ .

## 5.2.2 Measurement results

Figure 5.6 shows the evaluation of a typical measurement run where the basic offset of  $\delta(t)$  has been removed. It gives an impression of the density of sequential sample rate ( $2 \mu\text{s}$  pitch) and the interpolated signal ( $0.2 \mu\text{s}$  spacing). All following diagrams display only interpolated signals.

The train of varying pulse echoes exhibit a regular delay of about  $90 \mu\text{s}$  confirming that a single propagation velocity predominates while the maintained compactness of the pulses indicates the low dispersion of the applied GEW mode. From the echo repetition rate and the plate diameter of  $491 \text{ mm}$  a propagation velocity of about  $5500 \text{ m/s}$  can be calculated. The primary response of the interferometric transducer resembles the inverted shape of the excitation voltage as expected from the negative value of  $d_{31}$ . The further echoes differ in shape from the primary pulse as they represent a superposition of converging and diverging circular crested GEW packets.

Furthermore, intermediate features are observable featuring a delay of about  $225$  and  $450 \mu\text{s}$  with respect to the primary pulse. These findings suggest that beside of the intended  $S_0$ -like mode, an  $A_0$ -like mode is excited in the aluminum plate too. In view of the symmetric excitation, this finding may be attributed to deviations from mirror symmetry that may result from, e.g., an imperfect repair of the partially damaged actuator metalization with conductive silver filled epoxy resin (see detail view of Fig. 5.2). An echo delay of about  $225 \mu\text{s}$  corresponds to a group velocity of about  $2.07 \text{ km/s}$  that fits well to the  $A_0$  group velocity dispersion characteristic for a  $f \cdot d$  product of  $0.2 \text{ km/s}$  according to Fig. 4.2. From Fig. 5.6 one can conclude that the fiber-optic transducer performs for flexural waves as well.

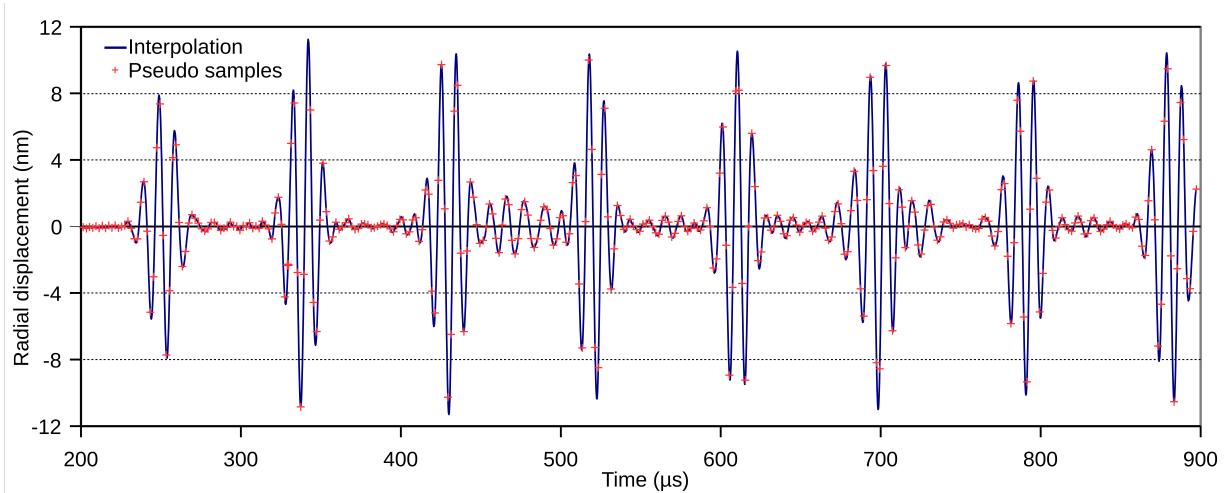


Figure 5.6: Radial displacement response to a symmetric 100 kHz Morlet wavelet deformation pulse of the piezoelectric actuators. Non-interlaced pseudo samples and the Whittaker-Shannon interpolated curve of the processed data are shown. The time scale refers to the trigger of the AWG, that is about 250  $\mu\text{s}$  in advance from the center of the excitation pulse to provide a baseline.

Figure 5.7 shows three subsequently recorded and processed responses that demonstrates the excellent repeatability of the experimental setup. The low frequency-thickness product of 200 m/s assures that no higher order modes are excited. In the Fig. 5.7, the vertical axis is scaled for the radial displacement at the fiber radius, i.e.,  $r = 12.5 \text{ mm}$ . Figure 5.7 reveals a repeatability of the pulse magnitude better than 1 nm. Moreover, the ripples between the pulses are reproduced with even better precision. From these results, a rough estimate of the measurement resolution can be derived. Assuming an arbitrary deviation of 0.1 nm between the curves, a strain resolution of  $2\pi \cdot 0.1 \text{ nm} / 2\pi \cdot 12.5 \text{ mm} = 8 \cdot 10^{-9}$  results that can be considered as an upper bound of the achieved resolution.

As expected from simulations, a single mechanical pulse induced by the piezoelectric actuator is followed by numerous regular echoes due to the specific boundary conditions of the circular plate. Whereas, the first pulse in the diagram of Fig. 5.7 consists of a pure expanding wave, the following echoes consist of the superimposed displacement of a contracting and an expanding wave. This is a consequence of the pulse duration of about 50  $\mu\text{s}$ , while a rough estimate of the delay between contracting and expanding wave amounts only  $25 \text{ mm} / v_g = 4.58 \mu\text{s}$ . The related phase shift adds to the phase jump required to maintain zero motion at the axis. Hence, we have approximate by constructive interference and the displacement swing of the echoes is somewhat higher compared to the primary signal. Figure 5.8 shows the complete processed experimental records. The shown time scale refers to the trigger of the electrical excitation pulse. The diagram starts with the primary elastic pulse and extends until the ramp down period of the applied Tukey window. A full raw data record period lasted for 1 ms while the excitation voltage pulse was launched with a delay of 200  $\mu\text{s}$  to assure the level of the initial baseline of the interferometer. The processed record reveals the appearance of marked pulses every  $\approx 90 \mu\text{s}$  with no noticeable decay. Obviously, diverging GEW-pulse-echoes are excited at the symmetry axis in addition to the pulse reflection at the circumference of the plate. As the pulse echoes do not spread significantly with time, isotropic wave propagation, simultaneous reflection at the plate boundary as well as negligible

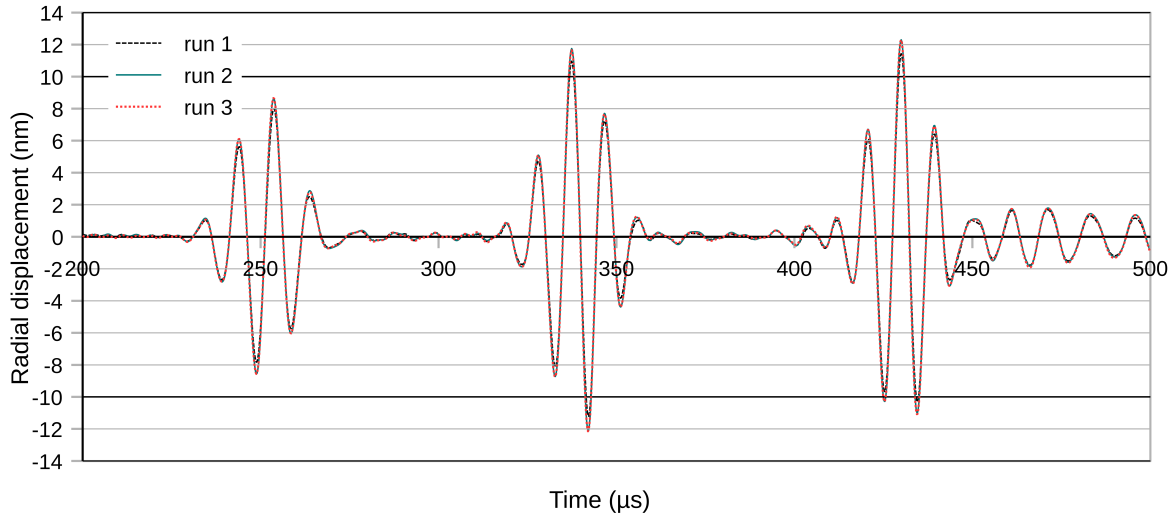


Figure 5.7: Signal processed responses of the fiber-optic transducer to symmetric pulse excitation of both actuators for three subsequent experimental runs taken in time intervals of 1 ms to ensure sufficient decay of the residues of the prior pulse.

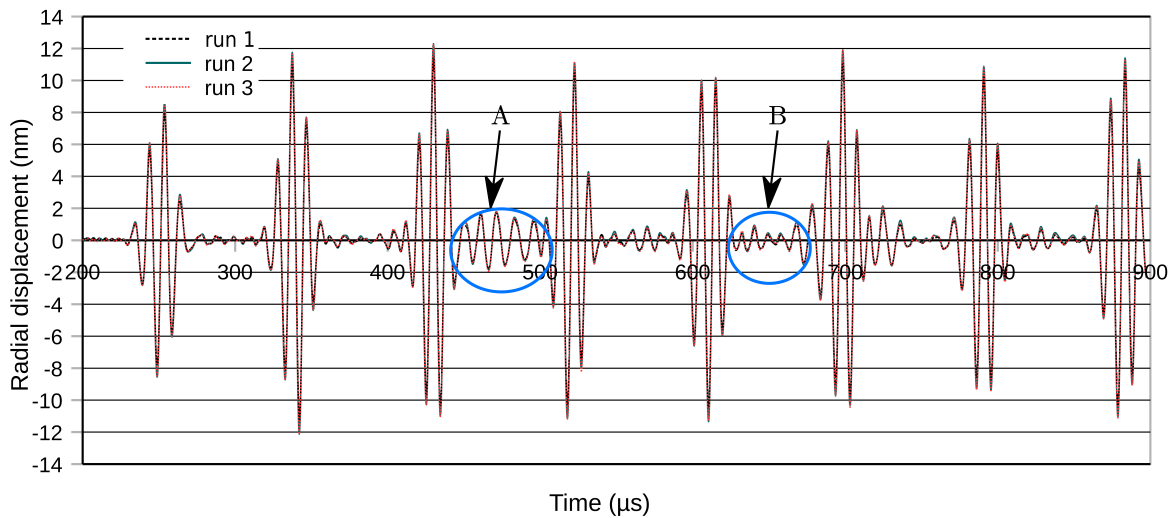


Figure 5.8: Complete processed experimental record. The measurement window amounts 1 ms while the portion whereas the diagram omits the initial pulse delay (200  $\mu\text{s}$ ) and the final ramp down of the Tukey window (100  $\mu\text{s}$ ). Points *A* and *B* are the indirect generated flexural waves.

wave dispersion is guaranteed. A close inspection of the wave train suggests additional signals between 450 and 500  $\mu\text{s}$  and around 730  $\mu\text{s}$  record time, respectively. These features are missing in the results of corresponding simulation's excitation signal recovering in the chapter 4 (see Fig. 5.8, *A* and *B*). Apart from these differences, the simulated and measured shapes of the primary pulse as well as the respective echoes are very similar. The in-depth discussion of these findings is postponed to the next chapter.

## 5.3 Novel robust optic fiber transducer

The experimental testing of the functionality and the examination of some sensing properties a prototype of this robust transducer was mounted on a preconfigured test plate. The developed robust fiber-optic transducer, was realized as described in the modeling section 4.2.

### 5.3.1 Design of the robust fiber-optic strain transducer

The new transducer design employs a sandwiched structure including a thin plate, which is attached to the sample with one surface and bears the measurement fiber on the opposite side. The fiber is firmly attached to this plate that acts as strain coupler between body and fiber on the one hand and as mechanical protector for the fiber on the other hand. An identical protector plate carries the reference fiber in Fig. 5.9.

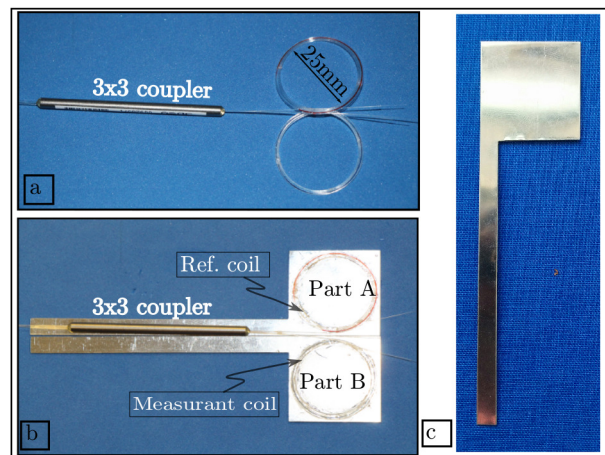


Figure 5.9: Robust transducer : *a*) development of measurant and reference arms: Both are identical, 5 turns coil, 25 mm of diameter; *b*) components of the sandwich structure with glued sensing and reference coil at each part. The sensing fiber attached to the upper carrier while the reference is glued to the lower carrier. The  $3 \times 3$  coupler is fixed to the lateral extension, *c*) transducer system filled with soft silicone elastomer.

The protecting carrier material has been selected based on the simulation results of the previous chapter. It must be resistant to be buckled by external forces but sufficiently compliant to the elastic deformations of the sample. The simulations of the robust transducer revealed that polyimide is the preferable carrier material. As this material was not available on short terms, stainless steel sheets (AISI 304 (Fe/Cr18/Ni10), 150 mm  $\times$  150 mm, 0.5 mm thick) of Goodyear Company, which also meet the support material criteria, were chosen for prototyping. This solution is considered a good compromise of high robustness and sufficient mechanical sensitivity.

Two identical spiral coils of five turns with a 25 mm outer diameter were shaped using Corning SMF 28<sup>+</sup> monomode optical fiber corresponding with two output fibers of a  $3 \times 3$  fiber-optic directional coupler (see Fig. 5.9 a). They played the role of measurement and reference coil. The optical path length in the sensing and reference arm was matched and the end faces were supplied with a highly reflective coating. The measurement and reference fibers were rigidly attached to the respective carriers with LOCTITE 401 cyanoacrylate adhesive forming part A and part B according to Fig. 5.9 b. Afterwards, the system was folded

keeping sufficient distance between the carriers to accommodate the fiber-optic coupler in between. To enable good thermal contact and to avoid transmission of dynamic strain variations between sensing and reference arms, a soft silicone elastomer was filled in the gap between the protecting carriers. The reference fiber coil is supposed to be unaffected by the structure displacements and changes its optical length only under the influence of temperature variations for example. Furthermore, the elastomer filler reduces the temperature gradient across the interferometer improving the stability enormously. The third output arm of the  $3 \times 3$  coupler was polished at an angle of  $8^\circ$  to suppress the back-reflection from this fiber tip. The finished robust and reusable fiber-optic transducer is shown in Fig. 5.9 c.

### 5.3.2 Testing concept of the robust transducer

The robust transducer was firmly attached on a 5mm thick CFRP plate composed of 16 cross-ply layers featuring a size of  $400 \text{ mm} \times 80 \text{ mm}$ . The transducer was seated at 152 mm in  $x$ , and 37 mm  $y$  directions from the lower left plate corner. The specimen was also equipped with four piezoelectric actuator patches (1– 4 from Acellent Smart Technology) that have been affixed at 40 mm and 10 mm distance in  $x$  and  $y$  direction, respectively, from each corner of the plate as shown in Fig. 5.10.

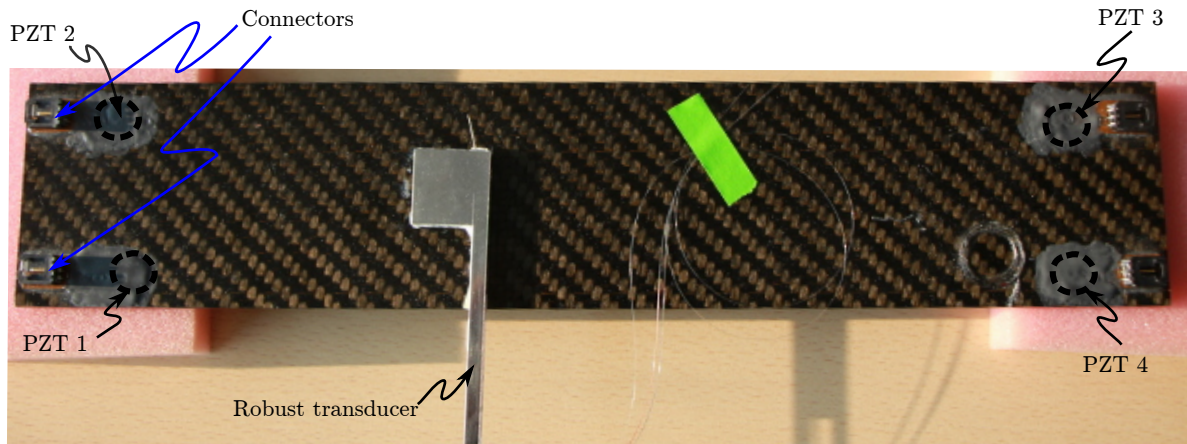


Figure 5.10: Composite plate sample with actuators at the four corners and the robust transducer.

The robust compact and reusable structure of fiber-optic transducer for harsh environments was glued with LOCTITE 401 on a preconfigured CFRP plate, which has been equipped with four piezoelectric actuators (PZT\_1 – 4). The transducer was placed closer to the actuators 1 and 2, to allow a diversification in propagation distance for the generated elastic waves.

The raw photodiode signals were converted by two the transimpedance amplifiers (TIA) into voltage signals and input to a 16 bit high-performance M-series multifunction NI USB-6225 card (up to 1.25 MS/s single-channel) with a sampling rate of 500 kS/s and 1000 samples which gives a total acquisition time of 2 ms.

For elastic waves production, a Stanford Research System waveform generator (Type DS345) was used to generate sine-burst signals for piezoelectric actuator excitation. Different sine-burst signals

$$s(t) = U \cdot \sin(\omega t) \cdot \sin^2(\omega t/N), \quad 0 \leq t \leq 2\pi/\omega$$

with  $N = 2, 3, 5$ , and center frequencies of  $10 - 50$  kHz. A high voltage amplifier (New Focus Model 3211) was used to rise the excitation voltage level to  $U = 75 - 90$  V magnitude producing elastic waves in the plate. Signal were sent alternatively from the actuator PZT\_1 and actuator PZT\_3.

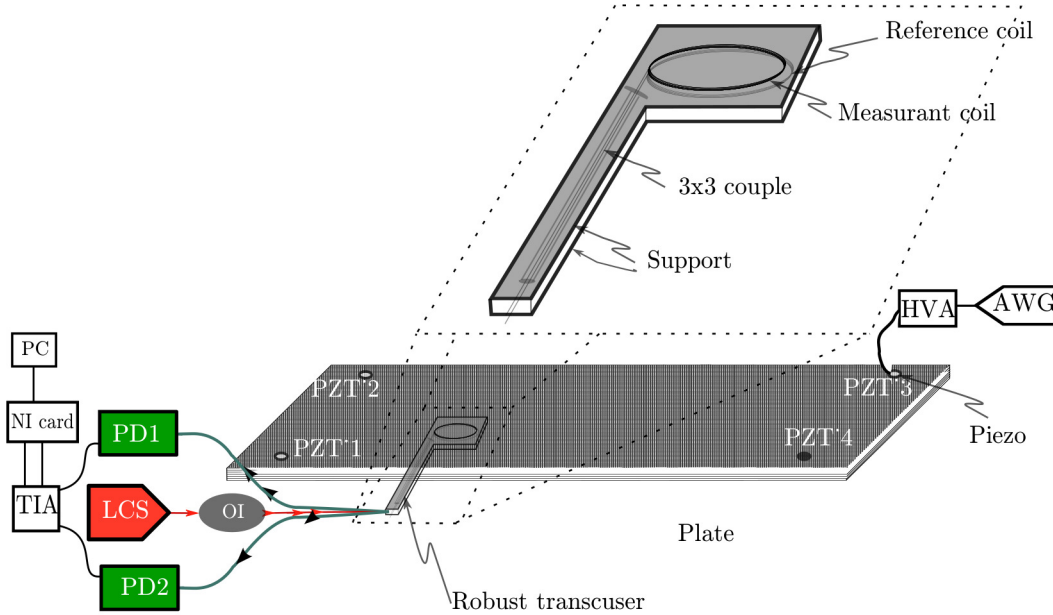


Figure 5.11: Experimental configuration of the robust and reusable fiber-optic transducer testing bed.

The electronic output signal depending on the optical phase difference was processed off-line to derive the elongation of the measurement coil.

### 5.3.3 Sensitivity tests

The main question was whether or not the robust transducer is capable to acquire strain variations in the plate that are evoked by typical guided elastic waves. Plate dimensions and available frequency range prevents for the measurement of a single wave packet. Within the time period of data acquisition multiple reflections occur from all four boundaries of the plate as well as scattering from the attached actuators. Furthermore, the excitation pulse duration is much longer than the respective forward-backward propagation delay of the excited ultrasonic waves. Thus, the measured response of the transducer does not allow a straightforward interpretation. However, the fidelity of the processed signals can be judged from a comparison of several runs of the same experiment.

Figures 5.12 and 5.13 depict the calculated fiber elongation for actuation with PZT1 and PZT3, respectively. In both cases, a single-sine burst of 10 kHz according to Eq. 4.5 was applied to the actuator. Bearing in mind that the first reflected waves arrive with a delay of only a few  $\mu$ s, it can be imagined that a large number of partial waves occur even during the actuation period of 100  $\mu$ s.

An inspection of the traces indicate that the approximate phase retardation resolution of the robust transducer is of the order of about 0.2 nm. For a rough estimate of the related plate strain, one can make use of the fact that mechanical wavelengths at 10 kHz are about 0.5 m, much larger than the fiber coil diameter. Using the window function for a circular

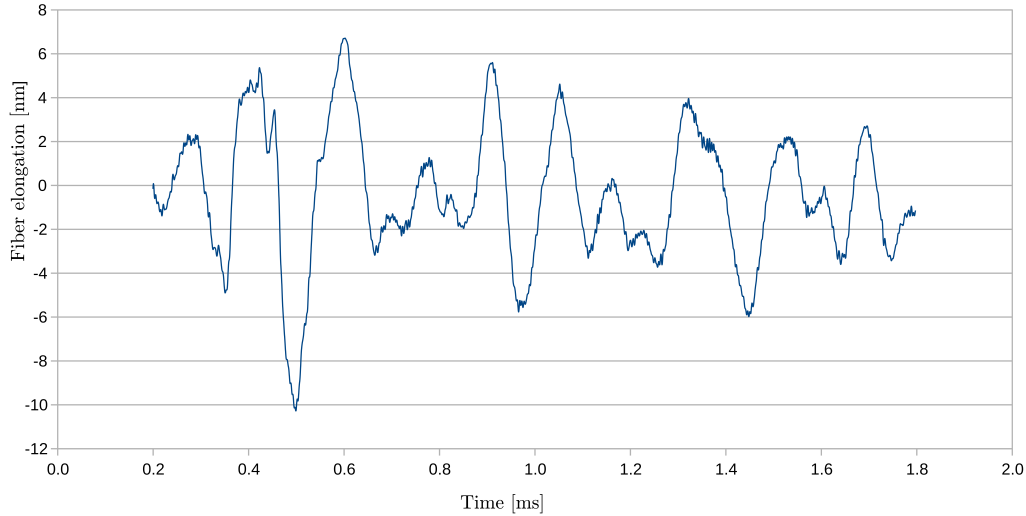


Figure 5.12: Experimental fiber elongation of a 5-turn spiral coil of the robust transducer in the case of actuation of PZT1 with a single sine burst at 10 kHz and 180 Vpp.

fiber in Eq. 3.26 and unidirectional strain, Eq. 3.7, and considering five turns of the spiral, the path length resolution of 0.2 nm translates into a resolvable unidirectional elongation of the fiber of about  $\delta L = 200 \text{ pm}/5\pi \approx 12.7 \text{ pm}$  over one fiber coil diameter. The related resolution for or uniform strain is  $\varepsilon \approx 5.1 \cdot 10^{-10}$ , which is a very encouraging result.

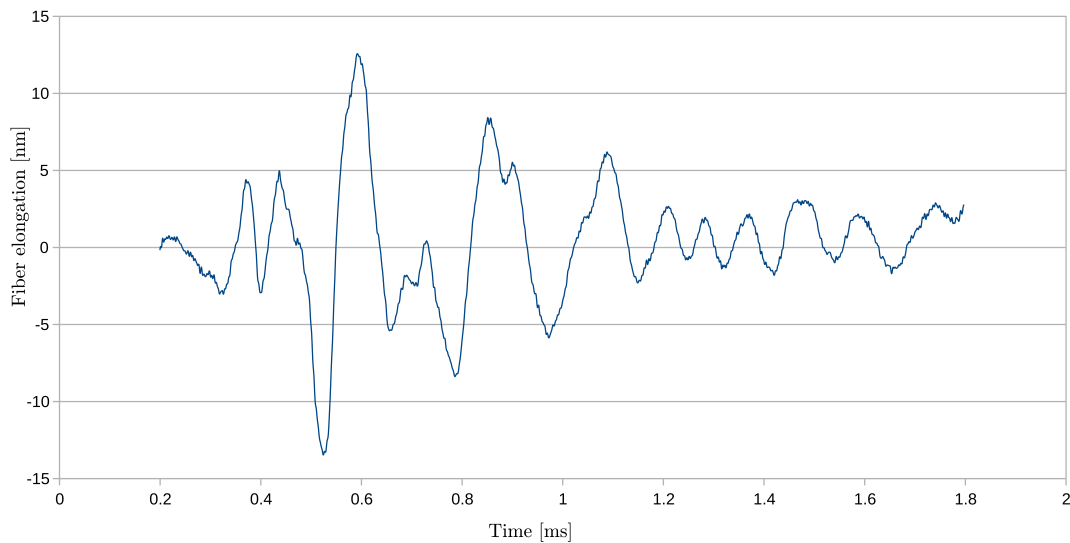


Figure 5.13: Experimental fiber elongation of a 5-turn spiral coil of the robust transducer in the case of actuation of PZT3 with a single sine burst at 10 kHz and 180 Vpp.

## 5.4 Summary

An experimental arrangement has been set up with the capability of quantitative comparison between interferometric strain measurements and related FEA results. The optical part

was complemented by the data acquisition capacity for the recording of the transient wave signals for omnidirectional fiber-optic transducers as well as robust fiber-optic transducers. The measurements with the reference setup reveal a satisfying qualitative and quantitative agreement with basic features of related FEM simulations that will be analyzed in the next chapter.

The sensitivity of the robust fiber-optic transducer is very encouraging in spite of the comparable rigid protective steel carriers used for the first implementation. Strain sensitivities of the order of  $10^{-8}$  seem within reach.

# Chapter 6

## Discussion of results

The following sections discuss the result of elastic wave experiments compared to simulations. Conclusions are drawn with respect to the predictive quality of the finite element simulations.

### 6.1 Reference model

The work is characterized by an almost one-to-one correspondence of the finite element model with the implementation used for the measurements. This enables a complete input-output comparison of the FEA with the experiment. The interferometer signals have been processed as described in 3.6.2 to yield the radial displacement at the fiber bending radius  $r_F$ . Figure 6.1 displays the time dependence of the measured radial displacement and the related simulation result for pure symmetric excitation. To enable a straightforward interpretation, the center of the primary wave pulses have been made congruent and the timescale refers to the trigger moment of the experiment. The actuation in form of a Morlet wavelet voltage pulse has been started 200  $\mu\text{s}$  after trigger to get a baseline signal in advance.

For the primary pulse, a nearly quantitative agreement between measurement and simulation is observed. In contrast, the magnitudes of the simulated pulse echoes exceed their measured counterparts markedly although the respective pulse shapes are similar.

The primary pulse is determined solely by the radial displacement imposed by the piezoelectric actuators and the elasticity parameters of the aluminum plate don't affect this displacement magnitude appreciably. The excellent agreement of the curves indicates that the FEM model describes the actuation magnitude very precisely.

From Fig. 6.1 it becomes obvious that the time course of the main echo pulses diverges with time. Therefore, the propagation speed of the simulated wave pulse differs from the pulse propagation velocity found in the experiment. For the selected pulse parameters, all echo pulses consist of a superposition of converging and diverging pulse packets at the radial distance  $r_F$ . The result of this superposition depends on the frequency, a phase jump at the axis, and a propagation time  $\approx 2r_F/v_{PH}$ . As a consequence, the measured magnitudes of the echo pulses depends on the actual value of  $v_{PH}$  and may differ from the simulation results.

Furthermore, Fig. 6.1 indicates a region where the time course of the measurement deviates significantly from the simulation results, notably around 470  $\mu\text{s}$  and 690  $\mu\text{s}$  elapsed time. The related echo delay is about 220  $\mu\text{s}$  with respect to the primary pulse. Based on the plate radius of  $r_D = 245.5 \text{ mm}$ , this round trip time corresponds to a group velocity of approximately 2230 m/s which is typical for the fundamental flexural mode at  $f \cdot d =$

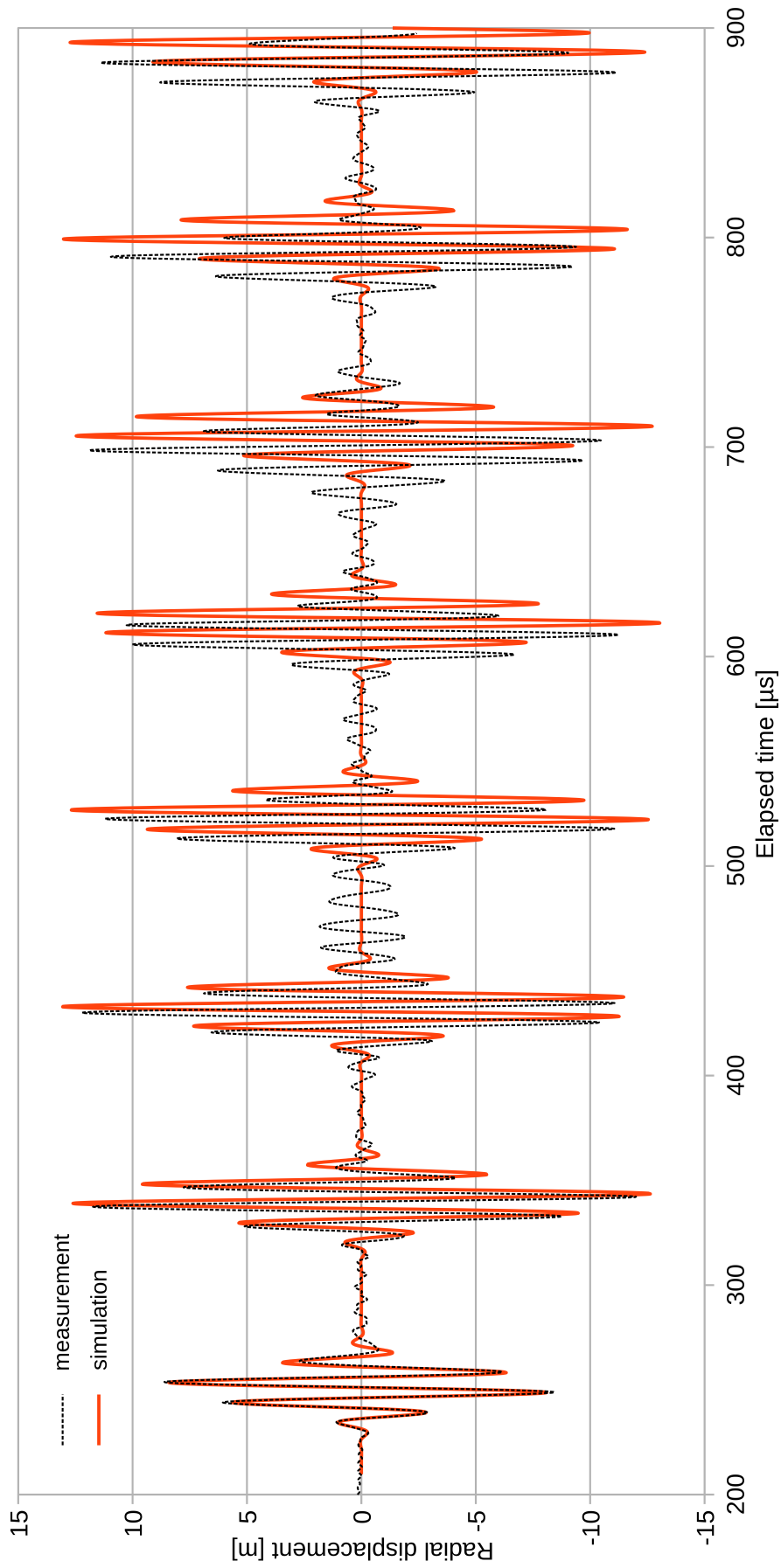


Figure 6.1: Simulated radial displacement for symmetric excitation and radial displacement derived from the transducer output. A time offset is added to the simulation result to achieve congruence of the primary pulses.

200 m/s (see Fig. 4.2). Hence, these additional features may be attributed to an unintended antisymmetric perturbation induced by the piezoelectric actuators.

Indeed, one of the actuator's electrodes had been slightly damaged during soldering of the coaxial voltage supply lines. Furthermore, the axes of the actuators may not coincide perfectly due to the imperfect positioning of the actuators by hand or an unintended slipping during the curing of the conductive epoxy resin.

To further support the conjecture of antisymmetric waves, the simulations were repeated but with an  $\pm 10\%$  amplitude mismatch between the top and bottom excitation voltages that ensures a symmetric perturbation as before with an added antisymmetric perturbation in the plate. The related results are depicted in Fig. 6.2 together with the measurement result. In intention to give a clear view, the time scale of the simulated trace is multiplied by an appropriate factor to achieve congruence for the pulse echoes of the compressive mode. As expected, the new features introduced the asymmetric excitation appear in the right region.

**Model adaptation to achieve synchron compressive mode pulses** Based on the plate diameter, propagation velocities of about 5370 m/s and 5456 m/s can be deduced from the echo delay of the compressive pulses for the simulation and the experiment, respectively.

Since at low  $f \cdot d$  values  $v_g \cong v_{PH}$  holds for the fundamental compressional mode, Eq. 2.25 suggests that, based on the simulation parameters, the expression

$$E(1 - \nu)/\rho(1 + \nu)(1 - 2\nu) \quad (6.1)$$

determining the phase velocity of compressional waves, is too low by about 3%. This deviation must result from differences between the true material parameters of EN AW6082 and EN AW6070 (UNS A96070) of the COMSOL material library that specifies  $E = 69.138$  GPa and  $\nu = 0.33$  at room temperature (293 K). To increase the phase and group velocity of the simulated compressive pulses, the ratio  $E/\rho$  as well as the Poisson ratio  $\nu$  may be increased. Arbitrarily, the phase velocity was adapted by solely increasing the Young's modulus to 71.2 GPa and the related simulation result is displayed in Fig. 6.3 together with the measurement outcome.

Now all compressive pulses of the time-scale manipulated simulation seen in Fig. 6.3 coincide with their experimental counterparts and the magnitude mismatch is reduced.

The experimental trace illustrates that there is no perceivable decrease of the measured pulse echo magnitudes within the time window of the experiment of about 0.75 ms. Therefore, the pulse broadening with propagation time must be very moderate and a large temporal extension of the experiment is conceivable. Such measurements would allow much more precise estimates of the group velocity of compressional waves. Since no significant dispersion of the pulses was found, the relation  $v_g \cong v_{PH}$  holds for the simulation as well as for the experiment.

Although a satisfying congruence of the echoes of the compressive wave is achieved by the adaptation of the Young's modulus, the echoes of the flexural pulses are barely met.

**Model adaptations affecting flexural waves** For better coincidence of measured and simulated flexural wave pulses, several modifications of the simulation model are feasible.

First, the dependence of the phase velocity of longitudinal and transversal waves on the Poisson ratio may be exploited to achieve a better match for both, flexural and compressive modes, simultaneously. While the expression Eq. 6.1 lead to an increase of the phase velocity of compressive waves, the respective expression for transversal waves

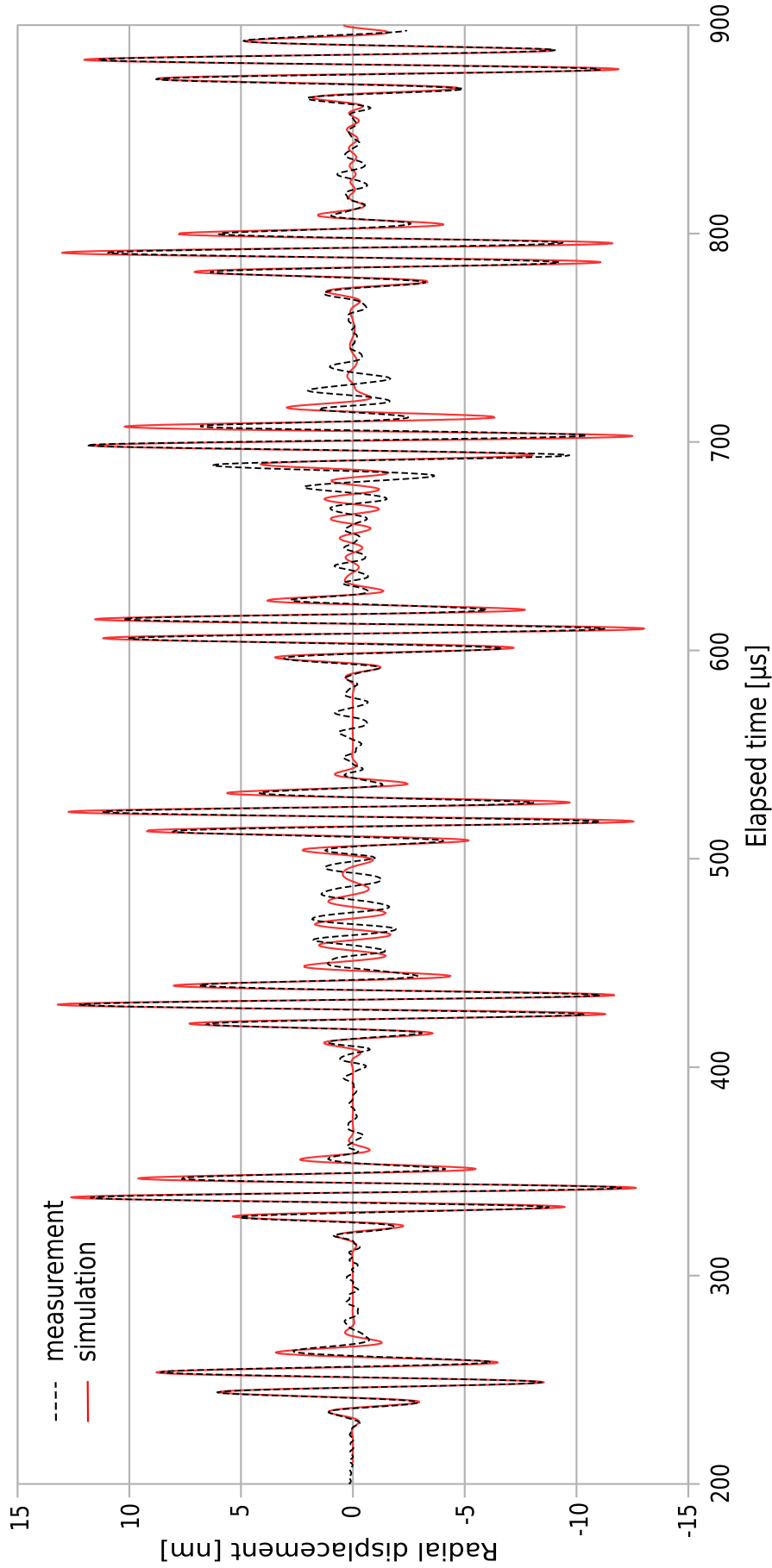


Figure 6.2: Measured radial displacement and simulated trace for a mixed flexural and compressional excitation. The times axis of the simulated results is multiplied by 0.984 to achieve synchronization of measured and simulated compressional wave pulses.

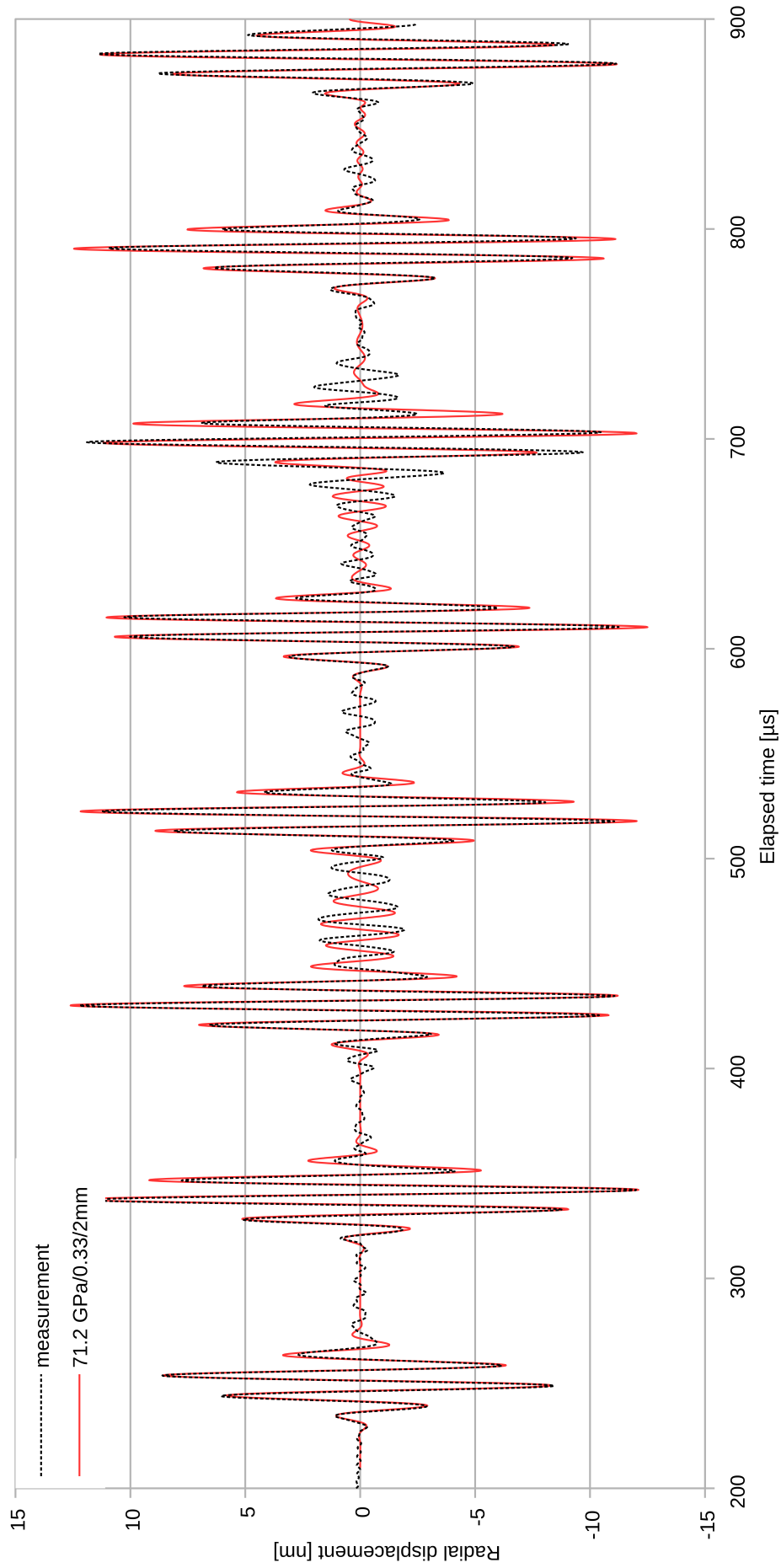


Figure 6.3: Measured radial displacement and simulated trace for a mixed flexural and compressional excitation and a Young's modulus of 71.2 GPa.

$$E/2\rho(1 + \nu) \quad (6.2)$$

decreases with increasing Poisson ratio. Interestingly, the ratio

$$\frac{v_T}{v_L} = \sqrt{\frac{1 - 2\nu}{2(1 - \nu)}} \quad (6.3)$$

depends only on the Poisson ratio. However, it turns out that tuning both phase velocities appropriately by variation of  $\nu$  would require Poisson ratios of about 0.4, which is too far from the well established value of  $\approx 0.33$  for EN AW-6082.

Second, the phase and group velocity of the fundamental flexural mode increases also strongly with the plate thickness  $d$  in the region of low  $f \cdot d$  products that is relevant for the current experiment. Hence, the plate thickness is a parameter of the simulation model that can be used to achieve a better fit to the experiment. The aluminum thickness was measured as  $1.973 \pm 0.008$  mm.

Third, two possible options of the  $\pm 10\%$  asymmetry of the actuation exist.

Figure 6.4 depicts a related simulation result, based on  $\nu = 0.337$ ,  $E = 71.0$  GPa, and the measured plate thickness aside with the experimental result. The excitation at the surface bearing the fiber optic transducer is assumed to be 20% less than the actuation on the opposite side. A good approximation to the features attributed to the flexural pulse echoes in the experiment is now achieved with no detrimental effects on the fit quality of the compressive pulses. Only for elapsed times between 700 and 750  $\mu\text{s}$  marked deviations from the measured trace occur.

It was shown that with slight modifications of the elastic parameters of the aluminum plate a satisfying agreement between measurement and FEM results can be achieved. However, a considerable asymmetric excitation is required for a sufficient match to the measured flexural pulses. This finding is rather surprising in view of the good agreement obtained for the compressive pulses. The reason for the comparatively strong antisymmetric wave pulses of the measurement remains unclear.

## 6.2 Results for the robust transducer

The main purpose of this activity was to demonstrate the feasibility of a robust fiber optic transducer that is capable to resolve strain variations with high resolution and bandwidth.

The measured and simulated time courses of the fiber elongation of the robust transducer shown in Figs. 4.36, 4.37 and Figs. 5.12, 5.13, respectively, show all rich features. In contrast to the results of the reference configuration, the simulated and measured curves of the robust transducer look quite different. Indeed, even a qualitative comparison of FEM and experiment seems impossible due the complex transmission behavior of the system. Several effects contribute to the rich features of the results:

1. Due to the single side excitation antisymmetric as well as symmetric plate wave modes are excited featuring different propagation speeds.
2. Due to the low pulse frequency and long pulse duration of 100  $\mu\text{s}$  while a compressive wave needs only about 70  $\mu\text{s}$  to pass the largest dimension of the plate. Thus reflections

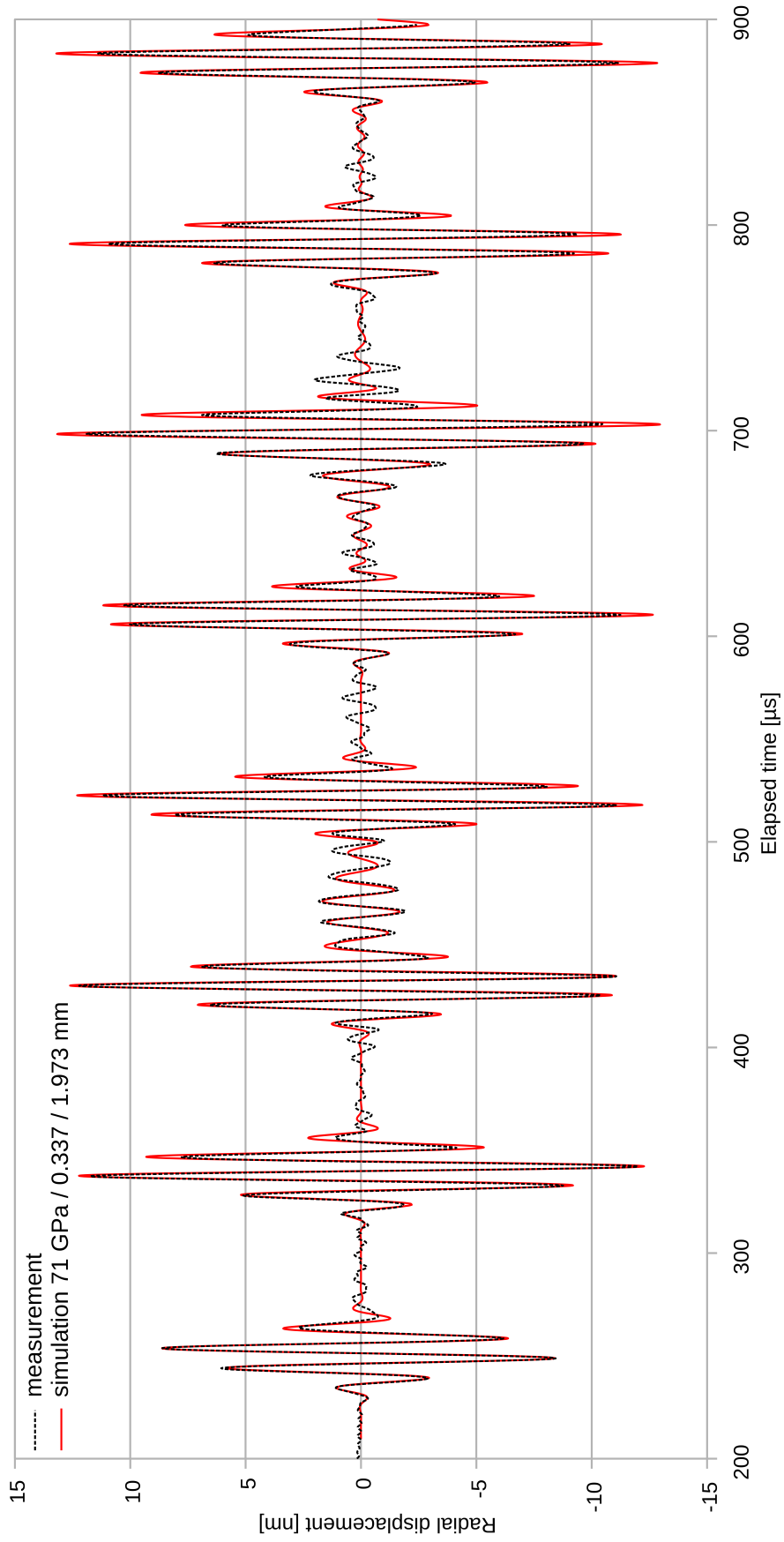


Figure 6.4: Comparison of measurement and simulation based on adapted plate material parameters.

at all four plate borders contribute to the shown measurement result of the fiber-optic transducer. Hence, the transducer signal suffers from pronounced multipaths transmission of the pulsed perturbation.

3. The anisotropic and inhomogeneous nature of the CFRP plate causes, e.g., directional variations of the propagation speed that are not sufficiently reproduced by the orthotropic plate material used in the simulations.
4. Strongly dispersive flexural waves contribute to the transducer output.
5. Different actuator types were utilized in both cases.
6. The simulated transducer consists of a single fiber circle while in the experiment a 5-turn fiber-optic coil was attached.
7. Minor effects like reflections of elastic waves by the attached robust transducer.

Figures 5.12 and 5.13 exhibit a peak length change of about 10 nm and 13 nm of the 5-turn, spiral wound fiber in response to actuator PZT1 and actuator PZT3. The simulations give a peak value of 3 nm for a single-turn fiber optic transducer. Hence, for the 5-turn spiral wound fiber of the robust transducer implementation one would expect about 15 nm magnitude. Considering that the simulated actuator differs from the device used, there is a reasonable agreement between simulation and measurement. These length variations are within one order of magnitude with the simulated data of Figs. 4.32 and 4.33. Thus the selected FEM approach provides a reliable toolbox aiding the design of such robust transducers.

# Chapter 7

## Conclusion and Outlook

### 7.1 Scope of the work

The inspiration for this thesis came from the urgent need for powerful structural health monitoring systems to maintain the safety of critical aviation infrastructure. Sensors for structural health monitoring should be easy to apply, cheap, highly sensitive, robust, able to survey large areas of sheet-like constructional elements and feature moderate power consumption. They should be able to monitor both aluminum and composite materials, where the use of the latter is becoming increasingly important in aerospace industry. The investigated technical approach seems to be a well suited candidate for such tasks.

Non-destructive examination of materials using ultrasonic elastic waves is one of the most promising ways. Lamb waves or closely related guided elastic waves are of particular relevance for the inspection of large structures. There are a number of reasons that allow this assumption: they permit the inspection of a 2-dimensional space rather than a single point; (i) they are adequately sensitive to flaws on either side or in the volume of the plate; (ii) they propagate over long distances; and finally, (iii) they are guided by the structure. To solve structural health monitoring tasks, a guided elastic wave application needs to be complemented by a competitive wave detection technology that effectively converts wave induced displacement or strain into appropriate signals for evaluation. This thesis opts for a fiber-optic strain transducing technology.

Fiber-optic strain transducers are considered in conjunction with elastic wave detection, as an appropriate means to convert strain variations: scattered waves induced by propagating in the structure elastic waves:

- they feature low weight and sufficient mechanical compliance for moderate loading of the monitored structure,
- they offer very high sensitivity,
- they feature high transduction bandwidth,
- they allow for pronounced directional as well as omnidirectional sensitivity characteristic,
- they exhibit immunity to the most important interfering quantities,
- and they enable signal guidance through particularly difficult environments.

The inherent drawback of light waveguide structures is that they are mechanically highly vulnerable, if they are not protected by suitable means. Furthermore, selected measurands such as the ambient temperature, impose a slow varying bias upon the fast varying strain that must be considered by an appropriate transducer design. However, the advantage of high sensitivity can be offset against by the sensitivity of such systems due to interfering influences. The current thesis employs specific fiber-optic interferometer implementations that address these topics. On the one hand, they offer high strain resolution; and on the other hand, flexibility of construction to enable a robust first order temperature compensation and

The scope of this thesis is the investigation of all major aspects of elastic wave generation in the field of SHM and certain selected method of their detection. The aim was to tackle the specific problems with finite element analysis and confirm related results wherever an experimental verification is feasible.

For practical reasons the experimental work is confined to elastic wave generation with commercial piezoelectric transducers and the measurement of the wave related strains by fiber-optic means. Furthermore, plates of aluminum and carbon fiber reinforced epoxy are chosen as the medium for elastic wave propagation.

To illuminate the related theoretical background, a short introduction into the theory of guided elastic waves as well as a review of fiber-optic transduction of wave strain was placed before the modeling and experimental sections.

## 7.2 Conclusions

The implemented fiber-optic strain transducer comprises a spiral wound fiber coil that enables omnidirectional sensitivity to plane elastic waves. The finite extension of the fiber coil leads to distributed strain sensing and thus, the conversion depends on the wavelength of the elastic waves. The related distortions of the strain conversion were investigated for plane elastic waves as well as for practically interesting cases of circular crested elastic waves. For an appropriate bending radius, the strain sensitivity grows in proportion with the number of turns of the coil.

Suitable simulation models have been derived in order to explore the physical foundations of SHM systems on the one hand, and to explain and predict measurement results on the other hand.

Fundamental issues were probed with abstract FE models. These models comprise small, rectangular plates of homogeneous orthotropic material and distinct propagating modes excited by artificial boundary conditions. With this approach, disturbances imposed on elastic waves in the plate by an attached transducer were successfully explored. It was shown that even in case of 0.75 mm thick plate, the loading by a 5-turn fiber-optic coil excites only minor wave reflection and mode conversion measuring a few percent of the incoming magnitude. An orthotropic material featuring stiffness comparable to carbon fiber reinforced epoxy was employed for this study.

A much more laborious effort was required to build FE models that enable a direct comparison with conducted experiments. Here, the complete chain of elastic wave actuation by piezoelectric transducers, the wave propagation in various plates and wave strain transduction by fiber-optic means had to be covered by the models.

It was also feasible to construct a FEM model geometry that can be readily implemented in an experimental setup. The key feature of both the model and the experiment, was axial symmetry of all system components aside with concentric arrangement of actuators,

fiber-optic strain transducer and a 2 mm thick aluminum plate. A direct comparison of input/output quantities was feasible for this setup enabling the validation of the performed FE analysis. Moreover, due to deviations from the ideal configuration, compression as well as flexural waves were observed in the experiment. This artifact enabled estimates for both the Young's modulus and the Poisson number to 71.0 GPa and 0.337, respectively. Even for a single-turn fiber-optic strain transducer, the achieved strain resolution of  $8 \cdot 10^{-9}$  competes well with the best commercial FBG sensors, although this result was achieved without any optimization of the detection system.

An especially challenging task was the modeling of elastic wave propagation in fiber reinforced material. According to the experiments, several layers of unidirectional fiber reinforcing with a variety of ply orientations acting along the symmetry of the elasticity were stacked and individually rotated to form the plate. This fine structured material requires fine simulation meshes, which requires huge sized simulation data files and extraordinary computational power at hand. Nevertheless, it was feasible to calculate models with relevance for complex practical implementations. It was shown that modeling such a CFRP as single solid of orthotropic elasticity leads to rather inaccurate predictions of elastic wave propagation.

Finally, an FE model of the novel robust fiber-optic strain transducer was established that enabled a direct comparison of simulated strain signal magnitudes with respective results of related experiments.

The actual implementation used a 5 mm thick plate made of 24 layers of cross-ply CFRP that was approximately modeled as an orthotropic solid. The sensitivity of the robust fiber-optic transducer is very encouraging in spite of the comparable rigid protective steel carriers used for the first implementation. The commercial piezoelectric actuator was used for implementation. From the measurement results one may conclude that strain sensitivities better than  $10^{-8}$  are well within reach.

### 7.3 Outlook

The experimental results of designing robust fiber-optic transducer suggests that the elements used may form a good general purpose tool for the large space monitoring of the composite material structures. However, open questions remain which should be investigated in the future work. The presented approach can be used to apply Lamb wave methods to detect damages like cracks in metallic structures or delamination in composites such as CFRP. It needs to be shown by further research that it is possible to locate and quantify damages in structures made of high-tech layered material with their sophisticated wave propagation behavior and complex boundary conditions.

Furthermore, considering that light propagation speed within optical fibers is very sensitive to variations of the waveguide temperature, appropriate compensatory measures by suitable interferometer arrangements are mandatory. The novel setup of the robust sensor points in the right direction, as it features a dramatic reduction in the temperature interference. Here, variation of the material combination for the sandwich composed of fiber carriers and soft intermediate layers must be solved to allow versatile adaptation to several circumstances of strain variation measurements.

The following list details some of the possible follow-up work recommended to further the goal of optical transducer systems for a wide variety of applications:

- Enhancing the reference model experiment to enable pure compressional and flexural wave modes and extend the studies on other  $f \cdot d$  products and frequency ranges.
- The modeling of anisotropic crossply composite laminate traversing by Lamb waves should be solved and compared with approximations by homogeneous materials.
- From the point of view of system complexity, it would also be interesting to perform more experiments using one set of transducer to perform several types of tests, which should also be implemented on representative structures in future testing. Since the present work only included newly manufactured specimens without introduced damage, and also did not account for the complexities inherent to retrofitting a system to an aging structure, a further testing of the same methods on materials in use would be desirable.
- In a parallel study on the elastic wave propagation, real-world structure elements may also be treated as multi-path transmission channels. Related knowledge is required for the evaluation by optical fiber detection and the discovery of structure changes in case of SHM.

# Bibliography

- [1] C. Boller and M. Buderath. Fatigue in aerostructures, where structural health monitoring can contribute to a complex subject. *Phil. Trans. R. Soc. A* 15, 3654(1851):561–587, Feb 2006.
- [2] N. Mrad. SHM implementation. In *Fly by Wireless Workshop (FBW), 2011 4th Annual Caneus*, pages 1–4, 2011.
- [3] P. Cawley. Low frequency NDT techniques for the detection of disbonds and delaminations. *The British Journal of Non-Destructive Testing*, 32:454–461, 1990.
- [4] G. Riegert, K. Pfeleiderer, H. Gerhard, I. Solodov, and G. Busse. Modern methods of NDT for inspection of aerospace structures. ECNDT, 2006.
- [5] C. M. Yeum, H. Sohn, and J. B. Ihn. Lamb wave mode decomposition using concentric ring and circular piezoelectric transducers. *Wave Motion*, 48(4):358 – 370, 2011.
- [6] S. K. Sethiya. Condition based maintenance. *Jabalpur, Secy.toCME/WCR/JBP*, 2005.
- [7] J. Edmonds and G. Hickman. Damage detection and identification in composite aircraft components. In *Aerospace Conference Proceedings, 2000 IEEE*, volume 6, pages 263–269 vol.6, 2000.
- [8] B. I. S. Murat and P. Fromme. Detection of impact damage in composite panels using guided ultrasonic waves. pages 869506–8, 2013.
- [9] S. S. Kessler, S. Mark Spearing, and C. Soutis. Damage detection in composite materials using lamb wave methods. *Smart Materials and Structures*, 11(2):269, 2002.
- [10] C. R Farrar and K. Worden. An introduction to structural health monitoring. *Phil. Trans. R. Soc.A* 15, 365(1851):303–315, Feb. 2007.
- [11] H. Lamb. On waves in an elastic plate. *Proc. R. Soc. Lond.*, 93:114–128, 1917.
- [12] E. Lehfelddt and P. Hoeller. Lamb waves and lamination detection. *Ultrasonics*, 5(4):255–257, 1967.
- [13] N. Guo and P. Cawley. The interaction of lamb waves with delaminations in composite laminates. *The Journal of the Acoustical Society of America*, 94(4):2240–2246, 1993.
- [14] L. Yaolu, Alamusi, J. Li, H. Ning, L. Wu, N. Hu, W. Yuan, and B. Gu. *Locating Delamination in Composite Laminated Beams Using the Zero-Order Mode of Lamb Waves*, volume Chapter 5. CC BY 3.0 license, Aug 2012.

- [15] H. Sohn, C. R. Farrar, F. M. Hemez, D. D. Shunk, D. W. Stinemates, B. R. Nadler, and J. J. Czarnecki. A review of structural health monitoring literature: 1996-2001. Los Alamos, NM: Los Alamos National Laboratories, 2010.
- [16] J. L. Rose. *Ultrasonic Waves in Solid Media*. Sept. 2004. ISBN 0-521-64043-1.
- [17] C. R. Farrar, S. W. Doebling, and D. A. Nix. Vibration based structural damage identification. *Philosophical Transactions of the Royal Society of London A: Mathematical, Physical and Engineering Sciences*, 359(1778):131 – 149, 2001.
- [18] L. Mallet, B. C. Lee, W. J. Staszewski, and F. Scarpa. Structural health monitoring using scanning laser vibrometry: Lamb waves for damage detection. *Smart Materials and Structures*, 13(2):261, 2004.
- [19] A. A. Shah, Y. Ribakov, and S. Hirose. Nondestructive evaluation of damaged concrete using nonlinear ultrasonics. *Materials and Design*, 30(3):775 – 782, 2009.
- [20] A. Naghashpour and S. Van Hoa. A technique for real-time detecting, locating, and quantifying damage in large polymer composite structures made of carbon fibers and carbon nanotube networks. *Structural Health Monitoring*, 14(1):35–45, 2015.
- [21] J. E. Doherty. *Handbook on Experimental Mechanics*. Nondestructive Evaluation, 1987.
- [22] S. W. Doebling, C. R. Farrar, M. B. Prime, and D. W. Shevitz. Damage identification and health monitoring of structural and mechanical systems from changes in their vibration characteristics. *A Literature Review. Report No. LA- I 3070-MS*, Los Alamos National Laboratory, May 1996.
- [23] E. Peter Carden and P. Fanning. Vibration based condition monitoring: A review. *Journal of Structural Health Monitoring*, 3:355–377, 2004.
- [24] P. Cawley and R. D. Adams. A vibration technique for non-destructive testing of fibre composite structures. *Journal of Composite Materials*, 13:161–173, 1979.
- [25] P. Cawley and R. D. Adams. The location of defects in structures from measurements of natural frequencies. *Strain Analysis*, 14(2):49–57, 1997.
- [26] A. B. Schultz and D. N. Warwick. Vibration response: A non-destructive test for fatigue crack damage in filament-reinforced composites. *Journal of Composite Materials*, 5:394–404, Jul 1971.
- [27] J. L. Rose. A baseline and vision of ultrasonic guided wave inspection potential. *Journal of Pressure Vessel Technology*, Vol. 124:Pp 273–283, Aug 2002.
- [28] T. R. Hay, L. Wei, J. L. Rose, and T. Hayashi. Rapid inspection of composite skin-honeycomb core structures with ultrasonic guided waves. *Journal of Composite Materials*, 37(10):929–939, 2003.
- [29] A. R. D. Jones, Russell A. Noble, R. J. Bozeat, and D. A. Hutchins. Micromachined ultrasonic transducers for damage detection in CFRP composites. *Smart Electronics and MEMS*, 3673:369–378, July 1999.

- [30] V. Giurgiutiu. *Structural Health Monitoring with Piezoelectric wafer active sensors*. Elsevier Academic Press, 2008.
- [31] H. Tsuda, N. Toyama, K. Urabe, and J. Takatsubo. Impact damage detection in cfrp using fiber bragg gratings,. *Smart Mater. Struct.*, Vol.13:pp. 719–724, 2004.
- [32] S. S. Kessler and S. M. Spearing. Structural health monitoring of composite materials using piezoelectric sensors. *Department of Aeronautics and Astronautics, Massachusetts Institute of Technology, Cambridge MA 02139, USA*, 2003.
- [33] A. W. Harris, I. J. Oppenheim, and D. W. Greve. MEMS-based high-frequency vibration sensors. *Smart Materials and Structures*, 20(7):075018, 2011.
- [34] C. Hautamaki, S. Zurn, S. C. Mantell, and D. L. Polla. Experimental evaluation of MEMS strain sensors embedded in composites. *Journal of Microelectromechanical Systems*, vol. 8(no. 3):p272 – 279, September 1998.
- [35] V. K. Varadan and V. V. Varadan. Conformal and embedded IDT microsensors for health monitoring of structures. *Smart Electronics and MEMS*, pages 167–177, June 2000.
- [36] D. W. Greve, A. Jain, and I. J. Oppenheim. MEMS phased array detection in contact with solids. In *Ultrasonics Symposium, 2002. Proceedings. 2002 IEEE*, volume 2, pages 1035–1038 vol.2, 2002.
- [37] K. Suresh, G. Uma, and M. Umapathy. A new self-sensing electronics for piezoelectric resonance sensor. *Journal of Intelligent Material Systems and Structures*, 23(5):587–593, 2012.
- [38] D. Marinkovic and U. Gabbert. Modelling of laminate composites with embedded piezoelectric actuators and sensors. *Mechanics, Automatic Control and Robotics*, Vol.4(16):115–120, 2004.
- [39] G. Park and D. J. Inman. Structural health monitoring using piezoelectric impedance measurements. *Philosophical Transactions of the Royal Society A: Mathematical, Physical and Engineering Sciences*, 365(1851):373–392, 2007.
- [40] S. H. Diaz Valdes and C. Soutis. Delamination detection in composite laminates from variations of their modal characteristics. *Journal of Sound and Vibration*, 228(1):1 – 9, 1999.
- [41] P. Tan and L. Tong. Identification of delamination in a composite beam using integrated piezoelectric sensor/actuator layer. *Composite Structures*, 66(4):391 – 398, 2004. Twelfth International Conference on Composite Structures.
- [42] C. M. Yeum, H. Sohn, J. B. Ihn, and H. J. Lim. Instantaneous delamination detection in a composite plate using a dual piezoelectric transducer network. *Composite Structures*, 94(12):3490 – 3499, 2012.
- [43] D. Kinet, P. Megret, K. W. Goossen, L. Qiu, D. Heider, and C. Caucheteur. Fiber bragg grating sensors toward structural health monitoring in composite materials: Challenges and solutions. *Sensors*, 14(4):7394, 2014.

- [44] Y. Qiu, Q. Wang, H. Zhao, J. Chen, and Y. Wang. Review on composite structural health monitoring based on fiber bragg grating sensing principle. *Journal of Shanghai Jiaotong University (Science)*, 18(2):129–139, 2013.
- [45] C. W. Wern, M. Ramulu, and A. Shukla. Investigation of stresses in the orthogonal cutting of fiber-reinforced plastics. *Experimental Mechanics*, 36(1):33–41, 1996.
- [46] N. Elvin and C. K. Y. Leung. Feasibility of delamination detection with embedded optical fibers. *Proc. SPIE*, 3041:627 – 34, 1997.
- [47] V. Bhatia, C. A. Schmid, K. A. Murphy, R. O. Claus, T. A. Tran, J. A. Greene, and Miller M S. Optical fiber sensing technique for edge-induced and internal delamination detection in composites. *Smart Mater. Struct.*, 4:164 – 9, 1995.
- [48] T. D. Cooper, G. L. Hardy, and F. Feчек. NDT of boron/epoxy structures after aircraft service testing. *Eighth World Conf on NDT*, 1976.
- [49] M. Castaings, P. Cawley, R. Farlow, and G. Hayward. Air-coupled ultrasonic transducers for the detection of defects in plates. *J. Acoust. Soc. Am.*, (100):3070 – 3077, 1996.
- [50] M. C. Tomic, J. M. Elazar, and Z. V. DjinoVIC. Low-coherence interferometric method for measurement of displacement based on a 3 x 3 fibre-optic directional coupler. *Journal of Optics A: Pure and Applied Optics*, 4(6):S381, 2002.
- [51] W. Wang and A. Zhang. Sensitivity analysis in fault vibration diagnosis of structures. *Proc. of 5th International Modal Analysis Conference*, 496-501, 1987.
- [52] H. Sohn, D. Dutta, J. Y. Yang, M. DeSimio, S. Olson, and E. Swenson. Automated detection of delamination and disbond from wavefield images obtained using a scanning laser vibrometer. *Smart Materials and Structures*, 20(4):045017, 2011.
- [53] B. A. Auld. *Acoustic fields and waves in solids*, volume Volumes I & II. John Wiley & Sons, Inc., New York, 2 edition, 1973.
- [54] J. D. Achenbach. *Wave propagation in elastic solids*. North-Holland publications, Amsterdam, 1984.
- [55] K. F. Graff. *Wave motion in elastic solids*. Dover Publications, New York, 1991.
- [56] A. E. H. Love. *The Mathematical Theory of Elasticity*. Cambridge University Press, 4th edition edition, 1944.
- [57] D. Royer and E. Dieulesaint. *Elastic Waves in Solids I and II*. Springer, New York,, 2000.
- [58] L. Rayleigh. On waves propagated along the plane surface of an elastic solid. *Proceedings of the London Mathematical Society*, s1 - 17(1):4 –11, 1885.
- [59] R. Stoneley. Elastic waves at the surface of separation of two solids. *Proceedings of the Royal Society of London A: Mathematical, Physical and Engineering Sciences*, 106(738):416 – 428, 1924.
- [60] I. A. Viktorov. *Rayleigh and Lamb Waves*. Physical Theory and Applications, 1967.

- [61] N. William and Sharpe. Springer handbook of experimental solid mechanics, 2008.
- [62] M. Collet, M. Ruzzene, and K. A. Cunefare. Generation of lamb waves through surface mounted macro-fiber composite transducers. *Smart Materials and Structures*, 20(2):025020, 2011.
- [63] Y. Shi, S. Wooh, and M. Orwat. Laser-ultrasonic generation of lamb waves in the reaction force range. *Ultrasonics*, 41(8):623 – 633, 2003.
- [64] W. Gao, C. Glorieux, and J. Thoen. Laser ultrasonic study of lamb waves: determination of the thickness and velocities of a thin plate. *International Journal of Engineering Science*, 41(2):219 – 228, 2003.
- [65] Y. Wu, M. de Labacherie, and F. Bastien. Investigations on excitation and detection methods for lamb wave sensors. *Sensors and Actuators A: Physical*, 100(2-3):214 – 222, 2002.
- [66] Homepage efunda / Piezo: Constitutive Transforms. [materials/piezo/piezo-math/transforms](#), 2015.
- [67] A. Raghavan and C. E. S. Cesnik. Articles review of guided-wave structural health monitoring, 2007.
- [68] Homepage Optic Fiber Sensor/General photonics. Superluminescent diode light source, 2015.
- [69] E. A. Faulkner and D. W. Harding. A high-performance phase-sensitive detector. *Journal of Scientific Instruments*, 43(2):97, 1966.
- [70] P. Arguel, J. Valentin, S. Fourment, F. Lozes-Dupuy, G. Sarrabayrouse, S. Bonnefont, Y. Jourlin, S. Reynaud, N. Destouches, A. Tishchenko, and J. Jay. A monolithic phase measurement photodetector. In *Sensors, 2003. Proceedings of IEEE*, volume 2, pages 783–786 Vol.2, Oct 2003.
- [71] I. P. Kaminow. *Optical Fiber Telecommunications*. Elsevier Science, 2002.
- [72] E. Udd. *Overview of Fiber Optic Sensors*, volume Fiber Optic Sensors. MARCEL DEKKER, INC. D E K K E R NEW YORK BASEL, 2002. ISBN: 0-8247-0732-X.
- [73] P. L. Fuhr. Fiber optic sensing - from theory to practice. *Sensors*, Part2, May 2000.
- [74] M. W. Maeda, C. J. Chang-Hasnain, J. S. Patel, H. A. Johnson, J. A. Walker, and Chinlon Lin. Two-dimensional multiwavelength surface-emitting laser array in a four-channel wavelength-division-multiplexed system experiment. In *Optical Fiber Communication*, page WC3. Optical Society of America, 1991.
- [75] P. A. Kirkby. Multichannel wavelength-switched transmitters and receivers-new concepts for broadband networks and distributed switching systems. *Lightwave Technology, Journal of*, 8(2):202–211, 1990.
- [76] R. Kashyap. *Fiber Bragg Gratings (Second Edition)*. 2010. ISBN: 978-0-12-372579-0.

- [77] N. Takeda, Y. Okabe, J. Kuwahara, S. Kojima, and T. Ogisu. Development of smart composite structures with small-diameter fiber bragg grating sensors for damage detection: quantitative evaluation of delamination length in cfrp laminates using lamb wave sensing. *Comp. Sci. Tech*, vol. 65:pp. 2575–2587, 2005.
- [78] N. Fisher, S. F. O’Meill, D. J. Webb, C. N. Pannell, D. A. Jackson, L. R. Gavrilov, J. W. Hand, L. Zhang, and I. Bennion. Response of in fibre bragg gratings to focused ultrasound fields. *Proc. 12th Int. Conf. Optical Fibre Sensors*, Williams-burg:190–193, 1997.
- [79] W. Ecke, I. Latka, R. Willsch, A. Reutlinger, and R. Graue. Fibre optic sensor network for spacecraft health monitoring. *MEASUREMENT SCIENCE & TECHNOLOGY*, Vol.12:pp974–980, 2001.
- [80] homepage: Technobis Fibre Technologies. Ultra-high resolution interrogator, 2014.
- [81] M. S. Ferreira, J. Bierlich, M. Becker, K. Schuster, J. L. Santos, and O. Frazao. Ultra-high sensitive strain sensor based on post-processed optical fiber bragg grating. *FIBERS SSN 2079-6439*, 2014.
- [82] G. Luyckx, E. Voet, N. Lammens, and J. Degrieck. Strain measurements of composite laminates with embedded fibre bragg gratings: Criticism and opportunities for research. *Sensors*, 11(1):384–408, 2010.
- [83] R. W. Ogden. Volume changes associated with the deformation of rubber-like solids. *Journal of the Mechanics and Physics of Solids*, 24(6):323 – 338, 1976.
- [84] C. D. Butter and G. B. Hocker. Fiber optics strain gauge. *Appl. Opt.*, pages 2867 – 2869, 1978.
- [85] G. B. Hocker. Fiber optic sensing of pressure and temperature. *Appl. Opt.*, 18(9):1445 – 1448, May 1979.
- [86] J. S. Sirkis and C. E. Taylor. Interferometric-fiber-optic strain sensor. *Experimental Mechanics*, 28(2):170–176, 1988.
- [87] L. B. Jeunhomme. *Single-Mode Fiber Optics*. New York, 1983.
- [88] S. F. Nye. Physical properties of crystals. *London: Oxford*, 1954.
- [89] P. Merritt, R. P. Tatam, and D. A. Jackson. Interferometric chromatic dispersion measurements on short lengths of monomode optical fiber. *J. Lightwave Technol.* 7, pages pp. 703–716, 1989.
- [90] F. Farahi, P. Akhavan Leilabady, J. D. C. Jones, and D. A. Jackson. Interferometric fibre-optic hydrogen sensor. *Journal of Physics E: Scientific Instruments*, 20(4):432, 1987.
- [91] X. S. Yao and J. Feinberg. Simple in-line method to measure the dispersion of an optical system. *Appl. Phys. Lett*, vol.62:pp. 811–813, 1993.
- [92] D. Mueller, J. West, and K. Koch. Interferometric chromatic dispersion measurement of a photonic bandgap fiber. *Proc. SPIE*, Vol. 4870:pp. 395– 403, 2002.

- [93] B. H. Lee, Y. H. Kim, K. S. Park, J. B. Eom, M. J. Kim, B. S. Rho, and H. Y. Choi. Interferometric fiber optic sensors. *Sensors*, 12(3):2467, 2012.
- [94] D. Uttamt, B. Culshawf, J. D. Ward, and D. Carter. Interferometric optical fibre strain measurement. *J. Phys. E: Sci. Instrum*, Vol.18:290–293, 1985.
- [95] Y. Zhao and Y. Liao. Discrimination methods and demodulation techniques for fiber bragg grating sensors. *J. Optics and Lasers in Engineering*, 41:1 – 18, 2004.
- [96] K. Liu, S. M. Ferguson, and R. M. Measures. Fiber-optic interferometric sensor for the detection of acoustic emission within composite materials. *Opt. Lett.*, 15(22):1255–1257, Nov 1990.
- [97] B. Culshaw. The optical fibre sagnac interferometer: an overview of its principles and applications. *Measurement Science and Technology*, 17(1):R1, 2006.
- [98] K. Wada, H. Narui, D. Yamamoto, T. Matsuyama, and H. Horinaka. Balanced polarization maintaining fiber sagnac interferometer vibration sensor. *Opt. Express*, 19(22):21467–21474, Oct 2011.
- [99] S. J. Russell, K. R. C. Brady, and J. P. Dakin. Real-time location of multiple time-varying strain disturbances, acting over a 40-km fiber section, using a novel dual-sagnac interferometer. *Lightwave Technology, Journal of*, 19(2):205–213, Feb 2001.
- [100] D. Harvey, R. McBride, R. Barton, and J. D. C. Jones. A velocimeter based on the fibre optic sagnac interferometer. *Meas. Sci. Technol.*, Vol. 3(no. 11):1077 –1083, 1992.
- [101] T. A. Carolan, R. L . Reuben, J. S. Barton, R. McBride, and J. D. C. Jones, editors. *Fiber optic Sagnac interferometer for non contact structural monitoring in power plant applications*, volume PP. 173-177, 1995.
- [102] N. Singh, S. C. Jain, A. K. Aggarwal, and R. P. Bajpai. Develop and experiment studies of fibre optic extrinsic fabry-perot interferometric sensor for measurement of strain in structures. *Current Science*, Vol.86(nr.2):pp. 309–314, 2004.
- [103] H. S. Park, G. Thursby, and B. Culshaw. Optical acoustic detector based on a fiber fabry-perot interferometer. *Appl. Opt.*, Vol. 44(No.4):pp.489 – 492, 2005.
- [104] G. S. Peng and E. G. Wolff. Processing of interferometric signals for a {CTE} measurement system. *Thermochimica Acta*, 218(0):101 – 112, 1993.
- [105] P. Lawson. *Principles of Long Baseline Stellar Interferometry*. Number pp. 325-332. NASA-JPL (Publication 00-009), 2000.
- [106] N. Beverini, E. Maccioni, M. Morganti, F. Stefani, R. Falciai, and C. Trono. Fiber laser strain sensor device. *Journal of Optics A: Pure and Applied Optics*, 9(10):958, 2007.
- [107] A. Raghavan and C. E. S. Cesnik. Finite-dimensional piezoelectric transducer modeling for guided wave based structural health monitoring. *Smart Materials and Structures*, 14(6):1448, 2005.
- [108] A. F. Bower. Applied mechanics of solids, chapter 3 constitutive models-relations between stress and strain, 2012.

- [109] S. G. Lekhnitskii. *Theory of Elasticity of an anisotropic Elastic body*. Holden-Day, Inc., 1963.
- [110] P. Antunes, F. Domingues, M. Granada, and P. Andre. Mechanical properties of optical fibers. *Interchopen*, pages p. 537–550, 2012.
- [111] A. Fitzgibbon, M. Pilu, and R. B. Fisher. Direct least square fitting of ellipses. *Pattern Analysis and Machine Intelligence, IEEE Transactions on*, 21(5):476–480, May 1999.

# Nomenclature

CCW	Counterclockwise
CFRP	Carbon fiber reinforced polymers
CW	Clockwise
EMAT	Electromagnetic Acoustic Transducers
FBG	Fiber Bragg Grating
FE	Finite Element
FEA	Finite Element Analysis
FEM	Finite Element Method
LED	Light-Emitting Diode
MEMS	Micro-Electro Mechanical Systems
NA	Numerical Aperture
NDT	Non-Destruction Testing
PD	Photodetectors
PZT	Piezoelectric Lead zirconate titanate
PZT	zirconate titanate ( $\text{Pb}[\text{Zr}(x)\text{Ti}(1-x)]\text{O}_3$ )
SAW	Surface acoustic wave
SHM	Structural Health Monitoring
SLD	Superluminescent Light Emitter Diode
TEM	Transversal ElectroMagnetic
TIA	Transimpedance Amplifiers

